

RE-OS GEOCHRONOLOGY OF BASE METAL SULFIDES  
FROM CRATONIC MANTLE XENOLITHS:  
CASE STUDY FROM SOMERSET ISLAND (CANADA)  
AND METHOD DEVELOPMENT

Dissertation  
zur  
Erlangung des Doktorgrades (Dr. rer. nat.)  
der  
Mathematisch-Naturwissenschaftlichen Fakultät  
der  
Rheinischen Friedrich-Wilhelms-Universität Bonn

vorgelegt von  
**Alessandro Bragagni**  
aus  
Bagno a Ripoli, Firenze, Italien

Bonn, 2016

Angefertigt mit Genehmigung der Mathematisch-Naturwissenschaftlichen Fakultät der  
Rheinischen Friedrich-Wilhelms-Universität Bonn

1. Gutachter: Prof. Dr. Ambre Luguet

2. Gutachter: PD Dr. Raúl Fonseca

Tag der Promotion: 11. März 2016

Erscheinungsjahr: 2016

*“There are two possible outcomes:  
if the result confirms the hypothesis, then  
you’ve made a measurement.  
If the result is contrary to the hypothesis,  
then you’ve made a discovery.”*

E. Fermi



## ABSTRACT

Robust and reliable time constraints are necessary to infer the formation and evolution of the cratonic mantle. Due to the large fractionation of Re from Os during mantle melting, the Re-Os decay system has been largely used for dating the melting event that led to the formation of the subcontinental lithospheric mantle (SCLM). In mantle rocks Re, Os and the other highly siderophile elements (HSE: Ru, Rh, Pd, Re, Os, Ir, Pt, and Au) are controlled by base metal sulfides (BMS), which can be residual phases of partial melting processes or can be re-introduced in mantle rocks during metasomatism. The present study aimed at the improvement and enhancement of our ability to use the Re-Os system and the HSE to unravel geological processes recorded in BMS. The contribution of this work is twofold because it provides new data on natural samples as well as a novel analytical technique for future applications. In the first part of this dissertation (Chapter 1) some basic concepts are introduced to make the reader more familiar with the topics encountered in the next sections. This includes an overview of the HSE behavior in terrestrial reservoirs and the explanations of the geochemical tools that will be used in the following sections.

The second part of this dissertation (Chapter 2) is focused on the investigation of partial melting and metasomatic processes recorded in four mantle xenoliths from Somerset Island (Rae craton, Canada). After textural and mineralogical investigations, individual BMS grains were micro-sampled and analyzed for  $^{187}\text{Os}/^{188}\text{Os}$ . The two xenoliths with the most metasomatic HSE signature (e.g. suprachondritic Pd/Pt) are distinguished for the high BMS modal abundance, the occurrence of large interstitial BMS grains, and the extreme  $^{187}\text{Os}/^{188}\text{Os}$  variation measured in BMS grains ( $^{187}\text{Os}/^{188}\text{Os} = 0.172\text{-}0.108$ ). Archean Re-depletion model ages ( $T_{\text{RD}}$ ) are recorded in BMS grains from three different xenoliths, suggesting a main formation of the SCLM at 2.7-2.8 Ga, in association with the local Rae greenstone belts. A similar scenario was proposed for the nearby Slave craton, which confirms that different terrains of the Canadian Shield share a similar Neoproterozoic history. At the whole rock scale, the  $T_{\text{RD}}$  age of 2.7-2.8 Ga is clearly recorded only in one xenolith with residual HSE signature (i.e. subchondritic Pt/Ir, Pd/Pt, and Re/Pd). This supports and further stresses that: 1) whole rock  $T_{\text{RD}}$  ages should be used carefully in xenoliths with metasomatic HSE signature, and 2) single grain BMS can record the age of formation of the SCLM even in heavily metasomatized mantle xenoliths. Single BMS grains yielded two

distinct Paleoproterozoic  $T_{RD}$  ages (~1.9 and ~2.2 Ga) that are not resolvable at the whole rock scale. The two  $T_{RD}$  ages are consistent with a scenario where metasomatic BMS were introduced in the SCLM during a first phase of rifting of the Slave from the Rae craton (2.2 Ga) and a later collision of the two cratons (1.9 Ga, Thelon-Talston orogeny). In the third part of this dissertation (Chapter 3) a novel analytical method is proposed to analyze  $^{187}\text{Os}/^{188}\text{Os}$  along with Ru, Pd, Re, Os, Ir, and Pt concentrations in individual  $\mu\text{g}$ -weight BMS grains. To set up this method, two Fe-Ni sulfides were synthesized and independently characterized for HSE content and  $^{187}\text{Os}/^{188}\text{Os}$ . Fragments of the two sulfides were used to test different digestion and separation methods. It is here shown that a simultaneous digestion and Os extraction yields inaccurate Os concentrations. The improved procedure proposed in this study includes BMS digestion in HBr + HCl, Os micro-distillation, and cation resin separation of Ru, Pd, Re, Ir and Pt. The  $^{187}\text{Os}/^{188}\text{Os}$  ratio and the HSE concentrations are measured by mass spectrometry (N-TIMS and SF-ICP-MS). The independently determined HSE concentrations are reproduced by this technique with differences < 10% for Pd, Os and Ir, and < 20% for Ru, Re, and Pt. The  $^{187}\text{Os}/^{188}\text{Os}$  ratio is indistinguishable within the analytical precision (2SD ~ 0.1%). Owing to the chemical separation of the analytes, the proposed procedure overcomes many of the analytical issues encountered during LA-ICP-MS analyses (e.g.  $^{187}\text{Re}$  isobaric interference on  $^{187}\text{Os}$  and matrix effects). Moreover, the analysis of the entire grain, avoid any sampling bias related to the complex mineralogical assemblage typically observed in natural BMS.

As shown in this dissertation, BMS grains record a multitude of magmatic and metasomatic processes that cannot be individually discriminated at the whole rock scale. The comprehension of these processes represents an exciting challenge as it will improve our ability of using the Re-Os system and, ultimately, to constrain the timing of mantle dynamics. Coupled HSE and  $^{187}\text{Os}/^{188}\text{Os}$  investigations in individual BMS grains will provide an essential tool towards this goal.

# TABLE OF CONTENTS

<b>ABSTRACT</b> .....	<b>I</b>
<b>CHAPTER 1: INTRODUCTION</b> .....	<b>1</b>
1.1 THE CRATONIC MANTLE.....	1
1.2 DATING THE FORMATION OF THE SUBCONTINENTAL LITHOSPHERIC MANTLE .....	4
1.2.1 <i>Basics of isotope geochronology</i> .....	4
1.2.2 <i>The Re-Os decay system</i> .....	7
1.2.3 <i>Dating melting events with the Re-Os decay system</i> .....	7
1.3 THE HIGHLY SIDEROPHILE ELEMENTS.....	10
1.3.1 <i>The origin of HSE in the mantle</i> .....	10
1.3.2 <i>Behavior of HSE during mantle melting</i> .....	12
1.3.3 <i>Rhenium</i> .....	14
1.3.4 <i>Osmium</i> .....	15
1.4 MANTLE METASOMATISM AND ITS EFFECT ON HSE SYSTEMATIC AND RE-OS DECAY SYSTEM .....	16
1.4.1 <i>Residual and metasomatic BMS</i> .....	17
1.5 MOTIVATIONS AND OUTLINE OF THE THESIS.....	19
1.5.1 <i>The Canadian Shield</i> .....	19
1.5.2 <i>Outline of the thesis</i> .....	22
<b>CHAPTER 2: OSMIUM ISOTOPIC COMPOSITION OF BASE METAL SULFIDES IN MANTLE XENOLITHS FROM SOMERSET ISLAND (CANADA)</b> .....	<b>25</b>
2.1 INTRODUCTION.....	25
2.2 GEOLOGICAL SETTING .....	27
2.3 MANTLE XENOLITHS FROM SOMERSET ISLAND .....	29
2.3.1 <i>Description of the studied samples</i> .....	31
2.4 ANALYTICAL METHODS.....	33
2.4.1 <i>Microprobe analyses</i> .....	33
2.4.2 <i>Base metal sulfides microsampling</i> .....	34
2.4.3 <i>Osmium chemical separation and N-TIMS analyses</i> .....	36
2.5 RESULTS .....	37
2.5.1 <i>Silicate mineral chemistry and geothermobarometry</i> .....	37
2.5.2 <i>Base metal sulfides</i> .....	38
2.5.3 <i><sup>187</sup>Os/<sup>188</sup>Os of single grain BMS</i> .....	45
2.6 DISCUSSION .....	49
2.6.1 <i>Origin of base metal sulfides, PGM and silicates</i> .....	49
2.6.2 <i>Mantle processes and Re-Os model ages</i> .....	54
2.6.3 <i>Age significance and geodynamic interpretation of BMS T<sub>RD</sub> model ages</i> .....	57
2.7 CONCLUDING REMARKS.....	61

<b>CHAPTER 3: HSE AND <sup>187</sup>OS/<sup>188</sup>OS CHARACTERIZATION OF SINGLE SULFIDES VIA MICRO-CHEMISTRY .....</b>	<b>63</b>
3.1 INTRODUCTION .....	63
3.2 EXPERIMENTAL AND ANALYTICAL METHODS .....	65
3.2.1 <i>Synthesis of the sulfide standard materials</i> .....	66
3.2.2 <i>Characterization of the sulfide standard materials</i> .....	67
3.2.3 <i>Single grain procedures</i> .....	68
3.2.4 <i>Mass spectrometry</i> .....	73
3.3 RESULTS .....	74
3.3.1 <i>Total procedural blanks</i> .....	74
3.3.2 <i>Composition of the two synthesized sulfide standards</i> .....	75
3.3.3 <i>Osmium concentration and <sup>187</sup>Os/<sup>188</sup>Os in single grain procedures</i> .....	78
3.3.4 <i>Ruthenium, Pd, Re, Ir, and Pt concentrations in single grain procedures</i> .....	82
3.4 DISCUSSION .....	85
3.4.1 <i>Osmium concentrations and <sup>187</sup>Os/<sup>188</sup>Os in single grain procedures</i> .....	85
3.4.2 <i>Ruthenium, Pd, Re, Ir, and Pt concentrations in single grain procedures</i> .....	90
3.5 CONCLUDING REMARKS AND PROPOSED PROTOCOL .....	93
<b>CHAPTER 4: SUMMARY, CONCLUSIONS AND FUTURE WORK .....</b>	<b>97</b>
<b>APPENDIX A .....</b>	<b>101</b>
<b>APPENDIX B.....</b>	<b>103</b>
<b>APPENDIX C SULFIDE MINERAL FORMULAE.....</b>	<b>107</b>
<b>REFERENCES .....</b>	<b>109</b>
<b>ACKNOWLEDGEMENTS .....</b>	<b>135</b>

## *Chapter 1:*

# INTRODUCTION

## ***1.1 THE CRATONIC MANTLE***

In the last century, many geophysical, petrological and geochemical studies have investigated the structure and the physico-chemical properties of the Earth's mantle. According to these studies, which are summarized in several textbooks (e.g. Anderson, 1989; Jackson, 2000; Schubert et al., 2001; Smith, 1986), the mantle is subdivided into three layers on the basis of its physical and chemical properties: 1) the lower mantle, which extends from the core boundary (2890 km) to about 660 km depth; 2) a transition zone that ranges between 660 and 410 km depth and 3) the upper mantle, which starts at 410 km depth and it is overlain by the Earth's crust (Mohorovičić discontinuity 3-90 km). With respect to its rheological behavior, most of Earth's mantle behaves as a ductile medium. However, the shallowest part of the mantle is mechanically rigid and, when combined with the equally rigid crust, forms the Earth's lithosphere. The lithosphere is the outer shell of the Earth, which is involved in plate tectonics. It has a thickness of 50-100 km in oceanic environment and 40-250 km in continents. The oldest crustal rocks are systematically recovered within continents, suggesting that the continental lithosphere is less efficiently involved in recycling processes. The oldest fragments of the crust, which have Hadean-Archean ages (e.g. Acasta Gneiss, 4.0 Ga, Bowring and Williams, 1999), are found within large tectonically stable domains called cratons (Figure 1-1). Due to their old age signature, it is likely that cratons formed when the bulk silicate Earth (BSE, i.e. the silicate fraction left after core formation) began to differentiate into crust and mantle. Understanding the genesis of cratons thus allows inference about the first pieces of the puzzle that forms the geodynamic framework of our planet.

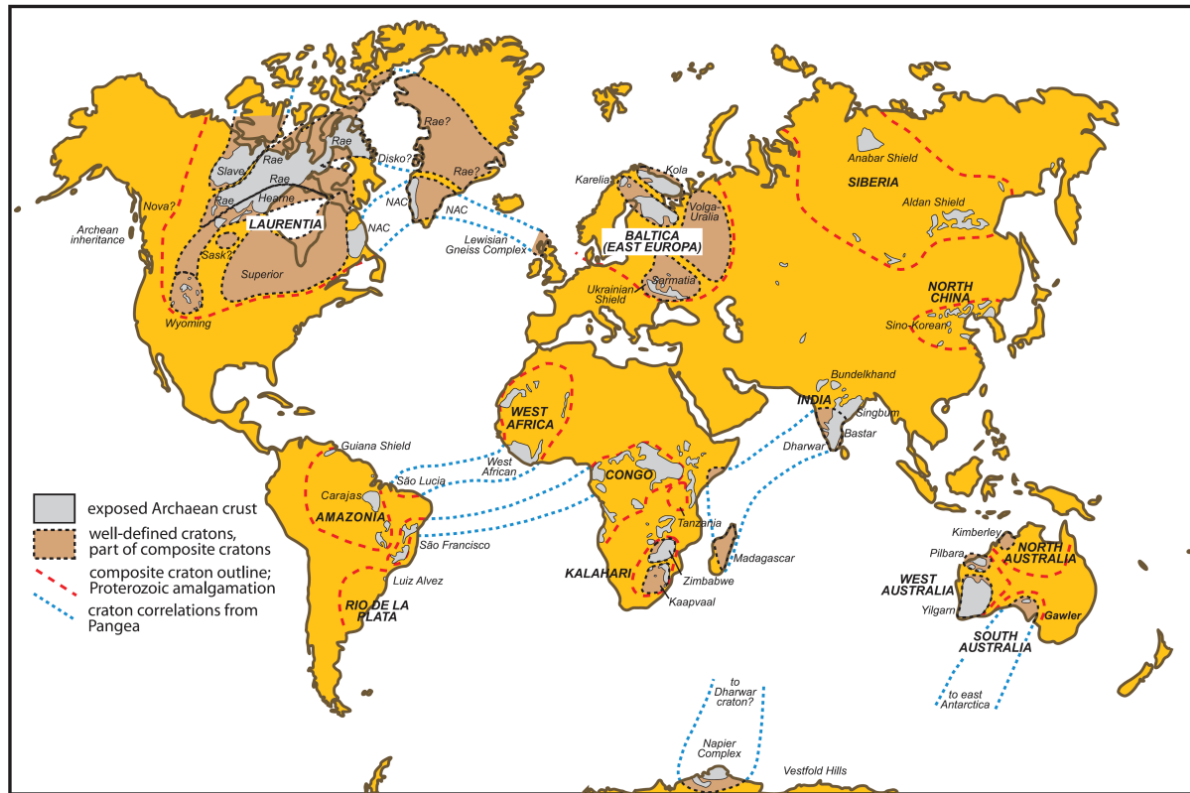


**Figure 1-1** Global map showing the distribution of cratonic terranes. From Pearson and Wittig (2008).

Cratons are characterized by thick ( $> 150$  km) subcontinental lithospheric mantle (SCLM) roots, which formed as residue of partial melting (O'Hara et al., 1975). Because of the high fraction of magma extracted, these mantle rocks are characterized by low density (Jordan, 1978), which contributed to the chemical buoyancy and the long term stabilization of cratons (e.g. Herzberg and Rudnick, 2012; Jordan, 1978). The exact mechanism of formation of the SCLM and its genetic linkage with overlying crustal domains are still unclear and are a matter of ongoing debate (cf. Aulbach, 2012; Griffin et al., 2003; Lee et al., 2011). The proposed SCLM formation processes range between two end-member scenarios, one involving deep melting of a mantle plume (Arndt et al., 2009; Aulbach, 2012; Griffin et al., 2003) and the other invoking the stacking of lithospheric blocks (Pearson and Wittig, 2008; Rollinson, 2010; Tappe et al., 2011). One strategy used to discriminate between these two processes consists in the investigation of the age distribution within the SCLM (Lee, 2006; Pearson, 1999). In the plume model, the melting can be considered instantaneous on a geological timescale and thus no age variation is expected inside the SCLM (Figure 1-2a). In the second scenario, which involves stacking of lithospheric blocks, the ages inside the SCLM will vary depending on the age of each

individual block. For instance, simple underthrusting and imbrication of oceanic lithosphere would lead to the presence of an age gradient perpendicular to the direction of thrusting (Figure 1-2b) while thickening or accretion in an arc environment would generate a more irregular age distribution (Figure 1-2c). It is important to note that more complex models for SCLM formation are possible and include hybrid scenarios (Pearson and Wittig, 2008). Robust geochronology investigations on SCLM xenoliths are essential to understand which processes lead to the formation of the earliest lithosphere on Earth. Moreover, a comparison between crustal and mantle ages might shed light on the genetic link between these two domains on a global (cf. Pearson et al., 2007) and regional (e.g. Luguet et al., 2009; Mundl et al., 2014) scale.

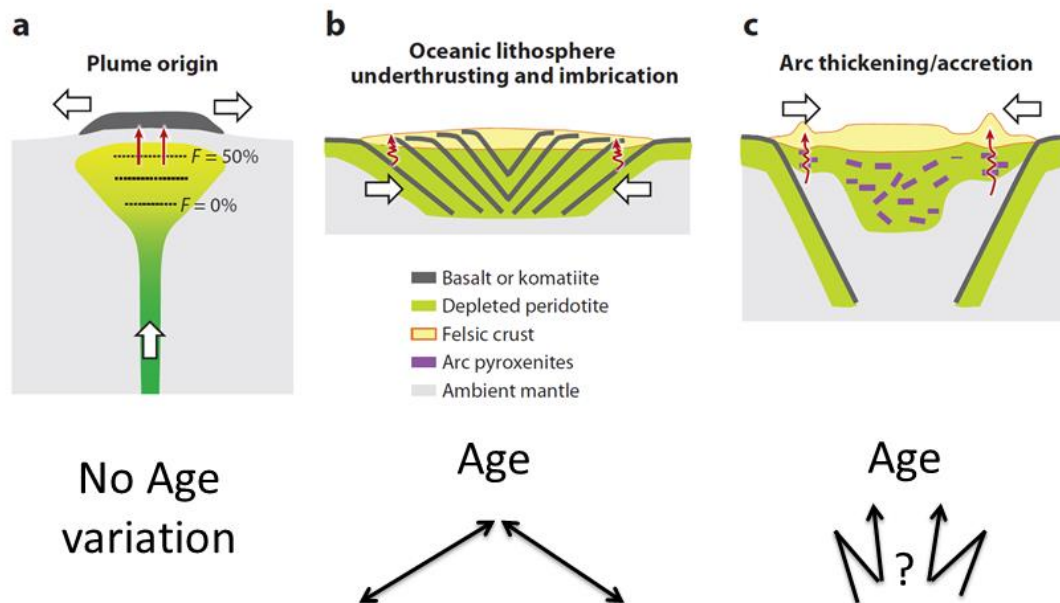


**Figure 1-2** Three different models proposed for SCLM formation and their expected age distribution. a) Plume model. The highest degrees of partial melting ( $F$  in figure) are expected in the shallower portions. In this scenario the formation of the SCLM is related to a single event and no age variation is expected. b-c) Stacking of lithospheric blocks. b) Underthrusting and imbrication of lithosphere formed in mid oceanic ridges. In this scenario the age distribution within the SCLM depends on the age of each individual block. c) Thickening/accretion of lithosphere formed in arc environment. An age gradient perpendicular to the thrusts would form after a thickening process, while a more chaotic distribution is expected after accretion. White arrows indicate the direction of the motion. Modified from Lee et al. (2011).

## ***1.2 DATING THE FORMATION OF THE SUBCONTINENTAL LITHOSPHERIC MANTLE***

The direct study of large portions of the SCLM is possible in tectonically emplaced domains that occur as orogenic massifs and ophiolite complexes. Alternatively, smaller portions of the mantle are available as xenoliths in volcanic rocks. Kimberlites are volcanic and sub-volcanic rocks that often occur in cratons and commonly host ultramafic xenoliths. Kimberlites are thought to have formed in the deep portion of the Earth's mantle before reaching the surface after fast rising through the mantle and the crust (cf. review by Sparks, 2013). Because they are emplaced rapidly, kimberlite-hosted mantle xenoliths record the conditions of the SCLM at the moment of the eruption, being less affected by low-temperature re-equilibration processes when compared to mantle domains in orogenic massifs and ophiolite complexes. Therefore, kimberlite-hosted mantle xenoliths provide a unique opportunity to directly study and date the lithospheric mantle below cratons.

### ***1.2.1 Basics of isotope geochronology***

Isotope geochronology is the main tool that can be used to determine absolute ages of geological processes. It makes possible to constrain the timing of processes that operate over timescales inaccessible to human observation. The key mechanism for isotope geochronology is based on the decay of radioactive isotopes (parents) to radiogenic ones (daughters). The number of decays per unit of time is directly proportional to the number of parent isotopes. Thus, the decay process is described by the following exponential law equation:

$$D = D_0 + N(e^{\lambda t} - 1) \quad (1)$$

Where  $D$  and  $N$  are the number of atoms of the daughter and parent isotope, respectively,  $t$  is the elapsed time, and  $\lambda$  is the decay constant, which controls the rate of the decay. As shown in Equation 1, ideally, a chemical process can be directly dated by measuring the concentration of the parent ( $N$ ) and daughter ( $D$ ) isotopes in one product, provided that the initial concentration of the daughter isotope ( $D_0$ ) is known.

Measurements of absolute isotopic concentrations are typically less precise than isotopic ratios. This is the main reason why it is usually more convenient to normalize both terms of Equation 1 to a stable reference isotope ( $D_{ref}$ ) of the same element of  $D$ , hence:

$$\frac{D}{D_{ref}} = \frac{D_0}{D_{ref}} + \frac{N}{D_{ref}}(e^{\lambda t} - 1) \quad (2)$$

The term  $D_0/D_{ref}$  of Equation (2) is critical for dating because not directly measurable. The “isochron method” and the “model ages” are the two main approaches used for overcome this issue and are briefly described below.

#### 1.2.1.1 *The isochron method*

If  $x = D_0/D_{ref}$  and  $y = N/D_{ref}$ , Equation 2 can be rewritten as  $y = y_0 + x(e^{\lambda t} - 1)$ , which is the equation of a straight line with a slope of  $e^{\lambda t} - 1$ . This implies that in a diagram where  $D/D_{ref}$  is reported against  $N/D_{ref}$  all the co-genetic products (e.g. mineral phases of a single rock or different rocks from a magmatic suite) lie on a straight line, whose slope is direct function of  $t$  and therefore can be used to infer the age (Nicolaysen, 1961). This line is called an isochron and the plot is known as the isochron diagram (Figure 1-3). The isochron method is applicable for dating when  $D/D_{ref}$  and  $N/D_{ref}$  are determined in at least two coeval products (i.e. mineral phases or whole rocks) with variable  $N/D_{ref}$ .

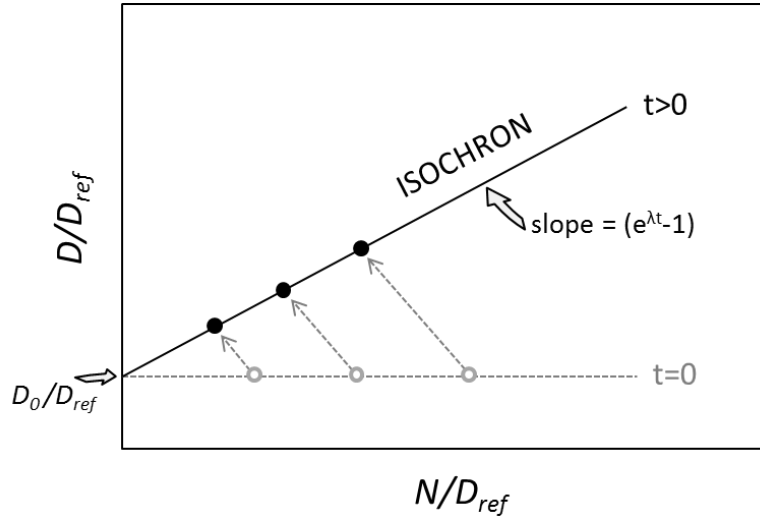


**Figure 1-3** Principles of the isochron dating method. The age can be determined by the slope of the isochron which can be inferred by measuring several co-genetic products (filled symbols). The starting compositions (at  $t = 0$ ) of the products is reported as grey open symbols. The effect of aging for each product is represented by the dashed arrows.

### 1.2.1.2 Model ages

By the use of Equation 2, it is possible to describe the isotopic evolution of a geological reservoir that behaves as a closed system:

$$\left(\frac{D}{D_{ref}}\right)_{res} = \left(\frac{D_0}{D_{ref}}\right)_{res} + \left(\frac{N}{D_{ref}}\right)_{res} (e^{\lambda t} - 1) \quad (3)$$

We can assume that a sample is extracted from the reservoir at a certain time. At this time ( $t_0$ ) the sample and the reservoir will have the same isotopic composition, which is  $(D_0/D_{ref})_{res}$ . Over time, the isotopic evolution of the sample can then be expressed as:

$$\left(\frac{D}{D_{ref}}\right)_{smp} = \left(\frac{D_0}{D_{ref}}\right)_{res} + \left(\frac{N}{D_{ref}}\right)_{smp} (e^{\lambda t} - 1) \quad (4)$$

As shown by Equation (4), the  $D/D_{ref}$  of a given sample can diverge from that of the reservoir if they have different  $N/D_{ref}$ . In order to have  $(N/D_{ref})_{res} \neq (N/D_{ref})_{smp}$  the sample needs to be extracted from the reservoir during a process that is able to fractionate N from D. When this is the case, Equations 3 and 4 can be solved with respect to  $t$ , making it possible to date when the sample was extracted from the reservoir.

Isochrons and model ages provide different age information and hence they can be used to date different processes. With the first method, the obtained age dates an equilibrium condition between the analyzed products. With model ages, a single product is analyzed and the equilibrium is assumed to have occurred within a certain reservoir of known evolution. For example, in an ideal case it is possible to date the crystallization of a magma by an isochron (i.e. analyzing different mineral phases) and to date the extraction of the primitive magma from the mantle by the use of a model age.

### ***1.2.2 The Re-Os decay system***

The applicability of a decay system to date a geological process depends on the value of the decay constant, the behavior of N and D during such process, and the available analytical techniques. The most commonly used decay systems (e.g.  $^{87}\text{Rb}$ - $^{87}\text{Sr}$ ,  $^{147}\text{Sm}$ - $^{143}\text{Nd}$ ,  $^{238}\text{U}$ - $^{206}\text{Pb}$ ,  $^{235}\text{U}$ - $^{207}\text{Pb}$ ,  $^{232}\text{Th}$ - $^{208}\text{Pb}$ ) are based on elements that show an incompatible geochemical behavior, i.e. they partition preferentially into the liquid phases during mantle melting (e.g. Dickin, 2005). Thus, mantle peridotites formed as residues of melting processes are depleted in these elements after melt extraction. The application of these isotopic systems to date melt extraction events in mantle peridotites is limited because parent and daughter isotopes can be easily affected by overprinting processes. This can occur, for example, when a small amount of liquid (usually enriched in incompatible elements) percolates through a residual peridotite.

When compared to other parent-daughter isotope couples, the  $^{187}\text{Re}$ - $^{187}\text{Os}$  decay system shows a different behavior in magmatic processes because Re is moderately incompatible during partial melting while Os is compatible (e.g. Shirey and Walker, 1998 and references therein). As a consequence, Os is enriched in residual peridotites and is expected to be relatively depleted in metasomatic melts/fluids. Due to the large fractionation of Os from Re during mantle melting and the relative robustness to overprinting processes, the Re-Os decay system is the most suitable tool to date melting events in peridotites.

### ***1.2.3 Dating melting events with the Re-Os decay system***

In principle, melting events can be dated in mantle rocks using Re-Os isochrons or Re-Os model ages. The most robust ages are derived from isochrons because they directly

allow for the dating of events without depending on the assumptions of model ages. However, if we exclude the isochron reported by Westerlund et al. (2006) for sulfide inclusions in diamonds, there have been no statistically significant Re–Os isochrons reported from whole rock peridotites or from their mineral separates (Rudnick and Walker, 2009).

Due to the lack of Re–Os isochrons, melting events are commonly dated with Re–Os model ages (Carlson, 2005; Rudnick and Walker, 2009; Shirey and Walker, 1998; Walker et al., 1989). With this approach, the mantle, which is assumed to evolve as a closed and homogenous system, is used as the reference reservoir. Combining Equations 3 and 4 and solving them with respect to  $t$  (re-named  $T_{MA}$  in the following equation) it is possible to obtain:

$$T_{MA} = \frac{1}{\lambda} \ln \left( \frac{(^{187}\text{Os}/^{187}\text{Os})_{smp} - (^{187}\text{Os}/^{187}\text{Os})_{res}}{(^{187}\text{Re}/^{187}\text{Os})_{smp} - (^{187}\text{Re}/^{187}\text{Os})_{res}} + 1 \right) \quad (5)$$

This is the equation of the “classic”  $T_{MA}$  model age (cf. Figure 1-4) and it is commonly used also in other systematics (e.g. Sm–Nd, Lu–Hf).

Due to the incompatible behavior, Re can be easily re-introduced to peridotites during, for example, magma percolation. When this is the case, Equation 5 gives artificially old ages because it does not take into account that Re may have been added after the melting event. In this case,  $T_{MA}$  ages will overestimate the time of melt depletion events (e.g. Carlson, 2005; Rudnick and Walker, 2009). In order to prevent an over-correction for Re decay, the term  $(^{187}\text{Re}/^{187}\text{Os})_{smp}$  of Equation 5 can be omitted, which leads to:

$$T_{RD} = \frac{1}{\lambda} \ln \left( \frac{(^{187}\text{Os}/^{187}\text{Os})_{smp} - (^{187}\text{Os}/^{187}\text{Os})_{res}}{-(^{187}\text{Re}/^{187}\text{Os})_{res}} + 1 \right) \quad (6)$$

This model age is called Re-depletion age ( $T_{RD}$ ) (cf. Figure 1-4 Walker et al., 1989). With this approach the decay of  $^{187}\text{Re}$  after the melting event is considered zero. Hence,  $T_{RD}$  model ages represent a minimum melting age.

In mantle xenoliths, enrichment in Re can occur during the infiltration of the Re-rich host magma (e.g. Irvine et al., 2003; Pearson et al., 1995a, 1995b). When the eruption age

is known, the measured  $^{187}\text{Os}/^{188}\text{Os}$  can be corrected for the decay of  $^{187}\text{Re}$  only after the emplacement. This model age is called  $T_{\text{RD}}$  eruption age (Pearson et al., 1995b cf. Figure 1-4).

The choice of the reference reservoir, which is used to define the mantle evolution line (Figure 1-4), is a critical point. Two approaches are commonly used. The first one utilizes the chondritic  $(^{187}\text{Os}/^{188}\text{Os})_{\text{res}}$  and  $(^{187}\text{Re}/^{188}\text{Os})_{\text{res}}$  (Fischer-Gödde et al., 2010; Walker et al., 2002), while the second one is based on direct estimates of the present-day upper mantle values (Meisel et al., 2001).

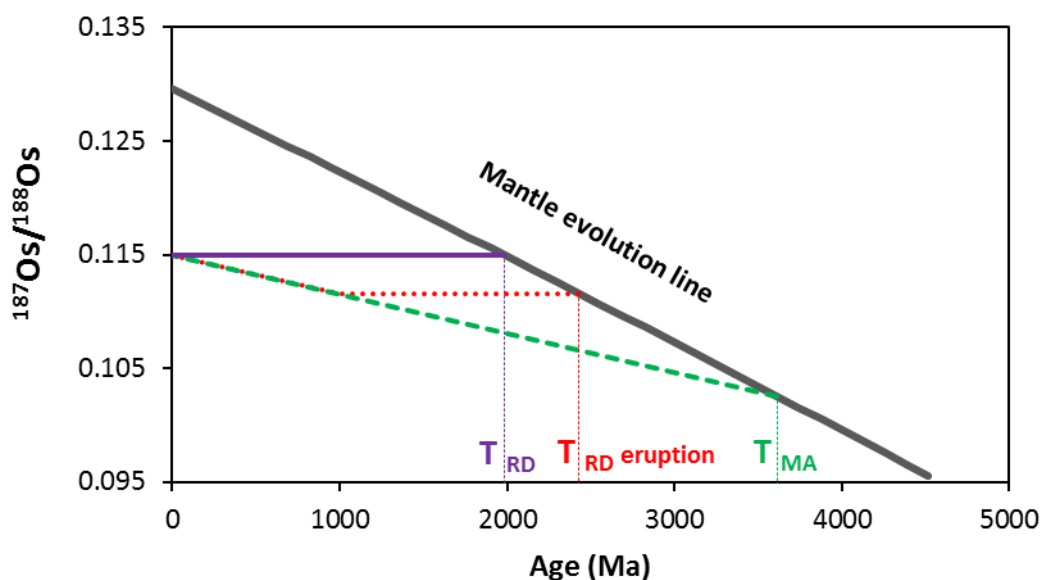


**Figure 1-4** Example of different Re-Os model ages calculated from a hypothetical mantle with  $^{187}\text{Os}/^{188}\text{Os} = 0.115$  and  $^{187}\text{Re}/^{188}\text{Os} = 0.2$ . The eruption age of the host magma is assumed to be 1 Ga. The mantle evolution line is calculated using the estimation of the present day composition reported by Meisel et al. (2001) ( $^{187}\text{Os}/^{188}\text{Os} = 0.1296$  and  $^{187}\text{Re}/^{188}\text{Os} = 0.4353$ ). The  $T_{\text{RD}}$  age of a sample is simply obtained by plotting the measured  $^{187}\text{Os}/^{188}\text{Os}$  on the mantle evolution line. The  $T_{\text{MA}}$  represents the intersection of the mantle evolution line with the evolution line of the sample. The evolution line of the sample starts from the measured  $^{187}\text{Os}/^{188}\text{Os}$  and it can be extrapolated backwards with a slope that is a function of  $^{187}\text{Re}/^{188}\text{Os}$ . The  $T_{\text{RD}}$  eruption age follows the same evolution line of the  $T_{\text{MA}}$  but only until the eruption age. Afterwards the  $^{187}\text{Os}/^{188}\text{Os}$  is constant and moves parallel to the x-axis until it intersects the mantle evolution line.

### 1.3 THE HIGHLY SIDEROPHILE ELEMENTS

Rhenium and Os belong to the Highly Siderophile Elements (HSE), a group of elements that show peculiar compartment when compared to lithophile elements. Understanding the geochemical behavior of HSE provides important constraints for the interpretation of Re-Os ages. The HSE include Ru, Rh, Pd, Re, Os, Ir, Pt, and Au, which are geochemically grouped together because of their high affinity for the metal-rich phases during core formation (e.g. O'Neill et al., 1995). In the Earth, the HSE are heterogeneously distributed following a general radial trend: they are enriched in the core (expected in the order of  $\mu\text{g/g}$ ), depleted in the mantle (in the order of  $\text{ng/g}$ ), and extremely rare in the crust (typically  $< \text{ng/g}$ ) (Table 1-1 and references therein). This radial distribution is especially pronounced for Os, Ir, Ru (i.e. the IPGE, Ir-like Platinum Group Elements) and Rh, while Pt, Pd (i.e. the PPGE, Pd-like Platinum Group Elements), Au and Re show more variable concentrations (Table 1-1).

**Table 1-1** HSE concentrations in different terrestrial reservoirs and CI chondrites.

	Os (ng/g)	Ir (ng/g)	Ru (ng/g)	Rh (ng/g)	Pt (ng/g)	Pd (ng/g)	Au (ng/g)	Re (ng/g)	$^{187}\text{Os}/^{188}\text{Os}$
Primitive upper mantle	3.9	3.5	7	1.2	7.6	7.1	1.7	0.35	0.1296
Residual mantle	2.74	2.89	5.47	0.84	4.16	1.73	0.95	0.09	
Oceanic crust	0.05	0.13	0.7		2.1	2.1		0.7	0.15
Continental crust	0.041	0.037	0.57	0.38	1.5	1.5	1.3	0.188	1.1
CI chondrite	449.5	418.4	627.2	130	871.4	567.4	148.8	36.6	0.1260

Primitive upper mantle estimates from Becker et al. (2006) except Rh and Au from Fischer-Gödde et al. (2011) and  $^{187}\text{Os}/^{188}\text{Os}$  from Meisel et al. (2001). The residual mantle is the average ( $n = 71-350$ ) of global non-orogenic harzburgite downloaded from the Georoc database (Max Planck Institute for Chemistry - Mainz - Germany, March 2015). Harzburgite from orogenic settings were excluded in order to do not include samples affected by subduction processes. Oceanic crust estimates from Peucker-Ehrenbrink et al. (2012). Continental crust estimates from Rudnick and Gao (2014). CI chondrite values are concentration averages from Fischer-Gödde et al. (2010).

#### 1.3.1 The origin of HSE in the mantle

The HSE are refractory elements as were among the first elements that condensed from the solar nebula (Lodders, 2003). Refractory elements are thought to have similar concentrations in the bulk Earth and in CI chondrites, a group of meteorites that is generally considered to be compositionally representative of the whole solar system

(McSween Jr and Huss, 2010; Palme et al., 2014). The HSE concentrations in the bulk silicate Earth is about two orders of magnitudes lower than in CI chondrites (Table 1-1). This relative depletion is thought to be caused by HSE scavenging into the Earth's metallic core during accretion and differentiation of our planet. Interestingly, even though HSE concentrations in BSE are much lower than those found in CI chondrites, their relative proportions are broadly chondritic (e.g. Becker et al., 2006, Table 1-1).

For several decades a plethora of experimental studies have tried to reproduce the conditions of core-mantle differentiation in order to explain the concentrations of HSE in the mantle. These studies reported HSE partition coefficients between silicates and metals that are typically  $> 10^4$  (e.g. Borisov and Palme, 2000; O'Neill et al., 1995). Thus, starting from a chondritic reservoir, the mantle after core formation is expected to contain  $> 50$  pg/g for each HSE, which is about two orders of magnitude lower than what is observed (Table 1-1). This experimental evidence, along with the fact that the relative HSE proportions of the BSE are similar those observed in CI chondrites, led many researchers to the conclusion that the HSE budget of the mantle is not fully controlled by an equilibrium process during core segregation, and that an additional process after core formation is required. The most accepted hypothesis is the so called "late veneer" (Kimura et al., 1974; Morgan, 1985; O'Neill et al., 1995). In this scenario it is assumed that a small portion of meteoritic material (chondrite-like) was added to an extremely HSE-depleted BSE after core formation. The contribution of the late veneer is estimated to be about 0.5-4.0% of the total mass of the BSE (Albarède et al., 2013; Ballhaus et al., 2013; Brenan and McDonough, 2009; Dauphas and Marty, 2002; Holzheid et al., 2000). The exact amount, the composition and the timing of this later addition are the subject of many recent studies and are still matter of debate (e.g. Albarède et al., 2013; Herwartz et al., 2014; Jacobson et al., 2014). However, it is largely accepted that the late veneer occurred in the Hadean (e.g. Albarède et al., 2013; Coggon et al., 2013; Morbidelli et al., 2012) and that the added material was likely fully homogenized in the mantle at the beginning of the Proterozoic (Maier et al., 2009; Willbold et al., 2011).

### ***1.3.2 Behavior of HSE during mantle melting***

Studies on primitive melts and mantle residues suggest a variable bulk partitioning of the HSE during mantle partial melting (Table 1-1; Day, 2013; Fischer-Gödde et al., 2011; Lorand et al., 2013; Pearson et al., 2004; Rehkämper et al., 1999). Osmium, Ir, and Ru are compatible elements, and become more concentrated in mantle residues. Conversely, Rh, Pt, Pd, Au, and Re show enrichment in basaltic melts and are consequently depleted in mantle residues. There is general agreement that bulk peridotite-melt partition coefficients follow the sequence:  $\text{Re} \leq \text{Au} < \text{Pd} < \text{Pt} \leq \text{Rh} < \text{Ir} \leq \text{Ru} \leq \text{Os}$  (e.g. Day, 2013; Fischer-Gödde et al., 2011; Lorand et al., 2013; Pearson et al., 2004). However, large variations in HSE concentrations and patterns are observed in different samples belonging to the same petrological type (i.e. basaltic melts or mantle residues) (Table 1-1). The observed variability of HSE concentrations in basalts and in mantle residues may be related to differences in pressure, temperature, and redox conditions during partial melting, as well as the extent of melting (e.g. Fonseca et al., 2012; Luguet et al., 2007; Mallmann and O'Neill, 2007; Mungall and Brenan, 2014; Rehkämper et al., 1999). Moreover, differences in source composition and the possibility of post-melting events (e.g. melt/fluid percolation in mantle residues and differentiation processes in basaltic melts) will likely lead to variability in HSE systematics (e.g. Alard et al., 2000; Ballhaus et al., 2006; Bézou et al., 2005; Dale et al., 2012; Harvey et al., 2010; Jenner et al., 2010; Lissner et al., 2014; Liu and Brenan, 2015; Lorand et al., 2013; Luguet et al., 2015).

In the Earth's mantle, the HSE are chalcophile with the partial exception of Re (see section 1.3.3). Because of this, the behavior of HSE during mantle melting is controlled by base metal sulfides (BMS), which, when present in the source, are the main host for these elements (up to 90% of the total HSE budget; Alard et al., 2000; Hart and Ravizza, 1996; Lorand et al., 2008a; Lorand and Alard, 2001).

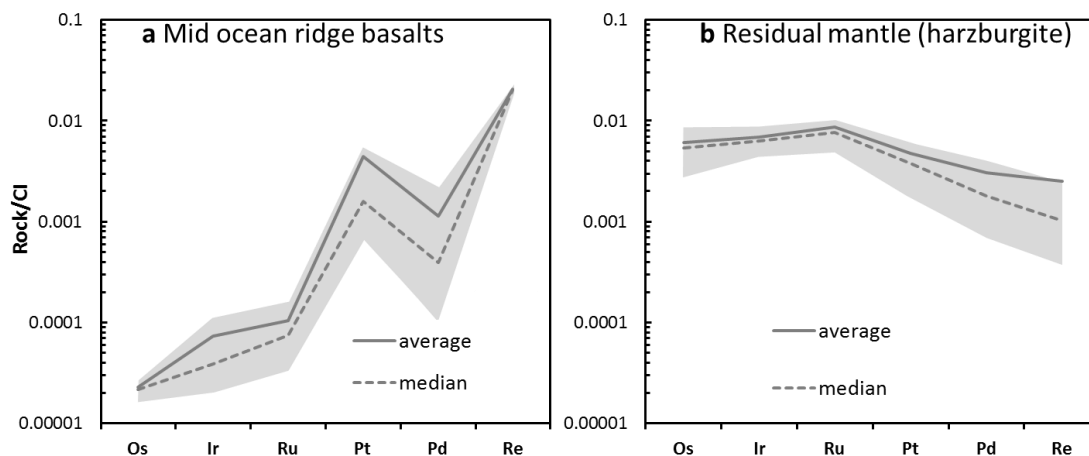


**Figure 1-5** HSE (Os, Ir, Ru, Pt, Pd, Re) in melts and residual mantle sources. a) Mid ocean ridge basalts (MORB) concentrations from a global compilation (Bézos et al., 2005; Lissner et al., 2014; Rehkämper et al., 1999; Tatsumi et al., 1999; Yang et al., 2014). b) Residual mantle concentrations from a global compilation of harzburgite (dataset downloaded from Georoc database in March 2015). The grey fields include the data between the first and the third quartile of the whole dataset.

During partial melting of the Earth's upper mantle, BMS are expected to be completely molten (Fonseca et al., 2012; Hart and Gaetani, 2006; Mungall and Brenan, 2014). For this reason, much effort was spent to infer the HSE partition coefficient between a sulfide melt and a silicate melt (cf. Mungall and Brenan, 2014 and references therein). A quantitative model to describe the behavior of HSE during partial melting is complex because the sulfide liquid, which retains the HSE in the mantle source, is continuously consumed due to sulfur dissolution in silicate melts (Haughton et al., 1974; Li and Ripley, 2009; Mavrogenes and O'Neill, 1999; Wallace and Carmichael, 1992). Moreover, S-exhaustion can be reached in the source depending on the initial sulfur content and the degree, pressure and temperature of partial melting. In particular, the total consumption of the sulfide liquid is favoured by high degrees of partial melting at low-pressure. Such conditions are expected in mid ocean ridges or back-arc basins but are unlikely for oceanic islands (Fonseca et al., 2011; Luguet et al., 2007).

A different scenario has been proposed to explain the HSE fractionation during mantle melting. According to some experimental data, sulfides can be partially molten during mantle melting (Ballhaus et al., 2006; Bockrath et al., 2004). Following these studies, the HSE budget is controlled by the partitioning of HSE between the sulfide solid phase (monosulfide solid solution) and the Cu-Ni rich sulfide liquid. In this case, the different

HSE patterns observed in basalts and mantle residues is explained by the physical removal of the sulfide liquid (enriched in Pt and Pd) via the rising silicate melt (Ballhaus et al., 2006).

At conditions in which sulfur is extremely depleted in a mantle source, BMS are no longer expected to be the main hosts of the HSE. Thus, other phases must host the HSE in the absence of BMS. Mass balance calculations based on mineral separates in S-free mantle rocks show that less than 30% of the HSE is contained in spinel and silicates (Luguet et al., 2007). Moreover, the solubility of IPGE is limited in silicate melts, as it is typically in the sub ng/g level (cf. Borisov and Palme, 2000; Ertel et al., 2008 for a review). Thus, due to the low solubility in silicate melts and the low concentrations observed in natural silicates and oxides, the IPGE are thought to form their own discrete phases as platinum group minerals, which include Ru-Os-Ir alloys and sulfides (e.g. laurite-erlichmanite) (Brenan and Andrews, 2001; Cabri and Weiser, 1996; Fonseca et al., 2012; Luguet et al., 2007, and reference therein). Other HSE, such as Pd, Re and Au are thought to leave the mantle source due to their higher solubility (up to  $\mu\text{g/g}$ ) in basaltic melts (Laurenz et al., 2010; Mallmann and O'Neill, 2007; Mungall and Brenan, 2014).

### **1.3.3 Rhenium**

In nature, Re occurs with two isotopes, the stable  $^{185}\text{Re}$  and the radioactive  $^{187}\text{Re}$ . The latter is the most abundant (62.6%) and decays to  $^{187}\text{Os}$  with a half-life ( $t_{1/2} = \ln(2)/\lambda$ ) of  $4.12 \cdot 10^{10}$  years (Smoliar et al., 1996).

During partial melting of the mantle, the Re bulk partition coefficient (i.e. the concentration of Re in the solid residue divided by that of the melt) has been compared to that of the heavy rare earth elements (HREE) (Schiano et al., 1997) or Ti (Mallmann and O'Neill, 2007). However, the geochemistry of Re is complex and unique since it can show lithophile, siderophile, or chalcophile behavior and can partition into a vapor phase depending on pressure, temperature, and oxygen fugacity (e.g. Lassiter, 2003; Sun et al., 2003). The different behavior of Re in high-temperature processes is largely controlled by its oxidation state, which in natural systems can be 0, +4, +6 and +7. In moderately reduced conditions, as expected in mid-oceanic ridges, Re occurs in the +4 and +6 oxidation states. During partial melting,  $\text{Re}^{4+}$  mostly partitions into sulfide phases (Fonseca et al., 2007),

clinopyroxene, and garnet (Mallmann and O'Neill, 2007). When present as  $\text{Re}^{6+}$  it behaves as an incompatible element and fractionates into the silicate melt (Brenan, 2008; Mallmann and O'Neill, 2007). Overall, under mid-oceanic ridge conditions, Re is slightly incompatible during partial melting (Mallmann and O'Neill, 2007). In more oxidized environments, like in arc settings, the dominant oxidation state is +6 and Re becomes more incompatible because its affinity for both silicates minerals and sulfide phases decreases (Brenan, 2008; Fonseca et al., 2007; Mallmann and O'Neill, 2007).

### ***1.3.4 Osmium***

In nature Os occurs with seven isotopes:  $^{184}\text{Os}$ ,  $^{186}\text{Os}$ ,  $^{187}\text{Os}$ ,  $^{188}\text{Os}$ ,  $^{189}\text{Os}$ ,  $^{190}\text{Os}$ , and  $^{192}\text{Os}$ . Two of these isotopes are the product of natural decay of radioactive isotopes:  $^{186}\text{Os}$  is produced from  $^{190}\text{Pt}$  by  $\alpha$ -decay (half-life  $4.7 \times 10^{11}$  years, Begemann et al. 2001) and  $^{187}\text{Os}$  by  $\beta$ -decay of  $^{187}\text{Re}$ . The two radiogenic isotopes  $^{187}\text{Os}$  (~2%) and  $^{186}\text{Os}$  (~1.6 %) are typically normalized to the stable  $^{188}\text{Os}$  (13.24%). The oxidation states of Os in nature are 0, +3, +4, +6, and +8. The most reduced form, 0, is observed in terrestrial and meteoritic alloys (Sakakibara et al., 2005) while the oxidized +8 is expected to be the main specie in seawater (Yamashita et al., 2007). In silicate melts, the most common oxidation state for Os is +3 (Fortenfant et al., 2006), but it might also occur in the +4 state in mantle sulfides and Pt group minerals (cf. Fonseca et al., 2011).

Under mantle conditions, Os is chalcophile and is hosted primarily by BMS phases provided that the mantle is BMS saturated. In a MORB-like setting, where S solubility in basalt is about 1000  $\mu\text{g/g}$  (Mavrogenes and O'Neill, 1999), a fertile mantle source (i.e. representing the BSE) is expected to be S-free after 15-20% partial melting took place (Fonseca et al., 2011; Luguet et al., 2007). It has been proposed that Os-rich sulfides and alloys may exsolve from the last remnant of mantle sulfides prior to complete S-depletion (Fonseca et al., 2011; Luguet et al., 2007). Recently Mungall and Brenan (2014) proposed that once the sulfide liquid is fully extracted the IPGE do not form alloys immediately but, for a certain extent of partial melting, are controlled by olivine. This is justified by the relatively high partition coefficient ( $> 1$ ) determined experimentally between olivine and silicate melts (Brenan et al., 2003). In this scenario Os alloys would form only after about 25% of partial melting (Mungall and Brenan, 2014). However, in natural depleted samples

(i.e. harzburgite), olivine usually contains only a marginal fraction of the bulk Os (< 20%) (Luguet et al., 2007), which suggests that this mineral plays only a small role in controlling Os during mantle melting.

#### ***1.4 MANTLE METASOMATISM AND ITS EFFECT ON THE HSE SYSTEMATIC AND THE RE-OS DECAY SYSTEM***

Metasomatism can be defined as metamorphism accompanied by changes in whole-rock composition (e.g. Winter, 2014). Therefore, the term metasomatism is used to identify a large variety of endogenic processes that involve a chemical exchange between a rock and the surrounding environment. These processes include reactions with fluids and melts that percolate/infiltrate in the host rock. In the mantle, metasomatic agents have a variable composition and they comprise silicate melts, carbonate melts/fluids, or aqueous fluids (e.g. Coltorti and Grégoire, 2008; O'Reilly and Griffin, 2013). Mantle metasomatism can affect the absolute and relative HSE concentrations (e.g. Ackerman et al., 2009; Lorand et al., 2013, 2008a; Reisberg et al., 2005). Since Pt, Pd, and Re are depleted in peridotites that underwent high degree of partial melting, these elements are particularly sensitive to metasomatism. As observed in many mantle suites, metasomatism in residual peridotites is typically displayed by an increase in Pd/Ir, Pt/Ir, and Re/Ir ratios (e.g. Irvine et al., 2003; Lorand et al., 2013; Maier et al., 2012; Pearson et al., 2004). However, it has been shown that the IPGE can also be affected by metasomatism (e.g. Ackerman et al., 2009; Büchl et al., 2002; Reisberg et al., 2005).

As observed for lithophile elements, the metasomatic agents change composition during their interaction with the mantle rocks, leaving behind mantle domains with variable chemical composition (Ionov et al., 2002). As a consequence, the trace element budget of metasomatized mantle rocks cannot be described by mass balance calculations where a metasomatic component is simply added to the original mantle rock. This is especially true for the HSE because they are mostly controlled by accessory phases, which can precipitate or dissolve owing to small scale chemical gradients. The complexity of the processes controlling the HSE during metasomatism is illustrated, for example, by the lack of clear correlation between proxies of melt/fluid addition based on lithophile elements (e.g. Nb,

Ba/Th) and HSE ratios clearly affected by metasomatism (e.g. Pd/Ir) (e.g. Chesley et al., 2004; Hanghøj et al., 2010). This lack of correlation also testifies that, similarly to what observed in magmatic processes, the lithophile elements and the HSE are controlled by different phases during metasomatism.

Melt percolation can have an important influence on the HSE budget. A melt, with a basalt-like composition, that percolates in peridotites can result in either precipitation or dissolution of BMS, depending whether the melt is saturated or undersaturated in sulfur (Ackerman et al., 2009; Büchl et al., 2002; Marchesi et al., 2014). The dissolution of BMS can lead to a decrease in the HSE content, which can vary depending on the melt/rock ratio (Büchl et al., 2002). There is evidence that metasomatic processes can affect HSE patterns, as well as the Re-Os system. For instance, the Re/Os ratio of peridotite may either increase or decrease by melts/fluids percolation. Rhenium, the most incompatible HSE, can be introduced during metasomatism by reaction with silicate melts (Ackerman et al., 2009; Chesley et al., 1999; van Acken et al., 2008), resulting in an increase over time of the  $^{187}\text{Os}/^{188}\text{Os}$  ratio. Conversely, other studies have shown that Re can also be removed after interaction with basalt-like melts (e.g. Reisberg et al., 2005). Osmium is thought to be less affected by metasomatism due to its compatible behavior in mantle conditions. However, it has been proposed that Os can be mobile under oxidizing conditions as expected in sub-arc mantle wedges (e.g. Saha et al., 2005; Suzuki et al., 2011; Woodland et al., 2002). The effect of mantle-metasomatism on the Re-Os decay system is also testified by the large scatter observed in  $^{187}\text{Re}/^{188}\text{Os}$  vs.  $^{187}\text{Os}/^{188}\text{Os}$  diagrams, which do not provide statistically significant isochrons neither for whole rocks nor for mineral separates (cf. Rudnick and Walker, 2009).

#### ***1.4.1 Residual and metasomatic BMS***

Upon closer inspection peridotites contain BMS with variable petrographic features, mineral composition, HSE signature and Os isotopic composition (e.g. Alard et al., 2011, 2002, 2000; Burton et al., 1999; Griffin et al., 2004; Harvey et al., 2011). The mineral assemblage of BMS included in silicates usually resembles that of high temperature monosulfide solid solution (mss). Included BMS show typically high IPGE content, low PPGE/IPGE, and unradiogenic  $^{187}\text{Os}/^{188}\text{Os}$ . Conversely, interstitial BMS grains often show

larger portions occupied by chalcopyrite (> 10% in volume) and pentlandite (up to 100%), and tend to be lower in IPGE, higher in PPGE/IPGE, and more radiogenic in  $^{187}\text{Os}/^{188}\text{Os}$  (e.g. Alard et al., 2011, 2002, 2000; Burton et al., 1999; Harvey et al., 2011). Based on these mineralogical and geochemical observations, it has been proposed that interstitial BMS grains are mostly metasomatic and can precipitate from silicate melts that percolate in the host rock (Alard et al., 2000; Lorand and Alard, 2001; Lugué et al., 2004). On the contrary, due to their textural position, BMS grains that are enclosed in silicates are less affected by metasomatism and their unradiogenic Os can be inherited from ancient melt depletion events (Alard et al., 2002, 2000). However, the Os isotopic composition recorded in BMS grains does not necessarily correlate with the petrographic setting of the grains. In fact, some BMS grains included in silicates can have radiogenic Os isotopic composition or less unradiogenic than other BMS grains from the same rock (Alard et al., 2002; Griffin et al., 2004; Xu et al., 2008). Moreover, besides the typical enrichment in PPGE/IPGE observed in sulfides formed after percolation of silicate melts, metasomatic sulfides can also show more complex HSE signatures, like super-chondritic Os/Ir as observed after interaction with volatile rich fluids (Alard et al., 2011; Delpech et al., 2012; Lee, 2002; Lorand et al., 2004).

From what observed on whole rock and single grain investigations, it is clear that the whole rock Os isotopic signature can be strongly affected by metasomatic processes as it carries the Os isotopic signature inherited from multiple sources (Figure 1-6). Therefore, the whole rock  $T_{\text{MA}}$  model age can lose any age significance and the  $T_{\text{RD}}$  model age can significantly underestimate the age of mantle melting events (Figure 1-6). The issues encountered in whole rock studies can be solved by investigations on the mineral scale because BMS (and PGM) have the ability to carry the original signature that was inherited from discrete events such as partial melting or metasomatic processes.

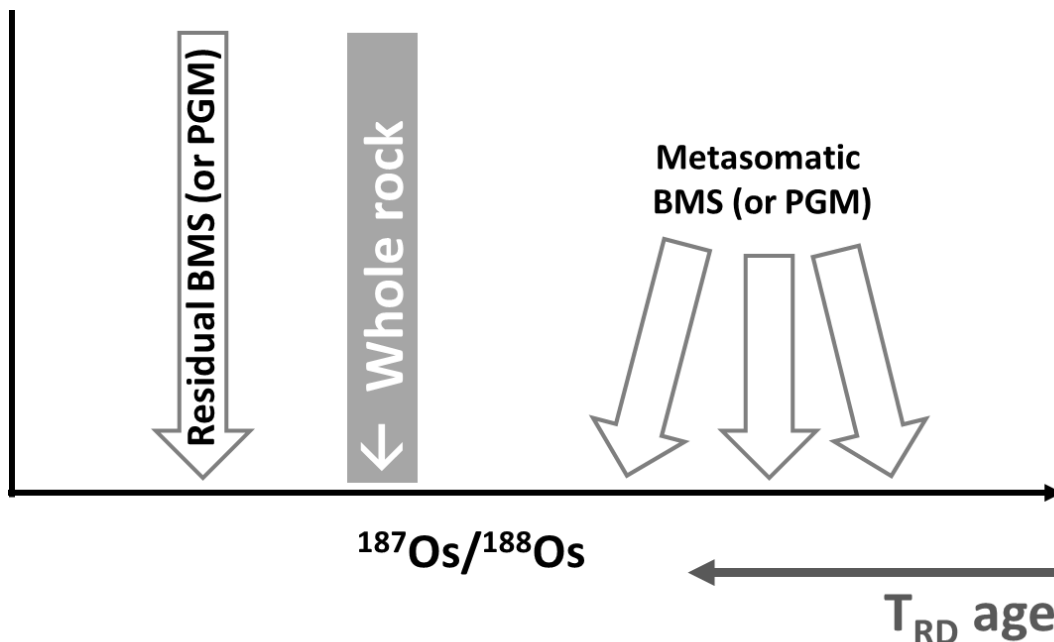


**Figure 1-6** Schematic illustration showing the  $^{187}\text{Os}/^{188}\text{Os}$  of residual and metasomatic BMS (and PGM) plus the corresponding whole rock. The whole rock Os isotopic composition provides only a minimum estimate ( $T_{RD}$  model age) for the melting age of the mantle rock.

## 1.5 MOTIVATIONS AND OUTLINE OF THE THESIS

### 1.5.1 The Canadian Shield

The Canadian Shield comprises many Archean terrains, including the Slave, the Rae, the Hearne, and the Superior cratons (e.g. Canil, 2008). Diamond exploration in the Canadian Shield started in the 1980s and received a new spin in 1991, after the discovery of the first economically exploitable kimberlite in the Lac de Gras area (Slave craton). Due to the industrial and scientific interest and the availability of material extracted by the mining activities, many mantle xenoliths have been studied to investigate the SCLM of the Canadian Shield. With the exception of the Victor mine, in the Superior craton, all the opened mines are located in the Slave craton. As a consequence, many studies have been focused on the SCLM beneath the Slave craton (e.g. Aulbach et al., 2011, 2004; Griffin et al., 1999; Heaman and Pearson, 2010; Irvine et al., 1999; Kopylova and Caro, 2004). In contrast, little is known about the deep continental roots beneath other portions of the

Canadian Shield, which also contain diamond-bearing kimberlites but are less economically exploited. Besides the Slave craton, the few available studies on mantle xenoliths from the Canadian Shield are limited to the Superior (e.g. Smit et al., 2014) and Rae (Irvine et al., 2003; Kjarsgaard and Peterson, 1992; Schmidberger et al., 2003, 2002, 2001; Schmidberger and Francis, 2001, 1999).

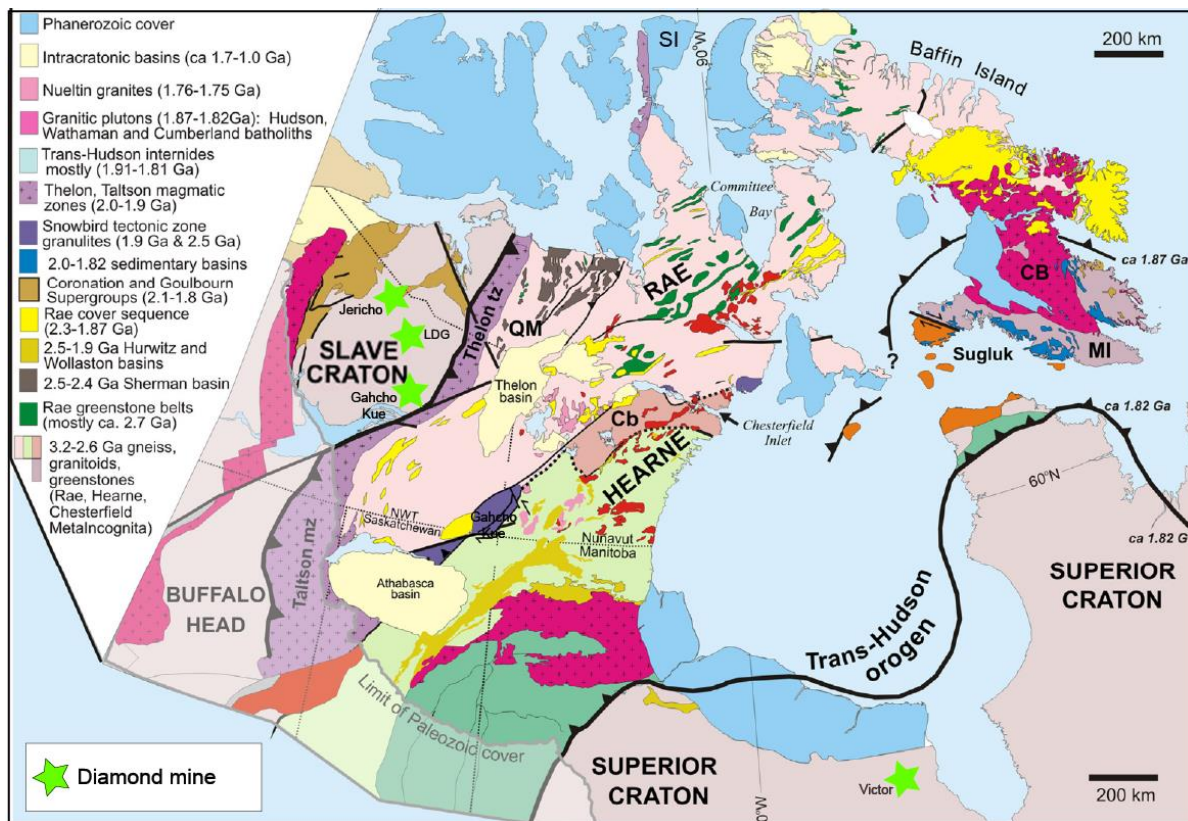


**Figure 1-7** Simplified geological map of the Canadian Shield (modified from Berman et al., 2005 and Pehrsson et al., 2013) showing the location for the diamond mines. QM-Queen Maud block, CB:Cumberland batholith, Cb:Chesterfield block, MI:MetaIncognita terrane, Wo:Wollaston group, WB:Wathaman batholith, SI:Somerset Island, LDG: Lac de Gras.

The SCLM beneath the Slave craton has been characterized with geophysical methods and by petrographic-geochemical investigations on mantle xenoliths from kimberlites (for a review see Heaman and Pearson, 2010). The SCLM of the Slave craton has a strong stratified structure with a shallow refractory layer and a deep more fertile domain (Carbo and Canil, 2002; Griffin et al., 1999; Heaman and Pearson, 2010; Irvine, 2001; Kopylova and Caro, 2004; Menzies et al., 2004; Stachel et al., 2003). Irvine et al. (1999) observed that mantle xenoliths from the north portion of the craton (Jericho mine), show  $T_{RD}$  ages

that are usually older (3.0-2.5 Ga) in the shallow spinel-bearing layer when compared to the ages of the more fertile and deeper garnet-bearing layer (2.8-1.2 Ga). The decrease in age with depth can be interpreted either as a primary feature with the formation of the two domains at different times (e.g. Aulbach et al., 2011; Griffin et al., 1999; Helmstaedt, 2009) or due to a metasomatic event in the deeper layer that caused a partial reset of the Re-Os isotopic system (Heaman and Pearson, 2010). In the central area of the Slave craton, seismic and geoelectric studies identified a volume of anomalous SCLM (Jones et al., 2003) that broadly correlates with the depth (100-150 km) of highly depleted peridotites xenoliths from the Lac de Gras kimberlite field (Griffin et al., 1999). An age of ~3.5 Ga was proposed for this layer on the basis of one isochron and one errorchron (i.e. an isochron with scatter exceeding the analytical error) obtained in sulfide inclusions from diamonds ( $3.52 \pm 0.17$  Ga isochron, Westerlund et al., 2006) and silicates ( $3.27 \pm 0.34$  Ga errorchron, Aulbach et al., 2004). However, the geological significance of these ages has been questioned as the isochron and the errorchron can also be described as mixing lines between two components with variable Re/Os and  $^{187}\text{Os}/^{188}\text{Os}$  (Pearson and Wittig, 2008). Regardless of the geological significance of the ~3.5 Ga isochron and the ~3.3 Ga errorchron, there is evidence from  $T_{\text{RD}}$  model ages that mantle xenoliths from the Slave craton record pre-Neoproterozoic depletion events. This is supported by the fact that among the analyzed samples, about 25% of the bulk peridotites and 10% of the peridotitic BMS yielded  $T_{\text{RD}}$  model ages  $\geq 2.9$  Ga (Aulbach et al., 2011, 2009, 2004; Irvine, 2001; Irvine et al., 1999; Westerlund et al., 2006). Overall, the oldest  $T_{\text{RD}}$  model age recorded in whole rocks is 3.1 Ga (Irvine, 2001; Westerlund et al., 2006) while one BMS included in olivine from Lac de Gras yielded a  $T_{\text{RD}}$  model age of  $3.9 \pm 0.3$  Ga (Aulbach et al., 2004). When  $T_{\text{RD}}$  model ages from whole rocks and BMS grains are combined in probability density plots, there is a clear predominant peak at ~2.8 Ga that was interpreted to date the main event of SCLM formation in the Slave craton (cf. Heaman and Pearson, 2010).

From what observed in the Slave craton, the Canadian Shield shows a variable Os isotopic signature, with a predominance of 2.8 Ga  $T_{\text{RD}}$  model ages and hints of older ages in more depleted and deeper lithologies. However, the exact time of formation of different portions of the SCLM is hampered by possible metasomatic events (e.g. Aulbach et al., 2013; Heaman and Pearson, 2010). A key tool to estimate the effect of metasomatism on

Re-Os ages is provided by a combined Re-Os study from whole rock and individual BMS grains. Unfortunately mantle xenoliths from the Slave and Superior cratons are typically too small (< 10 cm across, Kopylova and Caro, 2004) to be characterized for both whole rock and single BMS grain investigations. Larger xenoliths (up to 40 cm across) are recovered from Somerset Island (e.g. Irvine et al., 2003), in the north of the Rae craton.

A Re-Os geochronological investigation of BMS from Somerset Island, will therefore add important constraints to study the local SCLM in the framework of the Canadian Shield. It is of particular interest to ascertain if single BMS grains record Re-depletion events older than the whole rock (i.e. 2.8 Ga, Irvine et al., 2003), which would indicate a Meso or Paleoproterozoic history of the mantle roots beneath the Rae craton. This type of study will also reveal if the 2.8 Ga  $T_{RD}$  model age signature of the whole rock is mirrored at the mineral scale and if this age can be used to infer a major event in the formation of the local SCLM as observed in the Slave craton. A mineral scale investigation will also shed light on the effects of metasomatism in the SCLM beneath the Canadian Shield. This will further help to constrain the distribution of ages in the Canadian SCLM and can be used to highlight genetic relationships within mantle roots and crustal domains.

### ***1.5.2 Outline of the thesis***

The presented study included both, a case study from Somerset Island (Rae craton) (Chapter 2) and the development of an improved analytical technique (Chapter 3).

The suite of xenoliths analyzed by Irvine et al. (2003) from Somerset Island is further investigated in the second chapter of this thesis. Due to the large size of the xenoliths, it was possible to obtain several thin sections (up to 20) for the four analyzed samples. BMS grains were texturally and chemically characterized and 20 of them were analyzed for their Os isotopic composition. The analytical approach used in this thesis comprises the removal of individual BMS grains from thin sections before extracting the Os fraction via wet chemistry and measuring  $^{187}\text{Os}/^{188}\text{Os}$  via mass spectrometry (N-TIMS). This procedure, adapted from Pearson et al. (1998) differs from the more common LA-ICP-MS (laser ablation - inductively coupled plasma - mass spectrometry) as it allows measuring a larger fraction of BMS grains. In fact, LA-ICP-MS is applicable only to BMS grains that are larger than 50  $\mu\text{m}$  (Pearson et al., 2002), have  $^{187}\text{Re}/^{188}\text{Os} < 0.5$  (Nowell et al., 2008)

and contain at least 5-20  $\mu\text{g/g}$  of Os (Reisberg and Meisel, 2002), depending on the laser spot size. The Os isotopic variations observed at the mineral scale, along with the mineralogical/textural evidence, are used to constrain magmatic and metasomatic processes that are recorded by BMS grains. The age significance of  $T_{\text{RD}}$  model ages is then discussed in the context of the complex geodynamic setting of Somerset Island and the Rae craton.

The third chapter of this thesis is dedicated to the development of an improved analytical method to allow the analyses of  $^{187}\text{Os}/^{188}\text{Os}$  and HSE concentrations from the same BMS grain via wet chemistry. This approach will allow future studies to better constrain the origin of BMS grains thanks to the integration of the Re-Os geochronometer with the HSE signature, i.e. a proxy that can be used to discriminate genetic processes. The analytical procedure is set up using a sulfide standard that was synthesized and independently characterized for this scope.



*Chapter 2:*

OSMIUM ISOTOPIC COMPOSITION OF BASE METAL  
SULFIDES IN MANTLE XENOLITHS FROM SOMERSET  
ISLAND (CANADA)

**2.1 INTRODUCTION**

Ultramafic xenoliths hosted in kimberlites provide a unique opportunity to study the subcontinental lithospheric mantle (SCLM) below cratons. These xenoliths are fragments of the mantle lithosphere, which was mainly formed in the Archean as a residue of partial melting. Thus, these rocks can be dated to shed light on the time-scale of craton formation and they can be used to study the magmatic and metasomatic history of ancient mantle roots. Moreover, the horizontal and vertical age distribution within the SCLM provides essential information towards identifying the mechanism of cratonic formation (Lee, 2006; Pearson, 1999) as described in section 1.1.

Of all the geochemical tools at our disposal, the Re-Os decay system is the chronometer of choice to infer the melting age of mantle rocks (Carlson, 2005; Rudnick and Walker, 2009; Shirey and Walker, 1998; Walker et al., 1989). In mantle lithologies Re, Os, and the other highly siderophile elements (HSE) are controlled by platinum group minerals (PGM) and base metal sulfides (BMS) (Keays et al., 1981; Lorand et al., 2008b; Luguet et al., 2007). In particular, BMS are commonly observed as micro-phases (typically < 500µm across). Their origin can be residual or metasomatic (e.g. Alard et al., 2000; Lorand et al., 2010; Luguet et al., 2004, 2003). Residual BMS consist of sulfides that are left over in mantle rocks after a melting event, and their modal abundance decreases with increasing degree of partial melting. In contrast, metasomatic BMS can be introduced into residual peridotites via magma percolation (e.g. Alard et al., 2000; Luguet et al., 2004, 2003) or fluid infiltration (Alard et al., 2011; Delpech et al., 2012). Residual BMS are characterized

by unradiogenic Os, while metasomatic BMS typically contain more radiogenic Os (Alard et al., 2002). The whole rock Os isotopic composition and the Re/Os elemental budget are strongly affected by the presence of different generations (residual and metasomatic) of BMS (e.g. Alard et al., 2002; Griffin et al., 2004). Therefore, whole rock investigations, aiming to date melting events are hampered by widespread metasomatic processes. This issue can be overcome by analysing individual BMS because these phases can record information on single melting and metasomatic processes (e.g. Alard et al., 2002; Griffin et al., 2004).

Due to the new discovery and economic exploitation of kimberlite bodies, from the 1990s many mantle xenoliths became available for the investigation of the subcontinental lithospheric mantle (SCLM) below the Slave craton (Canada). Rhenium-Os investigations on peridotites (Irvine, 2001; Irvine et al., 1999; Westerlund et al., 2006) and BMS inclusions in silicates (Aulbach et al., 2004) show a predominance of Re-depletion ages ( $T_{RD}$ ) of ~2.8 Ga. This age was interpreted to date the major growth of the Slave SCLM (Heaman and Pearson, 2010). Similar Neoproterozoic model ages are also reported from mantle xenoliths of the Kaapvaal craton (e.g. Griffin et al., 2004; Irvine, 2001; Pearson et al., 2004, 1995a; Richardson et al., 2001; Simon et al., 2003), the Siberian craton (Griffin et al., 2002; Ionov et al., 2006; Pearson et al., 2004, 1995b), the North Atlantic craton (Wittig et al., 2010), the Tanzania craton (Chesley et al., 1999), the Superior craton (Smit et al., 2014), and the Rae craton (Irvine et al., 2003). In addition to the widespread occurrence of 2.8 Ga ages, the distribution of older and younger  $T_{RD}$  ages varies largely within and between cratons (cf. Heaman and Pearson, 2010).

Whole rock investigations on mantle xenoliths from Somerset Island (Rae craton, Canada) show oldest  $T_{RD}$  eruption ages of 2.7-2.8 Ga (Irvine et al., 2003; Table A-1), which are similar to those observed in other cratons and in the nearby Slave craton. Interestingly Irvine et al. (2003) observed a correlation between Re-Os model ages and HSE signature in this suite of samples. These authors showed that samples with a residual HSE signature (i.e. strongly depleted in Pt, Pd, and Re relative to Os, Ir, and Ru) yielded the oldest  $T_{RD}$  (or  $T_{RD}$  eruption) model ages of 2.7-2.8 Ga. In contrast, samples where Re

and Pd were clearly enriched during metasomatic events, show a large spread in  $T_{RD}$  ages (Irvine et al., 2003).

A Re-Os geochronology on individual BMS from these samples will provide constraints to understand the reliability of Re-Os model ages in whole rocks with increasing metasomatic HSE signature. This will help to distinguish events recorded in the cratonic SCLM, with particular regard to the evolution of the Canadian Shield. Rhenium-depletion model ages from BMS are here used to date melting and metasomatic processes and they are interpreted in the context of the geodynamic relationships between the Rae and Slave cratons.

## **2.2 GEOLOGICAL SETTING**

Somerset Island is located in the north of the Rae craton (Figure 2-1), which represents one of the fragments of the Canadian (Laurentian) Shield. The Rae craton is separated from the Slave craton to the north-east by the Taltson-Thelon Paleoproterozoic orogeny and from the Hearne craton to the south-west by the Snowbird zone (e.g. Berman et al., 2007; Hoffman, 1988). The Thelon orogen (Figure 2-1) extends to the Boothia Uplift (Hoffman, 1988) and represents the 1.9-2.0 Ga magmatic arc formed during the collision of the Slave and Rae craton. Historically the Rae and the Hearne cratons have been called the “Churchill province” along with the Early Proterozoic Trans-Hudson orogeny (e.g. Hoffman, 1988). Zircon U-Pb ages show the occurrence of Paleo-Mesoarchean terrains up to 3.7 Ga (Hartlaub et al., 2005). Most of the terranes consist of Neoproterozoic orthogneisses, greenstone belts and plutons, as well as Paleoproterozoic and younger intrusions (e.g. Ryan et al., 2009). The greenstone belts are confined to a small age range (e.g. Ryan et al., 2009; Young et al., 2007) and include the Woodburn Lake (2.74-2.63 Ga), Prince Albert (2.73-2.69 Ga) and Mary River (2.85-2.69 Ga) groups (Figure 2-1). Almost simultaneously (2.64-2.58 Ga), widespread granodioritic magmatism is recorded (Lecheminant and Roddick, 1991). The Archean terranes were intruded by Paleoproterozoic magmatism associated with the Macquoid (e.g. Pehrsson et al., 2013), Arrowsmith (e.g. Berman et al., 2013), Taltson-Thelon (e.g. Hoffman, 1988), and Trans-Hudson (e.g. Hollings and Ansdell, 2002) orogenies and by dyke swarms during the whole Proterozoic (Schetselaar and Ryan, 2009).

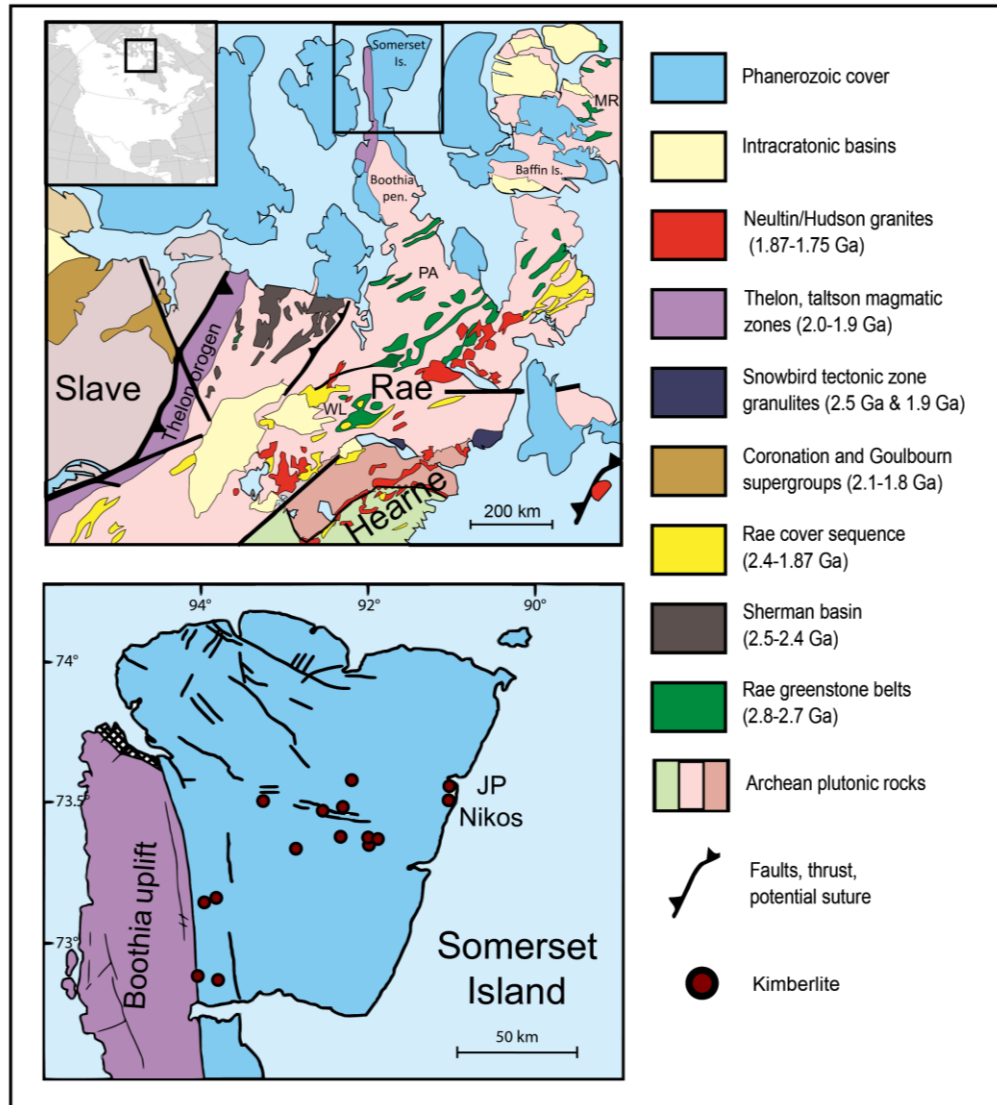


**Figure 2-1** On top: Simplified geological map of the Canadian Shield (redrawn after Berman et al., 2005 and Pehrsson et al., 2013). PA: Prince Albert group, WL: Woodburn Lake group, MA: Mary River group. On the bottom: inset of Somerset Island (redrawn from Wu et al., 2010).

Somerset Island is covered by Paleozoic sedimentary rocks mainly comprising limestone, dolomite, sandstone, siltstone, shale and conglomerate (Frisch, 2011). The sedimentary cover is thought to overlie the crystalline basement of the Boothia Uplift which outcrops in the eastern part of Somerset Island and in the near Boothia Peninsula (Stewart, 1987). Few U-Pb ages are available for the crystalline basement giving protolith ages of 2.5-2.2 Ga and metamorphic ages of 1.9-2.0 Ga (Frisch and Hunt, 1993; Hartlaub et al., 2007). The occurrence of 3.0-2.8 Ga Sm-Nd model ages hints to the presence of

Archean crust in the Boothia Uplift as also suggested by a 2.5 Ga xenocryst zircon from the Batty kimberlite (Parrish and Reichenbach, 1991). Kimberlites from Somerset Island are aligned along a SW-NE trend (Figure 2-1) following the orientation of fractures in the Precambrian basement that generated local weakness suitable for the emplacement of the diatremes (Mitchell, 1975). On a larger scale, the kimberlites from Somerset Island belong to the “Central Cretaceous corridor” (Heaman, 1989) formed during a continental event related to a crustal extension process or to a change in the Kula-Farallon subduction, which takes place on the west of North America since the Jurassic. The age of Somerset island kimberlites range between 88 Ma (Ham Kimberlite; Heaman, 1989) and 108 Ma (Peuyuk Kimberlite; Wu et al., 2010).

### ***2.3 MANTLE XENOLITHS FROM SOMERSET ISLAND***

Mantle xenoliths from seven kimberlites (Batty Bay, JP, Nikos, Elwin Bay, Nord, Nanorluk, Amayersuk) of Somerset Island have been extensively studied (Irvine et al., 2003; Kjarsgaard and Peterson, 1992; Mather et al., 2011; Mitchell, 1978, 1977; Schmidberger et al., 2003, 2002, 2001; Schmidberger and Francis, 2001, 1999; Smith et al., 1989; Wittig et al., 2008). According to the nomenclature introduced by Harte (1977), xenoliths from Somerset Island show coarse equant to coarse tabular texture and minor porphyroclastic texture (Irvine et al., 2003; Kjarsgaard and Peterson, 1992; Mitchell, 1978; Schmidberger and Francis, 1999). Garnet-peridotite is the dominant lithology but garnet-spinel and spinel peridotites are also reported along with rare dunites and garnet-pyroxenites (e.g. Irvine et al., 2003; Schmidberger and Francis, 1999). The P-T equilibration conditions for mantle xenoliths from Somerset Island vary between 1.5 and 5 GPa and between 650 and 1200 °C (Mather et al., 2011). Isotopic investigations on lithophile elements show that the Sr, Nd and Pb isotopic composition is inconsistent with a simple single-stage Archean melt extraction and that these three isotopic systems were variably affected by infiltration of the host kimberlitic magma (Schmidberger et al., 2001). A large Sr isotope variation (0.11%) was observed in different pyroxenes within individual xenolith and it was ascribed to the interaction with the kimberlitic magma (Schmidberger et al., 2003). An Archean 2.8 Ga age, although affected by a large uncertainty ( $\pm 0.8$  Ga), was

reported by Schmidberger et al. (2002) on the basis of a Lu-Hf errorchron on mantle xenoliths from Nikos kimberlite.

Rhenium-Os model ages corrected for the age of the host magma (i.e.  $T_{RD}$  eruption ages), display a variation between 1.4 and 2.8 Ga, with most of the samples grouped in the 2.0-2.7 Ga range (Irvine et al., 2003, Table A-1). From the perspective of the Re-Os systematic, the suite of samples investigated by Irvine et al. (2003) show some peculiar and interesting features. Xenoliths with whole rock  $^{187}\text{Re}/^{188}\text{Os}$  in excess of 0.6 are positively correlated with  $^{187}\text{Os}/^{188}\text{Os}$  ratios (Figure 2-2A). The samples aligned along this trend define an errorchron of  $94 \pm 24/-20$  Ma (“robust regression”, isoplot Ludwig 2003), which overlaps with the kimberlite emplacement age (93-108 Ma: Wu et al., 2010). The observed trend could also be explained by mixing during post-emplacement alteration such that the age obtained with the errorchron is simply coincidental. However, this scenario is unlikely because no correlation is observed in an  $^{187}\text{Os}/^{188}\text{Os}$  vs.  $1/\text{Os}$  plot (Figure 2-2B). Xenoliths aligned along this trend show a correlation between  $^{187}\text{Re}/^{188}\text{Os}$  and Re but not Os, therefore the errorchron corresponded to a variable Re enrichment processes related to the kimberlite eruption. The initial  $^{187}\text{Os}/^{188}\text{Os}$  of the errorchron is  $0.1094 \pm 0.0006$ , which is similar to that of the primitive mantle (Meisel et al., 2001) at 2.64-2.81 Ga. This time range overlaps with the oldest  $T_{RD}$  eruption age recorded in Somerset Island (Table A-1).

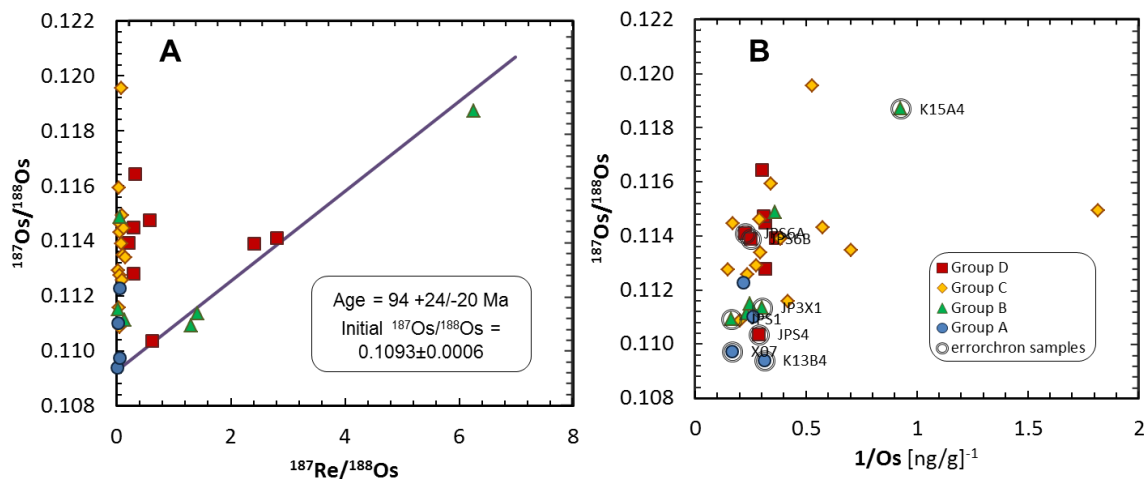


**Figure 2-2** A) Rhenium-Os isochron diagram for whole rock xenoliths from Somerset Island. The purple line represents an errorchron with an age of 94 Ma. All calculations were performed using the “robust regression” of isoplot (Ludwig, 2003). B)  $1/\text{Os}$  vs.  $^{187}\text{Os}/^{188}\text{Os}$  diagram. The samples that were used for errorchron calculations are highlighted by a grey circle. Blue circles belong to group A; green triangles belong to group B; yellow diamonds belong to group C; red squares belong to group D (Irvine et al., 2003). All data are from Irvine et al. (2003).

### 2.3.1 Description of the studied samples

The present study is based on the suite of 33 samples already investigated by Irvine et al. (2003) and Wittig et al. (2008). These xenoliths consist of coarse equant harzburgites and lherzolites. The whole rock major element composition is characterized by relative small variation in  $\text{SiO}_2$  (43-46 wt.%),  $\text{MgO}$  (40-48 wt.%), and  $\text{FeO}$  (6.9-8.3 wt.%). Despite an overall homogenous major element composition, the whole rock  $\text{Al}_2\text{O}_3$  and  $\text{CaO}$  contents vary between 0.1 and 3.3 wt.%, and 0.3 and 3.4 wt.%, respectively. The concentrations of  $\text{TiO}_2$  and  $\text{Na}_2\text{O}$  are always lower than 0.25 wt.% and 0.1 wt.%. The depleted nature of these xenoliths is testified by the high  $\text{Mg}\#$  ( $\text{Mg}\# = \text{Mg}/[\text{Mg} + \text{Fe}]_{\text{at}}$ ) of olivine, which varies from 0.917 to 0.926. Rare earth elements (REE) patterns show that samples from this suite are enriched in light REE relative to heavy REE, with  $\text{La}/\text{Lu}_N$  (i.e. the CI-normalized  $\text{La}/\text{Lu}$  ratio, McDonough and Sun, 1995) ranging between 3 and 87 (Wittig et al., 2008).

Irvine et al. (2003) subdivided this suite of xenoliths into four groups on the basis of the HSE signature. Group A and B show the most residual CI-normalized HSE pattern with a progressive depletion in Pt and Pd relative to the IPGE (i.e. Os, Ir, Ru), while group C and

D are variably enriched in Pd/Pt. Group B and D are distinguished from group A and C for an enrichment in Re relative to Pd. Interestingly, Irvine et al. (2003) observed that the oldest  $T_{RD}$  eruption ages are usually observed in samples from groups A and B, while group C and D show typically younger  $T_{RD}$  eruption ages. For the present study, the four samples X07, JPN11, JPN3A and JPS6A of Irvine et al. (2003) were selected because they are representative for the petrological and HSE chemical variability observed in the whole suite of samples. The four investigated xenoliths, belong to each different HSE group of Irvine et al. (2003) (Figure 2-3). Following this classification, and for the sake of clarity, samples X07, JPN11, JPN3A and JPS6A will hereafter be referred as A, B, C and D, respectively.

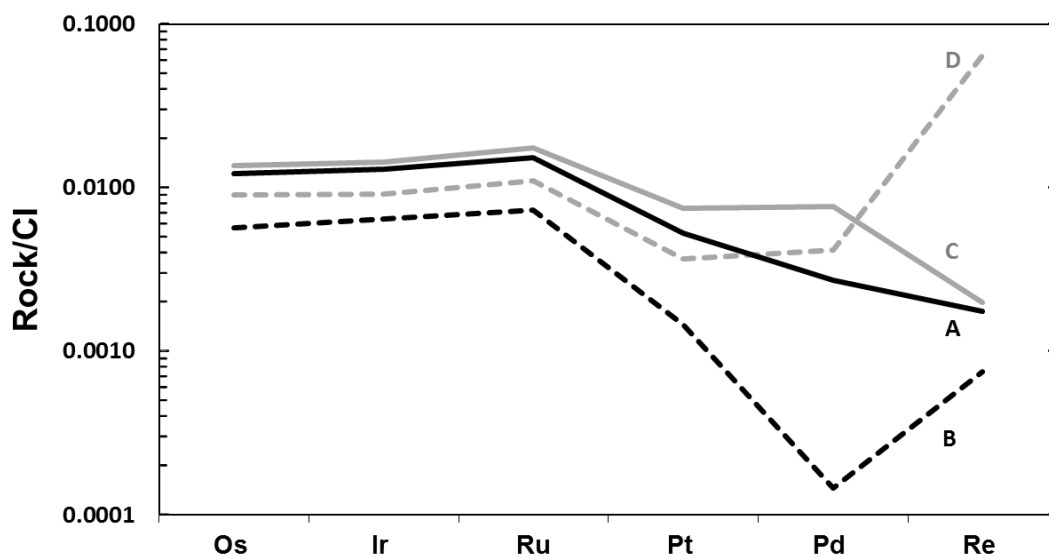


**Figure 2-3** HSE pattern of the selected samples normalized to CI-chondrite (Irvine et al., 2003). Black line : A; dashed black line : B; grey line : C; dashed grey line : D.

Sample A is a garnet-spinel harzburgite with low  $Al_2O_3$  content (0.21 wt.%), samples B, C and D are garnet lherzolites with variable  $Al_2O_3$  content (0.72, 1.14, 1.47 wt.%). Sample A shows a  $T_{RD}$  eruption age of 2.69 Ga and a  $T_{MA}$  of 3.04 Ga. In the Re-Os isochron diagram (Figure 2-2), this sample plots close to the intercept of the 94 Ma errorchron. Sample B and C display  $T_{RD}$  eruption ages of 2.01 and 2.29 Ga, and  $T_{MA}$  of 2.30 and 2.62 Ga, respectively. Sample D lies on the 94 Ma errorchron, and it has an extremely high  $^{187}Re/^{188}Os$  of 2.8, which results in an unrealistic  $T_{MA}$  and in an unprecise  $T_{RD}$  eruption age of  $2.72 \pm 0.09$  Ga (2SD, i.e. two times the standard deviation). Additional

petrographic observations on samples A, B, C and D show a variable degree of serpentinization (10-20%). Sample D also contains carbonate rich veins. Olivine in the four samples reaches 1 cm in size and shows large fractures filled with a fine serpentine matrix. Orthopyroxene is smaller (1-3 mm) and it is less fractured when compared to olivine, with the exception of sample D where large portions of orthopyroxene (10-30%) are altered and filled with the serpentinite matrix. Moreover, the orthopyroxene in this sample is commonly surrounded by a rim of clinopyroxene (~10  $\mu\text{m}$  in size). The grain size of garnet varies between few mm and 1 cm and shows kelyphitic rims containing euhedral spinel. Large spinel (hundreds of  $\mu\text{m}$ ), not associated with garnet, is only observed in sample A. Clinopyroxene, absent in sample A, has a round shape and occurs as clusters or small chains. The kelyphitic rim around the garnet in samples C and D also contains phlogopite.

## **2.4 ANALYTICAL METHODS**

Between 7 and 20 thin sections (~200  $\mu\text{m}$  thickness) were prepared from each sample. Thin sections were investigated using transmitted and reflected light microscopy prior to microprobe and  $^{187}\text{Os}/^{188}\text{Os}$  analyses. Moreover, an aliquot of the nodules was coarsely crushed using a disk mill and used for hand-picking additional BMS grains.

### **2.4.1 Microprobe analyses**

Silicates and sulfides were analyzed using a JEOL JXA 8900 electron microprobe (Steinmann Institut, Universität Bonn, Germany). The measurements were performed using 15 kV acceleration voltage, 15 nA beam current, and 1  $\mu\text{m}$  beam size. Sulfides were analyzed for S, Fe, Ni, Co, Cu, K and O content. Sulfur and Fe were calibrated on the Canyon Diablo troilite, Ni, Co, Cu on pure metals, K on microcline. Oxygen was measured with LDE1 crystal on the  $K\alpha$  line and calibrated on MgO. Silicates were analyzed for MgO,  $\text{Al}_2\text{O}_3$ , FeO, CaO,  $\text{TiO}_2$ ,  $\text{SiO}_2$ ,  $\text{Cr}_2\text{O}_3$ ,  $\text{Na}_2\text{O}$ ,  $\text{K}_2\text{O}$ , MnO and NiO. Calibration on silicates was performed using conventional silicate standards.

### ***2.4.2 Base metal sulfides microsampling***

The routine procedure to extract BMS grains from natural samples consists in hand-picking from a coarsely crushed rock (Aulbach et al., 2010; Burton et al., 2012; Dale et al., 2009; Gannoun et al., 2007, 2004; Harvey et al., 2011, 2010, 2006). In this study, some BMS have been collected using this technique which, however, does not allow a full textural and mineralogical characterization. To preserve this information, here, most of the studied BMS grains were extracted from thin sections. A simple technique to remove BMS from thin sections was proposed by Warren & Shirey (2012) using a diamond scribe. However, during the present study the use of a diamond scribe without a pre-isolation of the grain was found to often result in the loss of portions of the sulfides. For this reason, two new procedures were developed in the present study to precisely extract individual BMS grains from thin sections.

#### ***2.4.2.1 Extraction via MicroDrill***

The silicates surrounding the BMS grains were removed from thin sections using a NewWave Research MicroDrill combined with a Q-Finishers (Komet USA) tungsten carbide mill bit. In this case, the thin sections were prepared with acetone-dissolvable glue. The conical shape of the mill bit has a small tip (200  $\mu\text{m}$ ) and it allows a relative precision in the drilling process. Several linear passes were made to progressively mill the silicates until reaching the glue layer at the bottom of the section. With this procedure it was possible to isolate a small portion containing the BMS grain. After soaking for 1 hour in acetone (80 °C), the isolated volumes were removed from the thin sections using a stainless steel needle. In order to completely remove the glue, samples were rinsed at least twice in acetone and finally in ultrapure water ( $\text{H}_2\text{O}$ -MQ).

#### ***2.4.2.2 Extraction via Excimer Laser ablation***

The laser ablation apparatus (Resonetics M50-E ATL excimer 193 nm) of the Steinmann Institut (Universität Bonn) was used to ablate the silicates around the BMS grains. With this technique, transmitted light pictures were used to define the ablation path in order to prevent any loss of sulfide portions that are not exposed on the surface. A small rim of silicates around most of the grains was additionally preserved to avoid any thermal shock inside the BMS and to compensate for any possible offset of the laser optics. Laser

pulses with a spot size of 20  $\mu\text{m}$  and ablation rate of 15-20 Hz were applied while moving the sample stage at a speed of 0.3-0.4  $\mu\text{m}/\text{sec}$ . These settings can be slightly modified according to the thickness of the section as well as the size of the BMS grain. The measured laser fluence was  $\sim 10 \text{ J}/\text{cm}^2$ . The surface was then cleaned with ethanol to remove any dust and particles that may have settled on the surface of the sample during the laser ablation process. Extraction of the BMS grain from the surrounding silicates was achieved after widening the ablated path with a diamond scribe under a binocular microscope. The BMS grain was subsequently removed from the thin section and transferred to a pre-cleaned small container.

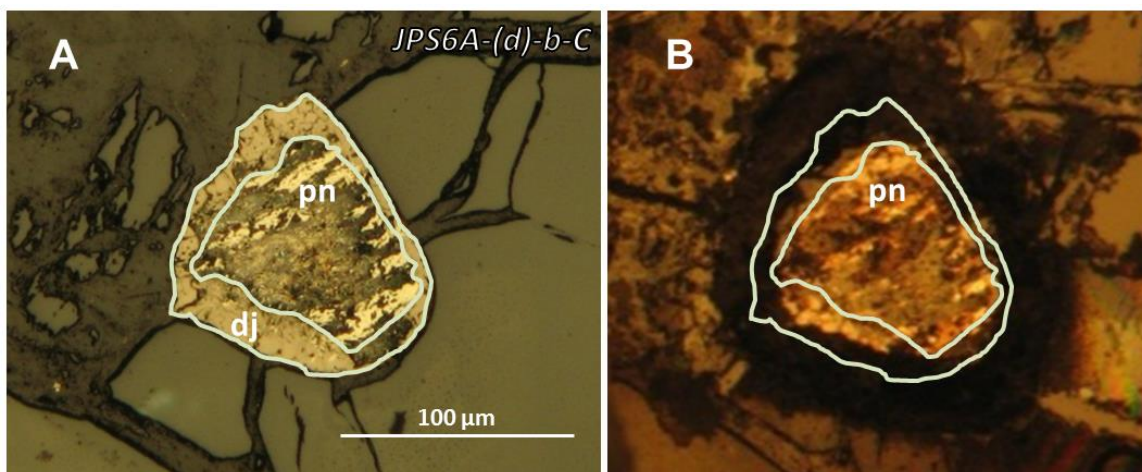


**Figure 2-4** A) microphotograph of a pseudoinclusion in olivine (grain JPS6A-(d)-b-C), which consists of a core of pentlandite (pn) surrounded by an overgrowth of djerfisherite (dj) B) Microphotograph of the same grain after ablating most of the djerfisherite corona. The leftover djerfisherite was removed while extracting the BMS grain from the thin section.

#### 2.4.2.3 Comparing microsampling techniques

Both procedures were tested extensively on grains of different sizes (30-500  $\mu\text{m}$ ), and the results of these tests show that both the MicroDrill and the laser apparatus can be used to successfully extract BMS from thin sections. The advantages of the Microdrill reside in the simplicity of the technique: it can be used by a single operator after short training, it is fast (one BMS grain can be extracted in about 20 min) and the consumable cost is limited as one mill bit can be used for several extractions. However, the MicroDrill does not enable to drill directly into silicates at the edge of the BMS because the grain can become detached from the thin section and get destroyed by the mill during the process. Therefore, a

minimum radius of 200  $\mu\text{m}$  from the center of the grain is necessary to minimize such a risk. This limitation is overcome when the BMS grain is extracted via laser ablation. Importantly, the high spatial resolution of the laser also allows selective investigation of different portions of individual grains (Figure 2-4), which can be essential in the case of BMS that are surrounded by overgrowth of metasomatic phases.

### ***2.4.3 Osmium chemical separation and N-TIMS analyses***

Single BMS collected with different micro-sampling techniques were individually digested following the protocol of Pearson et al. (1998). According to this procedure, a spike solution (enriched in  $^{190}\text{Os}$  and  $^{185}\text{Re}$ ) was added to the samples to determine Os and Re contents. As shown in section 3.4, the Os and Re concentrations obtained with this technique are not reliable. Therefore, only  $^{187}\text{Os}/^{188}\text{Os}$  isotopic ratios are presented and discussed in this section. The analytical procedure includes the digestion of the BMS in 20  $\mu\text{L}$  of a  $\text{Cr}^{6+} + \text{H}_2\text{SO}_4$  solution on the lid of a PFA Savillex conical vial. The beaker, containing a drop of HBr on the top, is placed on a hotplate for two hours at 80  $^\circ\text{C}$ . The HBr fraction is then dried down and used for Os measurements. Further details on the analytical procedure are given in section 3.2.3.

Measurements of the  $^{187}\text{Os}/^{188}\text{Os}$  isotopic ratio from individual BMS grains were carried out at the Northern Centre for Isotopic and Elemental Tracing (NCIET) of the University of Durham using a TIMS (ThermoScientific Triton) in negative mode. All Os isotopes were measured as  $\text{OsO}_3^-$  on a SEM in peak jumping mode. The measurements were corrected for mass bias and oxygen isotopic composition (for more details see Dale et al., 2008; Luguet et al., 2008 and section 3.2.4).  $^{185}\text{ReO}_3^-$  was measured in order to estimate any possible isobaric interference of  $^{187}\text{ReO}_3^-$  on  $^{187}\text{OsO}_3^-$ . Four measurements of 10-100 pg of the in-house standard DROsS (Luguet et al., 2008) yield an average  $^{187}\text{Os}/^{188}\text{Os}$  of 0.16090 (SD = 0.00011,  $n = 4$ ), which is in excellent agreement with the values reported in the literature for 10-100 ng loads of Os (e.g.  $0.16092 \pm 0.000004$ , Luguet et al., 2008).

As already stated Os concentrations are not reliable and in section 3.4.1 it is shown that this analytical procedure overestimate the Os concentration, up to a factor of almost three. Both BMS grains and blanks are similarly affected by this issue, which is likely due to

spike loss (see section 3.4.1). Therefore, despite the extreme lack of accuracy, Os concentrations can be used to assess any possible blank contribution. The average Os concentrations measured in five procedural blanks is 0.2 pg (SD = 0.1 pg). The majority of the BMS grains yielded Os concentrations > 20 pg, and therefore it is possible to exclude for them any significant blank contribution (> 1%). The remaining two BMS grains yielded Os concentrations of 4 pg (JPN3A-a-D) and 9 pg (JPS6a-d-A). However, the high  $^{187}\text{Os}/^{188}\text{Os}$  (> 0.13) measured in these two BMS grains makes any possible small blank contribution negligible for the interpretation and discussion of the data. Two BMS grains (SGSM01 and SGSM02) were not spiked. The Os measurements of these two grains yielded  $^{192}\text{OsO}_3$  intensities of  $2 \cdot 10^4$  and  $4 \cdot 10^4$  cps, which are in the range of those obtained from other BMS grains (typically between  $10^4$  and  $10^5$  kcps), and significantly lower than those measured in procedural blanks (typically < 500 cps). Therefore any significant blank contribution for these two measurements can be excluded.

A possible issue of BMS grains extracted with MicroDrill sampling is related to the silicates placed around the analyzed grains. Optical observations on the leftover after the micro-distillation reveal an almost intact silicate portion. However, the Os contained in silicates can be potentially liberated (e.g. leached) during  $\text{CrO}_3 + \text{H}_2\text{SO}_4$  digestion. Silicate phases usually contain < 1 ppb of Os (Luguet et al., 2007; Wittig et al., 2010). Assuming a content of 1 ppb in the silicates around the sulfides and an extracted volume of  $0.025 \text{ mm}^3$  (a cylinder of 0.2 mm thickness and 0.2 mm radius), the expected total amount of Os is < 0.1 pg, which is lower than the average procedural blank.

## 2.5 RESULTS

### 2.5.1 Silicate mineral chemistry and geothermobarometry

Olivine from the four samples shows only a small variation in Mg# between 0.919 and 0.927. NiO and CaO are in the range of mantle values, respectively at ~0.4 and 0.05 wt.%. Orthopyroxene is enstatite-rich (Mg# = 0.927-0.936) and its composition is almost constant with 1.3 wt.%  $\text{Al}_2\text{O}_3$ , 0.6-0.7 wt.% CaO, 0.4-0.6 wt.%  $\text{Cr}_2\text{O}_3$ . Clinopyroxene is rich in  $\text{Cr}_2\text{O}_3$  (up to 2.5 wt.%) and  $\text{Na}_2\text{O}$  (up to 2.3 wt.%) and poor in  $\text{TiO}_2$  (< 0.3 wt.%). The Mg#

of clinopyroxene is constant (0.93-0.92), CaO varies between 18.3 and 19.6 wt.%, and Al<sub>2</sub>O<sub>3</sub> between 2.3 and 3.1 wt.%. The garnet is Cr-rich pyrope with 20-21 wt.% MgO and 18-22 wt.% Al<sub>2</sub>O<sub>3</sub>. The Cr<sub>2</sub>O<sub>3</sub> content of garnet is between 4 and 9 wt.% and CaO varies between 4.7 and 6.3 wt.%, while FeO is almost constant (5.9-6.7 wt.%). Overall, silicates mineral chemistry is in agreement with the literature data for Somerset Island (Irvine et al., 2003; Kjarsgaard and Peterson, 1992; Schmidberger and Francis, 1999). No chemical zonation was observed within silicates.

Analyses on silicates were used to infer the P-T equilibration conditions of the xenoliths. Recent reviews by Nimis and Grütter (2012, 2010) pointed out that the two-pyroxene thermometer, initially proposed by Taylor (1998), is the most reliable one for lherzolites, while the orthopyroxene-garnet thermometer of Nimis and Grütter (2010) is the best suited for clinopyroxene-free samples (i.e. harzburgites). The same authors suggested the use of the orthopyroxene-garnet barometer (Nickel and Green, 1985). The combination of the two-pyroxene thermometer with the orthopyroxene-garnet barometer gives for samples B, C and D pressures of 3.9, 4.0 and 3.7 GPa and temperatures of 1070, 1060 and 1040 °C, respectively. The small variation in P-T is comparable to the analytical uncertainties and suggests that the three samples equilibrated at similar depth (~130 km) and temperature. The same orthopyroxene-garnet barometer combined with the orthopyroxene-garnet thermometer gives a larger range in P-T estimates, with pressures of 4.0, 3.9, 4.5, and 3.6 GPa and temperatures of 1067, 1067, 1181, and 1019 °C for samples A, B, C and D, respectively. All the P-T estimates are in agreement with the range of published ones obtained in Somerset Island using the same geothermobarometers (i.e. 1.5-5 GPa and 650-1200 °C, Mather et al., 2011).

### 2.5.2 *Base metal sulfides*

Hereafter, the name of the analyzed BMS grains will follow the criteria described in the example below:

JPS6A	-(d)	-b	-C
Xenolith name of Irvine et al. (2003)	HSE group of Irvine et al. (2003)	Thin section	BMS grain

BMS modal abundances vary between samples. If we exclude the ubiquitous small sulfides (usually  $< 5 \mu\text{m}$ ) inside the serpentine matrix veinlets, the number of BMS grains observed for each thin section of a given sample varies between zero and eight. Base metal sulfides are rare in sample A and especially in B. The average exposed BMS grains per thin section is about one for sample A (nine BMS grains exposed over 10 thin sections) and 0.25 for sample B (five BMS grains exposed over 20 thin sections). BMS are more abundant in samples C and D where, on average, more than four grains are observed per thin section (29 and 44 BMS grains exposed over seven and ten thin sections, respectively). The BMS grains are heterogeneously distributed also within a given sample. In sample C and D, the distribution of BMS is not uniform across the thin section as BMS grains are often concentrated in discrete areas (up to five large BMS grains over  $1 \text{ cm}^2$ ). Sample A and B, show a similar heterogeneous distribution of BMS as testified by two large BMS grains distant by  $\sim 1 \text{ cm}$  in one thin section of sample B.

#### 2.5.2.1 *Habitus and textural relationships*

Based on their habit and textural relationships, BMS grains can be subdivided in four distinct groups (Figure 2-5):

1) Inclusions consist of BMS blebs located within one single silicate crystal. They have a round or ovoid shape with a diameter ranging usually between 20 and  $250 \mu\text{m}$ . They are hosted in olivine, orthopyroxene, clinopyroxene and garnet. Sometimes, decrepitation trails can extend into the host phase in the form of chains of small round sulfides ( $< 2 \mu\text{m}$ ).

Only five inclusions appear to have no connection with the serpentine-rich veins. These BMS blebs are the only ones showing a surface fully occupied by preserved sulfides and they will be called hereafter isolated inclusions. Four of them are included in olivine (JPN11-(b)-0-A, JPS6A-(d)-0-F, JPS6A-(d)-a-C, JPS6A-(d)-a-B) and one in orthopyroxene (X07-(a)-a-F). Isolated inclusions consist of different sulfide phases such as monosulfide solid solution (mss), pentlandite, chalcopyrite and pyrrhotite. X07-(a)-a-F consists of a complex association of pentlandite and pyrrhotite in similar proportion (Figure 2-5). The largest portions ( $> 80\%$ ) of the other four isolated inclusions are made of fine exsolution lamellae ( $< 1 \mu\text{m}$ ). The only mineral that is clearly distinguished in these areas is mss, while other phases are too small to be identified (JPN11-(b)-0-A and JPS6A-(d)-0-F in

Figure 2-5). Chalcopyrite is observed only on the rim of two isolated inclusions (up to about 15% of the surface, JPS6A-(d)-0-F in Figure 2-5). Relatively large portions ( $> 10 \mu\text{m}$ ) of pentlandite can also occur as patches on the rim of BMS blebs (JPN11-(b)-0-A in Figure 2-5) or along the boundary between chalcopyrite and the rest of the BMS bleb (JPS6A-(d)-0-F in Figure 2-5).

In contrast to isolated BMS blebs, the majority of the inclusions are clearly connected to the serpentine matrix through a network of large veins (several  $\mu\text{m}$  across). Such BMS show alteration features with variable portions (20-60%) of the original mineral assemblage being filled with serpentine and magnetite. The alteration is often concentrated in the core of the BMS blebs (JPN3A-(c)-d-C in Figure 2-5). The preserved areas consist mostly of pentlandite (up to 100%). Chalcopyrite is observed on the majority of the rims, occupying  $< 5\%$  of the total surface. Micrometer-sized heazlewoodite and Cu-sulfides (chalcocite or digenite) were seldom observed along rims. About half of the BMS inclusions of sample D are surrounded by 10-100  $\mu\text{m}$  thick coronae of djerfisherite (JPS6A-(d)-d-A in Figure 2-4). Small round blebs or rods (usually  $< 1 \mu\text{m}$ ) of pentlandite are spread inside the djerfisherite coronae of BMS grains (Figure 2-6A-B). Pyrrhotite and mss were not observed in BMS inclusions that are in contact with the vein network.

2) Pseudoinclusions are BMS grains partially included in the host phases and partially exposed to serpentine matrix. Only one grain clearly belongs to this group (JPS6A-(d)-b-C, Figure 2-4). It has an ovoid shape, with the two axes being  $\sim 100$  and  $\sim 80 \mu\text{m}$  long. This pseudoinclusion is made of an altered pentlandite core and a corona of djerfisherite ( $\sim 10 \mu\text{m}$  thick).

3) Large interstitial BMS grains are up to  $500 \mu\text{m}$  in size and were found at the grain boundary between olivine, garnet and pyroxene. Their shape is more irregular than that of inclusions and they often show small dihedral angles ( $\ll 90^\circ$ ). Large interstitial BMS grains are observed only in sample C ( $n = 3$ ) and D ( $n = 1$ ). Like the inclusions connected to veins, large interstitial blebs display altered cores with preserved rims of pentlandite. The large interstitial BMS grain from sample D shows a djerfisherite corona with minor pentlandite, similar to what is observed in BMS blebs included in silicates from the same sample.

4) Small interstitial BMS grains are generally  $< 5 \mu\text{m}$  in size and occur exclusively within the serpentine veins. They tend to be elongated following the direction of the veins and may cluster to form chains of tens of  $\mu\text{m}$ . In every sample the majority of the small interstitials consist of Ni-sulfide in the form of heazlewoodite (sample A, B and C) and millerite (sample D). A minor fraction ( $< 30\%$ ) of small interstitial BMS consists of pentlandite. In sample D, small interstitial grains of djerfisherite are also abundant.

Small interstitial BMS are ubiquitous in every sample and they are especially abundant in sample C and D (Table 2-1). Beside the small interstitial grains, inclusions are the most abundant type of BMS grains in every sample (Table 2-1). Most of the BMS blebs included in silicates show alteration features while isolated inclusions are rare ( $\sim 10\%$  of the total inclusions). Large interstitial BMS grains are only observed in sample C ( $n = 3$ ) and D ( $n = 1$ ).

In an extensively serpentinized area of sample A, heazlewoodite is observed to replace a BMS grain, which was mostly made of pentlandite (Figure 2-6C). Due to the large alteration observed in this portion of the thin section, it is not possible to classify the BMS grain as interstitial or inclusion. Sub-micron PGM are observed on the boundary between the two phases. Their size is too small to be individually analyzed with the microprobe. However, spot analyzes centered on the PGM show Ru, Ir, Pt concentrations up to 9, 3 and 1 wt. %, respectively.

**Table 2-1** BMS grains petrography.

	N	Inclusion	Pseudoinclusion	Large interstitial	Small interstitial
Sample A	10	+ [pn, cp, po]	-	-	+++ [hz]
Sample B	20	(+) [pn, cp, mss]	-	-	+++ [hz]
Sample C	7	++ [pn, cp]	-	(+) [pn]	++++ [hz]
Sample D	10	++ [pn, cp, dj, mss]	(+) [pn, dj]	(+) [pn,dj]	++++ [ml,dj]

N : number of thin section investigated. - : not detected, (+) : between 0.1 and 0.5 grains on average per thin section, + : about one grain on average per thin section, ++ : more than two grains on average per thin section, +++ : abundant, ++++ : extremely abundant. The most abundant phases of each type of BMS grains are reported in square brackets. cp : chalcopyrite, dj : djerfisherite, hz : heazlewoodite, ml : millerite, po : pyrrhotite, pn : pentlandite.

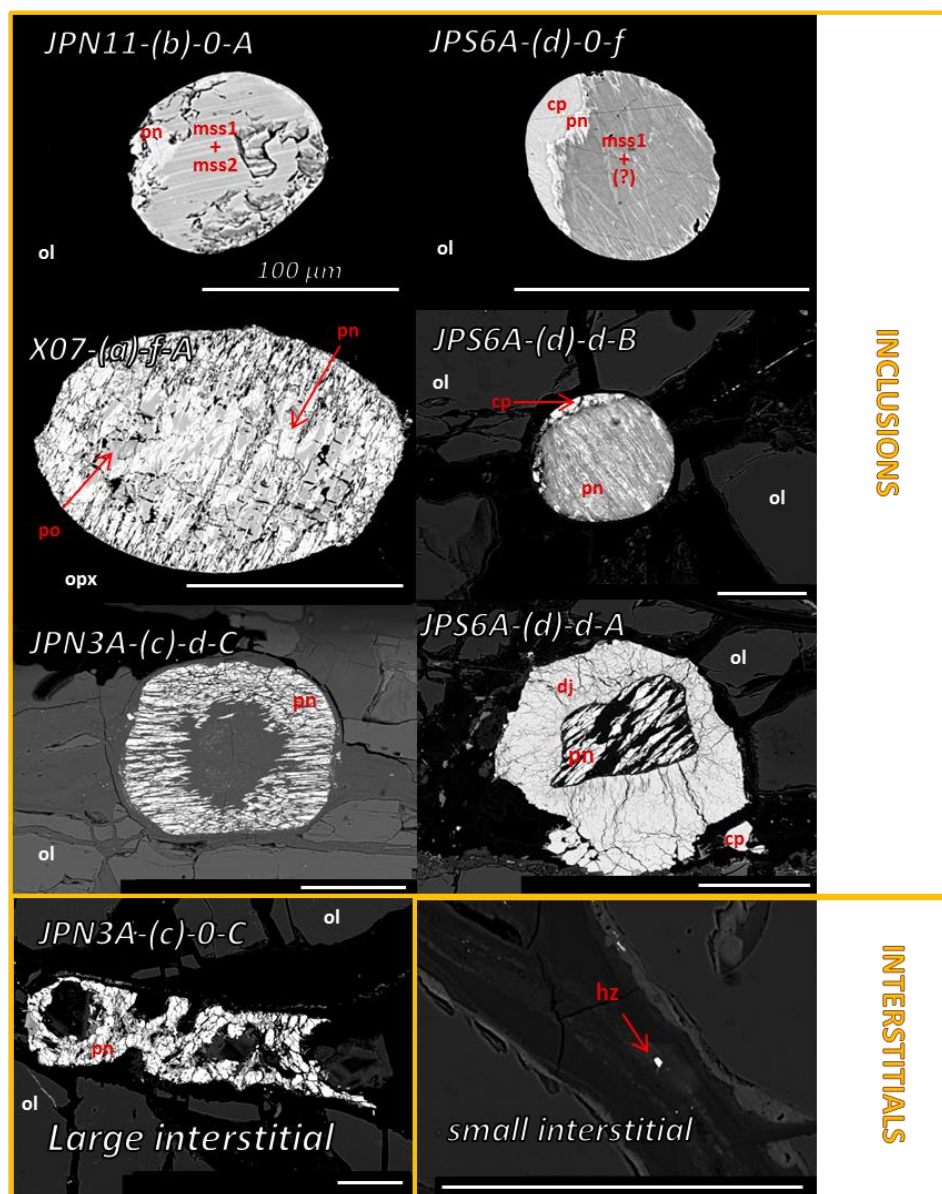


**Figure 2-5** Back scattered electron (BSE) images of BMS grains with different textures and mineralogy. JPN11-(b)-0-A, JPS6A-(d)-0-F and X07-(a)-f-A are well preserved isolated inclusions. JPN11-(b)-0-A consists mostly of fine lamellae of mss1 (i.e. Fe-rich mss, dark lamellae) and mss2 (Ni-rich mss, light lamellae). A patch of pentlandite (pn) is observed on the left rim. The largest areas of JPS6A-(d)-0-F are made of lamellae of mss1 and a Fe-Ni BMS that was not identified due to the small fine-grained texture. A band of pn separates this area from the chalcopyrite (cp) rim. X07-(a)-f-A is made of pyrrhotite (po) and pn. JPS6A-(d)-d-B is an inclusion clearly connected to cracks and it is made of pn and cp (on the top rim). JPN3A-(c)-d-C has an altered core and a rim made of pn, a structure commonly observed in BMS grains in contact with the serpentine matrix. JPS6A-(d)-d-A shows a large corona of djerfisherite (dj) overgrowing on an altered pentlandite core. JPN3A-(c)-0-C is a large interstitial BMS located between two olivine grains. The small interstitial grain is from sample B and consists of heazlewoodite. The white bar is always 100 µm. ol:olivine, opx: orthopyroxene.

### 2.5.2.2 Chemical composition

Pyrrhotite shows  $M/S_{at}$  (i.e. the total metal content over the S content expressed in moles) of 0.89-0.90 and  $Fe/Ni_{at}$  of 95-130. No pure analysis of mss could be obtained due to the fine-grained exsolutions lamellae. Mixed analyses on multiple lamellae yielded  $M/S_{at} = 0.90$  and  $Fe/Ni_{at} = 3-3.5$ , which correspond to Fe-rich mss (i.e. the mss1 field of Craig, 1973). The presence of Ni-rich mss (i.e. the mss2 field of Craig, 1973) is suggested by one mixed measurement that yielded  $M/S_{at} = 0.91$  and  $Fe/Ni_{at} = 1.6$  (light grey lamellae of JPN11-(b)-0-A in Figure 2-5).

Pentlandite displays variable  $Fe/Ni_{at}$ , ranging between 0.6 and 1.5. The  $Fe/Ni_{at}$  does not show a systematic variation with the habit or the texture of BMS grains. Small domains located on the rims of grains in contact with the serpentine-rich veins can be enriched in Ni (up to 50 wt.%) and Co (up to 17 wt.%, i.e. cobalt-pentlandite). Small round blebs or rods (usually  $< 1 \mu m$ ) of pentlandite inside djerfisherite grains are typically enriched in Co ( $> 1$  wt.%) and Ni ( $> 30$  wt.%). Microprobe analyses on three included BMS show Cu content up to 77 wt.%, revealing the presence of Cu-sulfides, most likely in the form of digenite or chalcocite.

Djerfisherite  $(K,Na)_6(Fe,Cu,Ni)_{25}S_{26}Cl$  is only observed in sample D. It occurs in the serpentine-rich matrix or around other sulfide grains. In sample D, about 50% of inclusions and large interstitials are surrounded by a corona of djerfisherite whose thickness varies between 10 and 100  $\mu m$  (Figure 2-5). Compositionally, djerfisherite shows an almost constant Fe content (35-40 wt.%) but a variable Cu and Ni content ( $Cu/Fe_{at} = 0.27-0.49$ ;  $Ni/Fe_{at} = 0-0.22$ ).

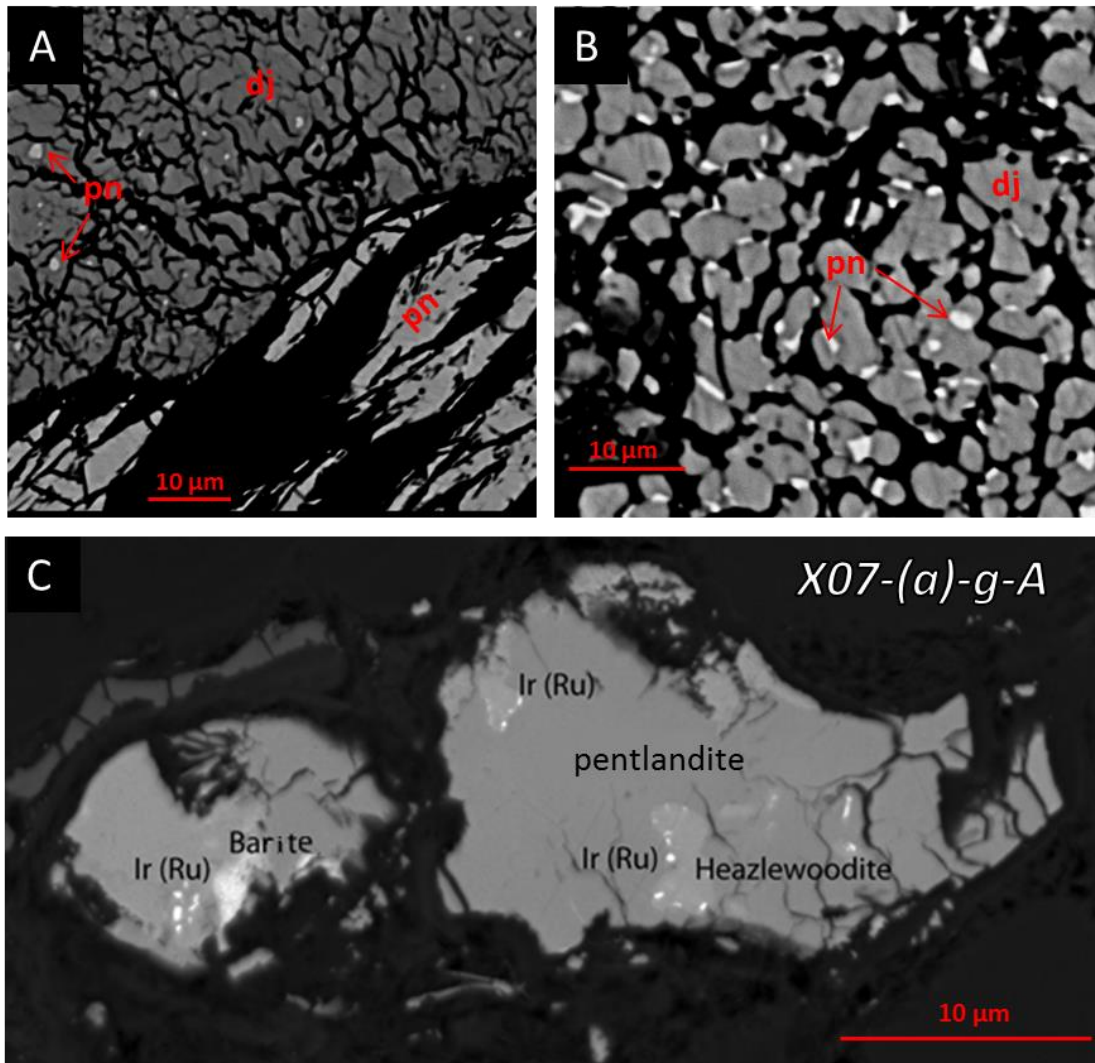


**Figure 2-6** A) BSE image of JPS6A-(d)-d-A showing the djerfisherite corona around the core of pentlandite. Some portions of pentlandite are also observed within the corona (light grey). B) detail of JPS6A-(d)-d-E where pentlandite (light grey) forms rods and patches inside djerfisherite C) BSE image of a pentlandite grain (dark grey) partially replaced by heazlewoodite (light grey). The grain is located in a vein and submicron sized PGM (white spots) are located on the boundary between the two phases. The high resolution BSE image was taken by J-P. Lorand, using a field emission gun electron microscope (FEG-SEM) at the University of Nantes.

### 2.5.3 $^{187}\text{Os}/^{188}\text{Os}$ of single grain BMS

The BMS grains show a large range of  $^{187}\text{Os}/^{188}\text{Os}$  (Table 2-2, Figure 2-7), from very radiogenic (0.1724) to un-radiogenic (0.1084). The four BMS grains with Os isotopic composition higher or equal to the present-day primitive mantle value (i.e.  $^{187}\text{Os}/^{188}\text{Os} \geq 0.1296$ , Meisel et al. 2001), are observed in samples C and D (Figure 2-7). However, the majority of BMS grains from these two samples show un-radiogenic  $^{187}\text{Os}/^{188}\text{Os}$ ,

overlapping with the range observed in samples A and B (i.e. between 0.1084 and 0.1160). The lowest  $^{187}\text{Os}/^{188}\text{Os}$  (0.1084, Figure 2-7) was observed in one BMS grain from sample C. Similarly unradiogenic Os was also measured in BMS grains from samples A ( $^{187}\text{Os}/^{188}\text{Os} = 0.1094$ , Figure 2-7) and D ( $^{187}\text{Os}/^{188}\text{Os} = 0.1088$ , Figure 2-7). Differently, the lowest  $^{187}\text{Os}/^{188}\text{Os}$  from BMS grains of sample B is less unradiogenic ( $^{187}\text{Os}/^{188}\text{Os} = 0.1133$ , Figure 2-7).

With the possible exception of BMS grains that were not characterized for textural relationships, only grains included in silicates were analyzed for  $^{187}\text{Os}/^{188}\text{Os}$ . Overall, there is no systematic variation in  $^{187}\text{Os}/^{188}\text{Os}$  between isolated inclusions ( $n = 2$ ) and inclusions in contact with the vein network ( $n = 11$ ). The most radiogenic isotopic composition was obtained from one BMS grain included in olivine with a large djerfisherite corona (JPS6a-(d)-d-A, see Figure 2-5). All the other inclusions extracted from orthopyroxene and olivine show  $^{187}\text{Os}/^{188}\text{Os} \leq 0.1160$ . Orthopyroxene- and olivine-hosted BMS show no systematic difference in  $^{187}\text{Os}/^{188}\text{Os}$ . The only inclusion hosted in garnet (from sample D) and measured for  $^{187}\text{Os}/^{188}\text{Os}$ , yielded  $^{187}\text{Os}/^{188}\text{Os} = 0.1345$ . With the exception of the djerfisherite-rich grain, no clear correlation between mineral assemblage and  $^{187}\text{Os}/^{188}\text{Os}$  could be observed.

Rhenium and Os concentrations for each sample were not measured, which precluded the possibility of calculating any model age corrected for  $^{187}\text{Os}$  ingrowth (i.e.  $T_{\text{MA}}$  and  $T_{\text{RD}}$  eruption). The  $T_{\text{RD}}$  model ages (Table 2-2) were calculated using the present-day primitive mantle estimates of  $^{187}\text{Os}/^{188}\text{Os} = 0.1296$  and  $^{187}\text{Re}/^{188}\text{Os} = 0.4353$  (Meisel et al., 2001) and the  $^{187}\text{Re}$  decay constant of  $1.666 \cdot 10^{-11} \text{ year}^{-1}$  (Smoliar et al., 1996). The uncertainties on single measurements were propagated to the calculated  $T_{\text{RD}}$  ages. Except for four grains with  $^{187}\text{Os}/^{188}\text{Os} \geq 0.12$ , BMS grains yielded  $T_{\text{RD}}$  ages from Paleoproterozoic to Mesoarchean ( $1.85 \text{ Ga} < T_{\text{RD}} < 2.86 \text{ Ga}$ ). These BMS grains are clustered around three groups of  $T_{\text{RD}}$  ages: seven grains have  $2.86 \leq T_{\text{RD}} \leq 2.63 \text{ Ga}$ ; four grains have  $2.13 \leq T_{\text{RD}} \leq 2.23 \text{ Ga}$ ; four grains have  $1.86 \leq T_{\text{RD}} \leq 1.94 \text{ Ga}$ . The only exception is one BMS grain ( $T_{\text{RD}} = 2.35 \text{ Ga}$ ), which is affected by large analytical uncertainty ( $2\text{SD} = 0.09 \text{ Ga}$ ).

**Table 2-2**  $^{187}\text{Os}/^{188}\text{Os}$  measurements and calculated  $T_{\text{RD}}$  for single BMS grains.

	sample	mineral assemblage	host-phase	type	$^{187}\text{Os}/^{188}\text{Os}$	$\pm$	$T_{\text{RD}}$ (Ma)	$\pm$	
<i>Hand-picked</i>									
	JPN3A-(c)-x-01	C	-		0.10998	0.00013	2647	17	
	JPN3A-(c)-x-02	C	-		0.11595	0.00022	1854	30	
	JPN3A-(c)-x-5	C	-		0.12962	0.00043			
	JPN3A-(c)-x-08	C	-		0.10838	0.00031	2857	42	
<i>Micro-sampled (microdrill)</i>									
	X07-(a)-c-A	A	n.d.	n.d.	0.10937	0.00034	2727	46	
	JPN11-(b)-c-A	B	n.d.	orthopyroxene	<i>f-in</i>	0.11530	0.00013	1940	18
	JPN3A-(c)-a-D	C	n.d.	n.d.	0.17079	0.00080			
	JPN3A-(c)-a-G	C	n.d.	n.d.	0.11359	0.00011	2168	16	
	JPS6A-(d)-d-C	D	pn-cp	garnet	<i>f-in</i>	0.13445	0.00044		
<i>Micro-sampled (laser)</i>									
	X07-(a)-a-D	A	pn	olivine	<i>f-in</i>	0.11385	0.00054	2134	73
	X07-(a)-bII-A	A	*ch/dig-hz?	olivine	<i>f-in</i>	0.10935	0.00011	2729	14
	X07-(a)-f-A	A	pn-po	orthopyroxene	<i>i-in</i>	0.11013	0.00014	2627	20
	JPN11-(b)-aII-A	B	*pn-hz?-ch/dig?	orthopyroxene	<i>f-in</i>	0.11533	0.00025	1936	34
	JPN11-(b)-0-A	B	pn-mss	olivine	<i>i-in</i>	0.11329	0.00027	2208	38
	JPN3A-(c)-f-B	C	pn	olivine	<i>f-in</i>	0.11219	0.00063	2353	86
	JPN3A-(c)-h-A	C	pn	olivine	<i>f-in</i>	0.10868	0.00010	2817	14
	JPS6A-(d)-b-C	D	(dj)-pn	olivine	<i>f-in</i>	0.10883	0.00038	2798	51
	JPS6a-(d)-d-A	D	dj-pn	olivine	<i>f-in</i>	0.17242	0.00099		
	JPS6a-(d)-d-B	D	pn-cp	olivine	<i>f-in</i>	0.11315	0.00009	2226	12
	JPS6a-(d)-e-A	D	pn-cp	olivine	<i>f-in</i>	0.11582	0.00041	1871	56

$T_{\text{RD}}$  model ages were calculated using the present-day primitive mantle values of  $^{187}\text{Os}/^{188}\text{Os} = 0.1296$  and  $^{187}\text{Re}/^{188}\text{Os} = 0.4353$  (Meisel et al., 2001). pn : pentlandite; cp: chalcopyrite; dj: djerfisherite; po: pyrrhotite; hz: heazlewoodite; ch: chalcocite; dig: digenite; *i-in*: isolated inclusion; *f-in*: inclusion in contact with the vein network (fractured inclusion); (dj): djerfisherite corona removed before Os analysis; \*: only tip of the grain exposed. n.d: not determined. Uncertainties are reported as 2SD.

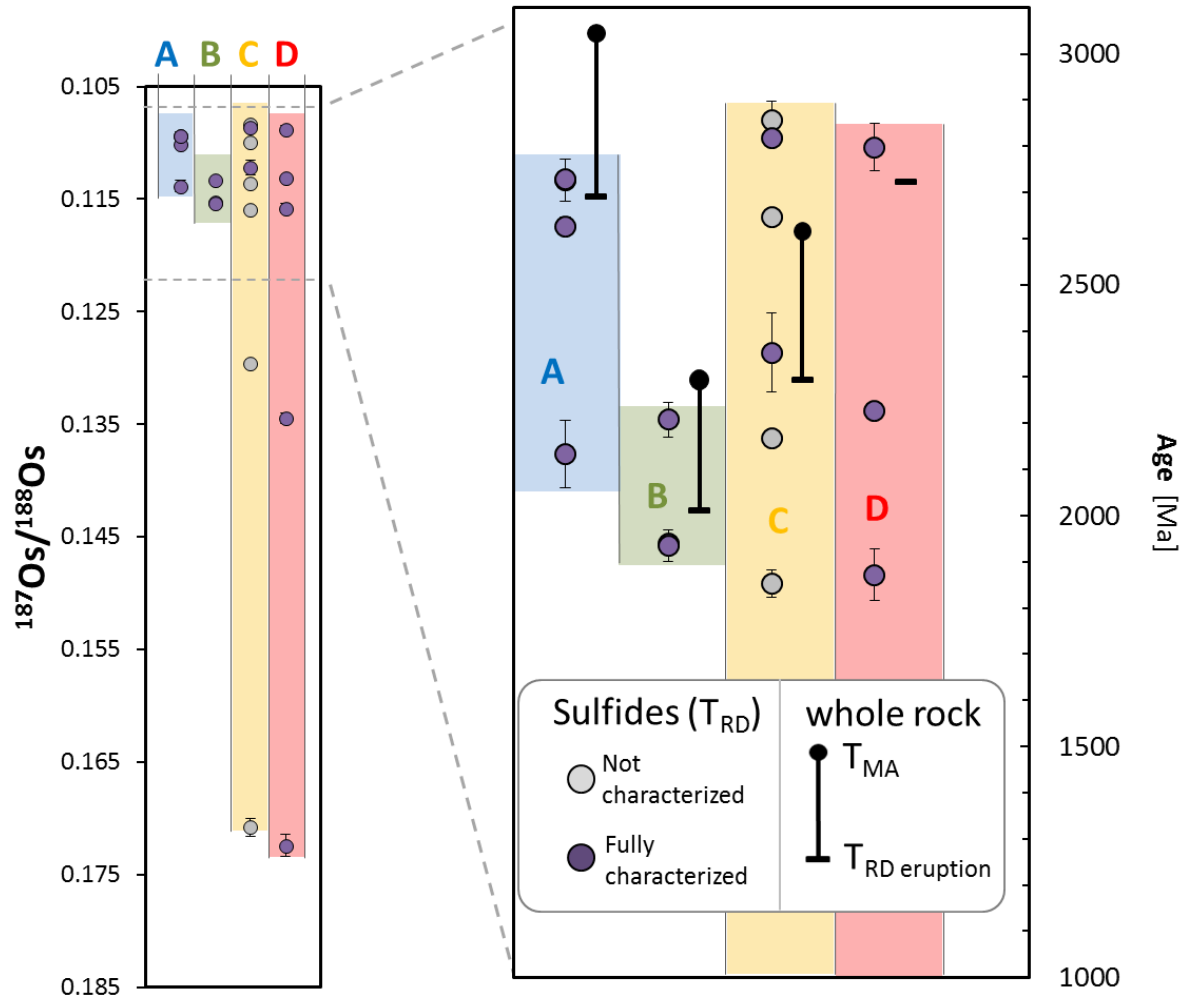


**Figure 2-7** Osmium isotopic composition and Re-Os ages in single BMS grains and whole rocks. On the left, the Os isotopic composition measured in BMS grains and subdivided for xenolith parental group. Purple circles are BMS grains fully characterized for textures and major elements composition (microprobe analyses); grey circles are BMS collected from a coarse crush or not characterized for their mineral assemblage. On the right side, inset from the left diagram with Os isotopic composition converted to  $T_{RD}$  ages. Whole rock  $T_{RD}$  eruption ages and  $T_{MA}$  ages are also reported for comparison. Sample D has Re/Os higher than the present-day primitive mantle, resulting in unrealistic  $T_{MA}$  age.

## 2.6 DISCUSSION

### 2.6.1 Origin of base metal sulfides, PGM and silicates

#### 2.6.1.1 Magmatic BMS

The mantle xenoliths studied here, contain different BMS grains that can be distinguished by size, mineral assemblage, and textural relations with silicates. The polysulfide assemblages of the five isolated inclusions is made of pentlandite+chalcopyrite+mss and pentlandite+pyrrhotite and they suggests a magmatic origin as observed in peridotites (e.g. Alard et al., 2002; Lorand and Grégoire, 2006; Luguët et al., 2004; Shindo et al., 2009) and in basalts (Czamanske and Moore, 1977; Francis, 1990; Mathez, 1976; Patten et al., 2013, 2012; Peach et al., 1990) from other localities. Inclusions connected with the serpentinite veins formed likely in similar magmatic conditions, with the original portions of metal rich sulfides (e.g. mss and pyrrhotite) being replaced by magnetite and silicates during later low temperature processes (Abrajano and Pasteris, 1989; Lorand, 1985; Lorand and Grégoire, 2006; Luguët et al., 2004; see section 2.6.1.3). A high temperature origin of inclusions connected with the serpentinite veins is also testified by the habit of the preserved sulfide portions that resembles that of exsolution lamellae (Figure 2-5).

In mantle rocks, BMS can be either residual phases left behind after partial melting or they can be metasomatic phases that formed during melt or fluid percolation (e.g. Alard et al., 2002, 2000; Harvey et al., 2010; Lorand et al., 2003; Luguët et al., 2004, 2003). Partial melting generally leads to a decrease of the abundance of BMS in a mantle rock. This is related to the high solubility of S in silicate melts, which is a direct function of pressure and to a smaller extent of temperature (Mavrogenes and O'Neill, 1999). The melting pressure can be constrained from whole rock major element concentrations using the model proposed by Herzberg and O'Hara (2002) and Herzberg (2004). A rough estimation of the melting parameters is obtained by plotting the four analyzed samples in a MgO-FeO diagram (Figure 2-8). According to this model, samples A, B, C and D show starting melting pressures of about 4.5, 4.5, 5 and 3.5 GPa, and final melting pressures of about 2.5, 3, 4 and 2 GPa, respectively. The estimated degree of partial melting for samples A through

D is 0.31, 0.26, 0.24, and 0.25, respectively. The model of Herzberg and O'Hara (2002) and Herzberg (2004) assumes a polybaric melting that begins at the starting pressure and ends at the final pressure. The independent estimates of pressure and the degree of partial melting can be used to calculate the amount of S that is removed from the mantle residue after melt extraction. In order to simplify the calculations, the melting processes can be assumed to occur in two steps. In this simplified scenario, 50% of the total produced melt is extracted at the starting pressure and the remnant 50% is extracted at the final pressure. With the equation of Mavrogenes and O'Neill (1999), it is then possible to calculate the amounts of S that is removed from the source in these two steps. The sum of the two amounts gives an indicative estimate of the total S that can be extracted from the samples during partial melting. The calculated amounts are 310, 270, 240 and 240  $\mu\text{g/g}$  of S, respectively, for samples A, B, C and D. In light of these estimates, and given that a fertile lherzolite is assumed to contain  $250 \pm 50 \mu\text{g/g}$  of S (McDonough and Sun, 1995), the four samples are expected to be extremely depleted in S.

If one takes the average S content and the modal abundance of BMS grains, it is possible to estimate their contribution on the whole rock S budget. In the case of samples A and B, included BMS grains are rare (less than one grain per thin section). For these two samples, a maximum whole rock S content of 10  $\mu\text{g/g}$  can be estimated assuming one BMS grain with a diameter of 150  $\mu\text{m}$  per thin section. Thus, considering the large uncertainty of the melting model (e.g. on the estimates of the melting pressures and the S content of the primitive mantle), it cannot be excluded that these BMS may be residues of partial melting. However, most likely S was completely extracted by the silicate melt. In this case PGM are expected to crystallize in the form of Ru-Os-Ir sulfides/alloys and Pt-Ir alloys (e.g. Fonseca et al., 2011; Luguet et al., 2007; Mungall and Brenan, 2014). The lack of such PGM in Somerset Island xenoliths could be explained by later re-introduction of BMS and subsequent redissolution of PGM (Delpéch et al., 2012; Griffin et al., 2004, 2002; Lorand et al., 2010, 2008b) due to the high solubility of HSE in sulfide phases (e.g. Mungall and Brenan, 2014 and references therein). In this scenario, the required amount of metasomatic sulfides is extremely limited as they account for less than 10  $\mu\text{g/g}$  of S on the bulk rock. In samples C and D, large BMS grains are more abundant than in samples A and B. They can be relatively large in size (up to 500  $\mu\text{m}$ ) and the extreme variation in size makes a proper

quantification of the BMS modal abundance difficult. Nevertheless, a reasonable minimum estimate can be obtained when four grains with a diameter of 250  $\mu\text{m}$  per thin section are assumed. This leads to about 100  $\mu\text{g/g}$  of S on the whole rock. This amount is too high to be inherited from the original melting process and later metasomatism is necessary to reintroduce BMS in these two xenoliths. Sulfide-bearing metasomatism in sample C and D is also suggested by the occurrence of large interstitial BMS, which are typically, but not solely, formed during the percolation of melts through the mantle (e.g. Alard et al., 2000). A metasomatic origin of large interstitial BMS grains is additionally supported by their size that is larger than included BMS grains. In fact, during partial melting, interstitial BMS are expected to be more consumed than included BMS (Harvey et al., 2011). Interestingly, the two samples with petrographic indications of metasomatic BMS show the most overprinted a whole rock HSE signature, characterized by supra-chondritic Pd/Pt.

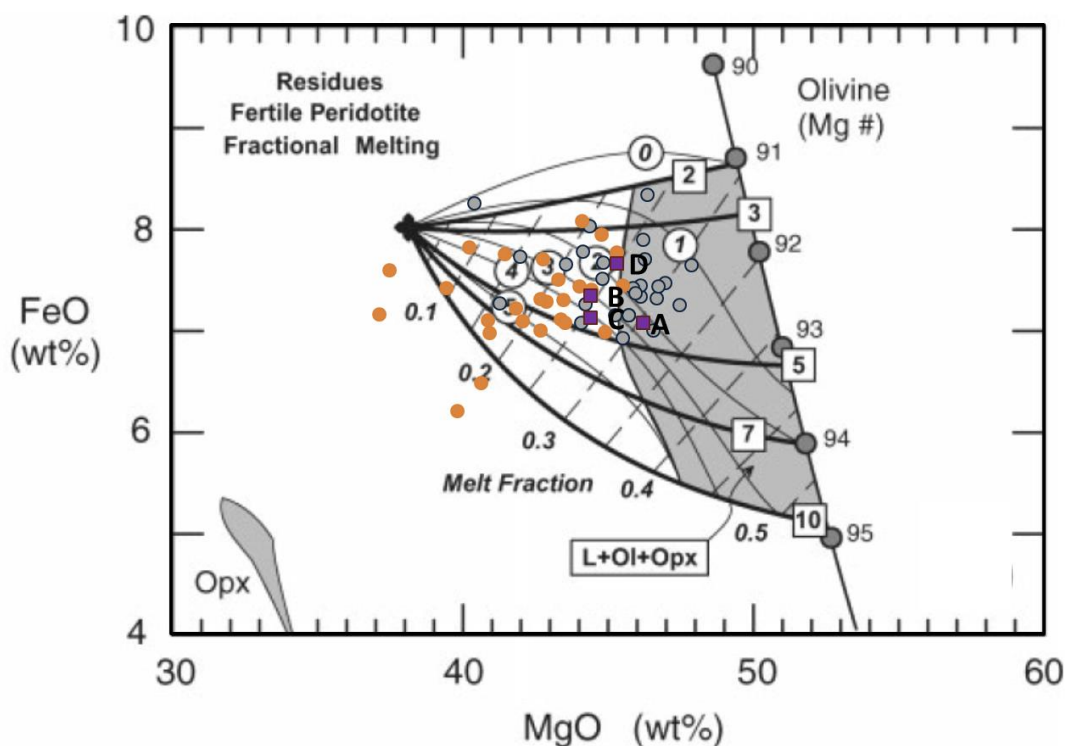


**Figure 2-8** Somerset Island xenoliths plotted in the MgO vs FeO diagram of Herzberg (2004). Purple symbols are the whole rock compositions of the studied samples. Grey symbols are xenoliths from Irvine et al. (2003), and orange symbols are xenoliths from Schmidberger and Francis (1999). Bold lines labelled with squares are initial melting pressures (GPa); light lines labelled with circles are final melting pressures (GPa); light dashed lines are melt fractions.

### 2.6.1.2 Kimberlite infiltration

Processes able to introduce metasomatic sulfides in mantle xenoliths include interactions with the kimberlite host magma (e.g. Grégoire et al., 2002; Griffin et al., 2004) and fluid/melts reactions that can also occur shortly before the kimberlite magmatism (e.g. Giuliani et al., 2013). The presence of djerfisherite in sample D testifies a strong BMS metasomatism associated with the kimberlite magmatism (Misra et al., 2003; Sharygin et al., 2012, 2007). In fact, djerfisherite typically occurs in alkali-rich fluids and is found in kimberlites from many localities (e.g. Chakhmouradian and Mitchell, 2001; Clarke, 1979; Sharygin et al., 2007), including Somerset Island (Clarke et al., 1994). Often djerfisherite contains small domains of pentlandite, which could represent the residue of older BMS (Figure 2-6A). However, the arrangement and shape of some blebs and rods (Figure 2-6B) resemble the texture observed in sphalerite affected by the “chalcopyrite disease” (e.g. Barton Jr. and Bethke, 1987). This texture is thought to result from re-equilibration of the original homogenous assemblage after changes of the chemical and/or physical conditions (Bente and Doering, 1995). This suggests an early formation of djerfisherite, probably at relative high temperature as confirmed by the high thermal stability of this mineral (> 600 °C, Clarke 1979).

In sample D, djerfisherite is also observed inside the clinopyroxene rims that surround altered orthopyroxene crystals (Figure 2-9). This suggests that the crystallization of clinopyroxene at the expense of orthopyroxene is coeval with djerfisherite, and thus most likely related to the kimberlite magmatism. The late crystallization of clinopyroxene during kimberlite magmatism was also observed in other localities (e.g. Boyd and Mertzman, 1987; Dawson, 2002; Kopylova and Caro, 2004; Simon et al., 2007, 2003) and might indicate an important and widespread metasomatic process in kimberlite-hosted xenoliths.

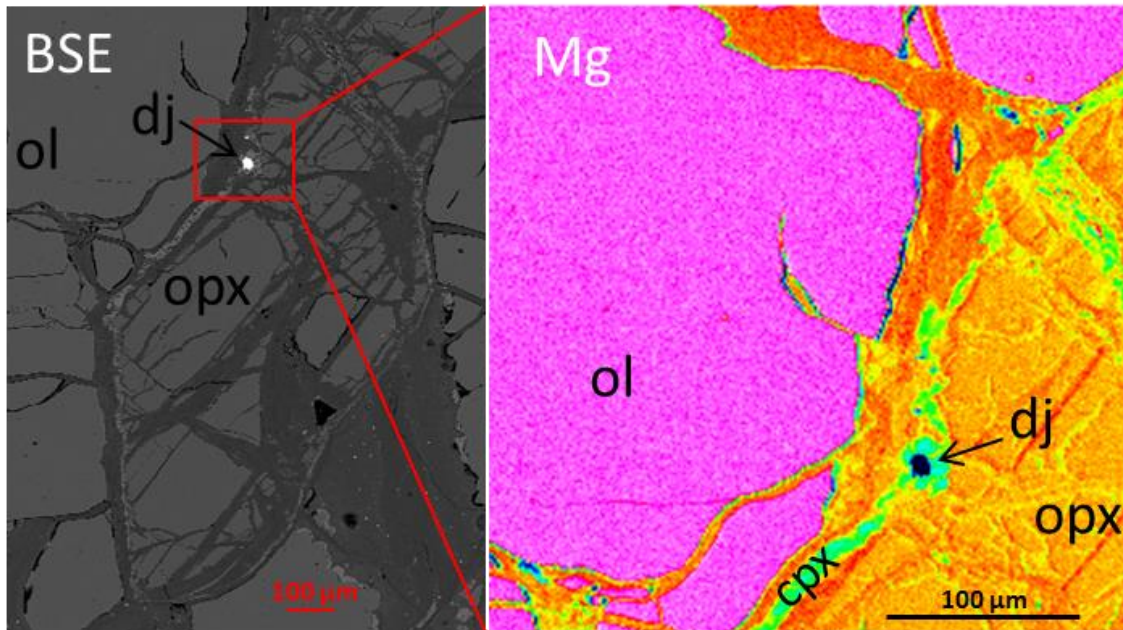


**Figure 2-9** BSE image (left) and WDS magnesium map (right) of a partially dissolved orthopyroxene grain surrounded by a clinopyroxene rim containing djerfisherite. cpx: clinopyroxene, ol: olivine, opx: orthopyroxene, dj: djerfisherite.

### 2.6.1.3 Serpentinization and low temperature PGM

Inclusions that appear to be connected with the serpentine veins are made of pentlandite and chalcopyrite and are characterized by portions filled with silicates and magnetite. This type of alteration of Fe-Ni BMS is consistent with serpentinization processes (Abrajano and Pasteris, 1989; Lorand, 1985; Lorand and Grégoire, 2006; Luguet et al., 2004).

Serpentine-rich veins are characterized by the ubiquitous presence of small grains of heazlewoodite (samples A, B and C) or millerite (sample D). These two sulfides are characteristic for serpentinization processes due to desulfurization of sulfides such as pyrrhotite or pentlandite (Abrajano and Pasteris, 1989; Alt and Shanks, 1998; Klein and Bach, 2009; Lorand, 1985; Lorand and Grégoire, 2006; Luguet et al., 2004; Shiga, 1987). A snapshot of this process is observed in some pentlandite grains that are partially replaced by heazlewoodite (Figure 2-6C). Interestingly, Ru-Ir-Pt-rich PGM were observed along the boundary between the two phases. Pentlandite is known to be able to accommodate high amounts of HSE (up to wt.%, Makovicky et al., 1986), thus the exsolution of discrete PGM phases was likely triggered by the formation of heazlewoodite at the expenses of

pentlandite. The PGM grains are observed on the boundary but not inside heazlewoodite, suggesting that they migrate along the interface between the two minerals and that they might grow and coalesce to form  $\mu\text{m}$ -sized grains. In the case of Somerset Island, PGM are clearly secondary and related to a desulfurization process. Desulfurization has been proposed to lead to the formation of PGM starting at relatively high  $f(\text{S}_2)$  during the breakdown of mss (e.g. Pt-Ir alloys as shown by the experiments of Peregoedova et al., 2004) or at extremely low  $f(\text{S}_2)$  during the exhaustion of BMS to form Fe-Ni alloys (Foustoukos et al., 2015). However, the PGM observed here formed during intermediate  $f(\text{S}_2)$  conditions when pentlandite is consumed and heazlewoodite is still stable.

In sample D, the small Ni-rich interstitial sulfide grains mainly consist of millerite while heazlewoodite is absent. During serpentinization, it is suggested that millerite forms whenever fluids have higher  $f(\text{H}_2\text{S})$  or lower  $f(\text{H}_2)$ , in opposition to heazlewoodite (Klein and Bach, 2009). Such conditions are obtained if the fluid to rock ratio increases in association with a more extensive serpentinization process (Klein and Bach, 2009). Thus, small interstitial BMS from sample D record different conditions when compared to those of the other three samples. A possible reason for this might be a more extensive serpentinization process in sample D.

## ***2.6.2 Mantle processes and Re-Os model ages***

### ***2.6.2.1 Probability density plots of Os model ages***

The ages of melting events are often determined from peaks on probability density plots of Os model ages from mineral phases (e.g. BMS grains and PGM) or whole rocks (Griffin et al., 2002; Heaman and Pearson, 2010; Pearson et al., 2007; Rudnick and Walker, 2009). When the  $T_{\text{RD}}$  ages obtained from single BMS grains of Somerset Island are plotted in such a diagram, they display three well defined peaks (Figure 2-10). In contrast, density probability plots of model ages ( $T_{\text{RD}}$  eruption ages and  $T_{\text{RD}}$  ages) from whole rock data show only two peaks (Irvine et al., 2003). On a closer look, the  $\sim 2.2$  and  $\sim 1.9$  Ga peaks observed in single BMS grains overlap with a wide peak at  $\sim 2.1$  Ga on the whole rocks scale (Figure 2-10). The 2.7-2.8 Ga age is not visible in whole rock  $T_{\text{RD}}$  ages and is

recorded by  $T_{RD}$  eruption ages only in a limited subset of samples (Figure 2-10). Thus, the information obtained from BMS grains is only partially visible on the whole rock scale. This demonstrates that single BMS grain investigations provide a better resolution to identify the presence of mantle portions with distinct  $T_{RD}$  age signatures (i.e.  $^{187}\text{Os}/^{188}\text{Os}$ ).

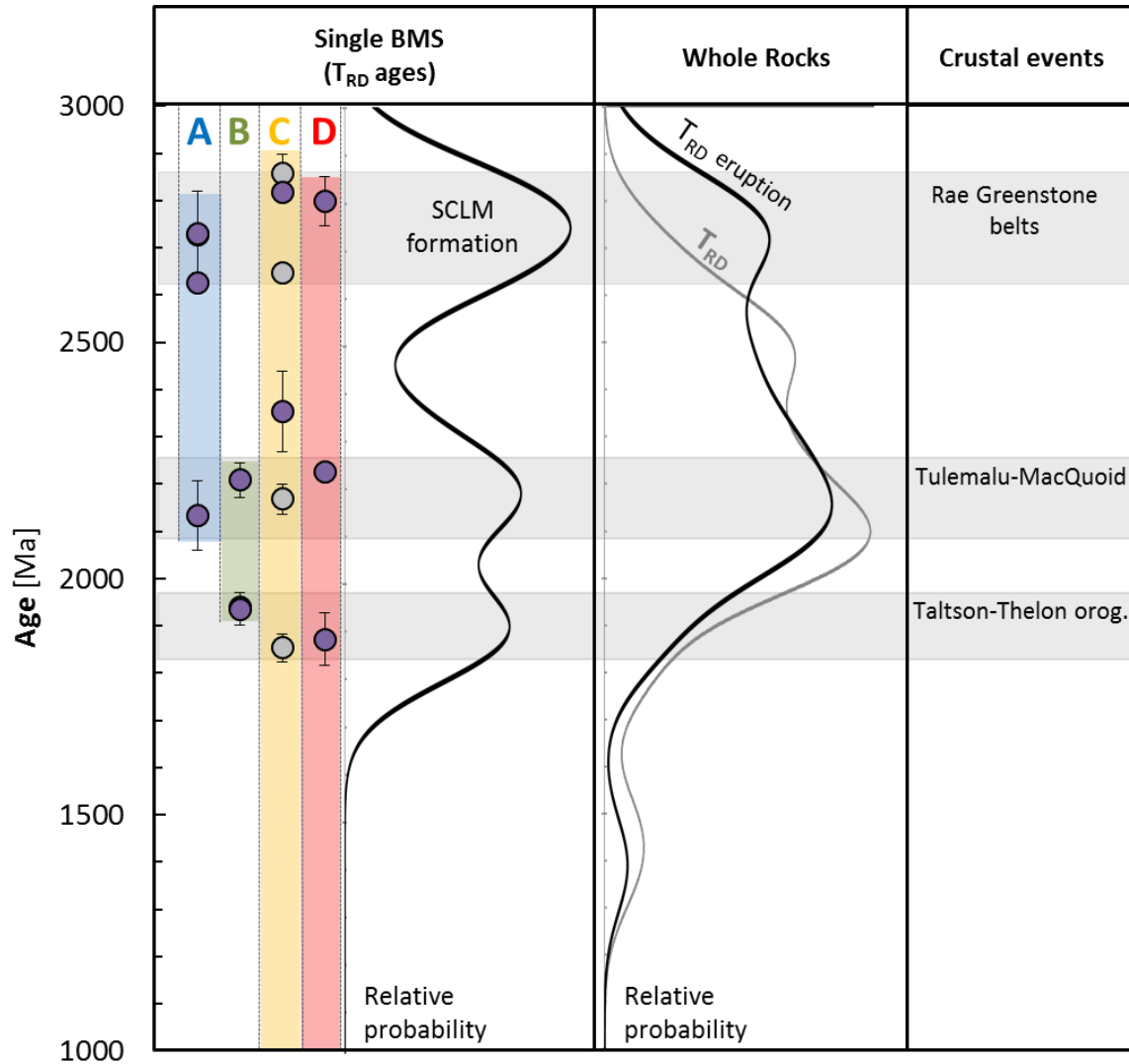


**Figure 2-10** Compilation of Re-Os model ages from Somerset Island. From left to right:  $T_{RD}$  ages from single grain BMS as reported in Figure 2-7; probability density plot of  $T_{RD}$  ages for single grain BMS; probability density plot of  $T_{RD}$  and  $T_{RD}$  eruption ages for 33 whole rocks from Somerset Island (Irvine et al., 2003); crustal events recorded in the Rae craton that overlap in age with Re-Os model ages. Data in probability density plots are reported assuming an uncertainty of 200 Ma (cf. Pearson et al., 2007).

### 2.6.2.2 *Re-Os model ages from whole rocks and BMS: an integrated view*

Sample A has a residual HSE signature. Although less affected by post-melting events, rocks with residual HSE signature are not completely immune to sulfide metasomatism (cf. Griffin et al., 2004; Harvey et al., 2011), which can result in the introduction of BMS with variable Re/Os and  $^{187}\text{Os}/^{188}\text{Os}$  (e.g. Alard et al., 2002). In sample A,  $T_{\text{RD}}$  ages obtained from the whole rock (2.69 Ga) and from three of the four analysed BMS grains (2.63-2.73 Ga) are in very good agreement (Figure 2-7). This suggests that the whole rock Os budget is controlled by one population of BMS grains with relatively homogeneous  $^{187}\text{Os}/^{188}\text{Os}$  and that the contribution of metasomatic Os is negligible. For this reason it is likely that the  $T_{\text{RD}}$  ages observed in three BMS grains and in the whole rock record the first melting event of sample A, which occurred at  $\sim 2.7$  Ga.

Sample B is the only sample that does not show any Re-Os model age in the 2.7-2.8 Ga range (Figure 2-7). This sample has a clear depleted PGE signature. However, the recovery of a BMS grain with  $T_{\text{RD}}$  age significantly older than the whole rock  $T_{\text{RD}}$  age (Figure 2-7) implies that the whole rock Os budget is not controlled by the BMS population with the most unradiogenic Os. This suggests that the sample experienced significant Os metasomatism. A minimum depletion age of 2.2 Ga can be estimated for sample B but it is worth to stress that this age is constrained by only one BMS grain and that only three BMS grains were successfully measured for  $^{187}\text{Os}/^{188}\text{Os}$ .

When compared to sample A and B, sample C and D show more petrographic evidence of BMS metasomatism and they are characterized by a more overprinted whole rock HSE signature (i.e. supra-chondritic Pd/Pt). The Os isotopic composition is also clearly affected by metasomatism as highlighted by the four BMS grains with radiogenic Os, which yielded  $^{187}\text{Os}/^{188}\text{Os}$  higher than the present-day primitive mantle (Figure 2-7).

Sample C shows a relatively narrow range in whole rock Re-Os model ages ( $T_{\text{MA}}-T_{\text{RD}} = 0.3$  Ga, Figure 2-7) and  $T_{\text{RD}}$  ages from BMS grains spread well outside this range, indicating that sample C underwent a complex history that strongly affected the Re-Os isotopic systematic. Due to metasomatic processes, the whole rock Re-Os model ages do not provide meaningful age information.

The oldest  $T_{RD}$  age from BMS grains (2.80 Ga) of sample D is older than the whole rock  $T_{RD}$  age (2.1 Ga, Appendix A) but similar to the whole rock  $T_{RD}$  eruption age (i.e. 2.72 Ga, Appendix A, Figure 2-7). This is consistent with a strong enrichment in Re during the kimberlite magmatism, as also testified by the fact that this sample lies on the 94 Ma errorchron. The 2.8 Ga  $T_{RD}$  age was obtained from one BMS grain that was extracted after the removal of the djerfisherite rim by laser ablation (Figure 2-4). In contrast, the most radiogenic Os isotopic composition ( $^{187}\text{Os}/^{188}\text{Os} = 0.1724$ ) was measured from one BMS grain with a preserved large djerfisherite corona. This is in agreement with a crystallization of djerfisherite from the Re-rich kimberlite liquid and it suggests that this process resulted in heterogeneous Os isotopic composition at the micro-scale (i.e. within the same grain).

### ***2.6.3 Age significance and geodynamic interpretation of BMS $T_{RD}$ model ages***

#### ***2.6.3.1 The 2.7-2.8 Ga melting event***

The  $T_{RD}$  ages probability density plot of BMS grains from Somerset Island shows a well-defined peak at 2.7-2.8 Ga. This age is recorded in BMS grains from three of the four analyzed samples and similar ages were also reported by Re-Os and Lu-Hf studies on xenoliths from Somerset Island (Irvine et al., 2003; Schmidberger et al., 2002). Based on this, there is large evidence that the major SCLM-forming process occurred in the Neoproterozoic. This event overlaps in age with the formation of the Rae greenstone belts, including the Woodburn Lake (2.74-2.63 Ga), Prince Albert (2.73-2.69 Ga) and Mary River (2.85-2.69 Ga) groups (Hartlaub et al., 2004; Ryan et al., 2009; Young et al., 2007). In particular, Somerset Island is located near the Prince Albert group, which outcrops in the mainland of Nunavut (~500 km south of Somerset Island, Figure 2-1), and the Mary River group, which is located in Baffin Island (~500 km east of Somerset Island, Figure 2-1). Thus, the 2.7-2.8 Ga age recovered in mantle xenoliths from Somerset Island might be related to the formation of the nearby Prince Albert and Mary River greenstone belts (Irvine et al., 2003). It has been proposed that the Rae greenstone belts derived from mantle melting in a continental rift setting as suggested by stratigraphic investigations, which reported a sialic basement overlain by continental-like sediments and mafic and ultramafic volcanic rocks (Hartlaub et al., 2004; Nadeau et al., 2008; Skulski et al., 2003; Zaleski et

al., 2001, 2000). Following these considerations the SCLM beneath Somerset Island formed during continental rifting.

A similar scenario was also proposed for the Slave craton. The main formation of the Slave SCLM occurred at 2.7-2.8 Ga as testified by a pronounced peak in  $T_{RD}$  ages from mantle xenoliths and BMS grains (e.g. Heaman and Pearson, 2010). Moreover, the Slave greenstone belts (e.g. Yellowknife supergroup) have a similar age (2.7-2.8 Ga) and they likely formed in a continental rift setting (Cousens et al., 2006; Cousens, 2000; Helmstaedt, 2009). Therefore, it seems consistent that the Slave and the Rae cratons share a common Neoproterozoic history (Heaman and Pearson, 2010; Pehrsson et al., 2013). However, in contrast to the Slave craton, so far there is no evidence of pre-Neoproterozoic depletion in the SCLM of the Rae craton.

### 2.6.3.2 Age significance of the ~1.9 Ga and ~2.2 Ga $T_{RD}$ model ages

The ~1.9 Ga and ~2.2 Ga peaks observed in the  $T_{RD}$  ages density probability plot is defined by BMS grains from all four samples (Figure 2-10). The discussion of the origin of these two populations is hampered by the lack of distinctive mineralogical composition and by the fact that their Re content is not known. Nevertheless, there are several possibilities to explain the two Paleoproterozoic peaks in  $T_{RD}$  ages. For example, the three BMS populations with  $T_{RD}$  ages of ~1.9 Ga, ~2.2 Ga and 2.7-2.8 Ga could share the same origin. In this case the different Os isotopic signature could have resulted from a variable interaction with metasomatic agents and/or by *in situ* Re decay.

The first possibility requires partial metasomatic overprinting of  $^{187}\text{Os}/^{188}\text{Os}$ . This scenario is supported by the relatively fast diffusion of Os in pyrrhotite at magmatic temperature (the diffusion coefficient is  $\sim 10^{-14}$  m<sup>2</sup>/s at 950 °C, Brenan et al., 2000). However, after a partial re-equilibration with metasomatic fluids/melts, the Os isotopic composition is expected to vary largely between different BMS, depending on many variables, such as the original Os content of BMS, the BMS grain size and the exposure to metasomatic agents. Thus a diffusion driven re-equilibration cannot easily justify the clustered  $^{187}\text{Os}/^{188}\text{Os}$  of BMS grains. Moreover, an independent evidence against a significant effect of Os diffusion during metasomatism is provided by the extreme  $^{187}\text{Os}/^{188}\text{Os}$  variation between djerfisherite coronae and the older pentlanditic cores.

Furthermore, for the same reasons discussed for metasomatic Os, metasomatic Re can unlikely explain the clustered  $^{187}\text{Os}/^{188}\text{Os}$ .

Alternatively, the three BMS populations with  $T_{\text{RD}}$  ages of ~1.9 Ga, ~2.2 Ga and 2.7-2.8 Ga can be co-genetic if they formed with variable Re/Os. Assuming a  $^{187}\text{Re}/^{188}\text{Os}$  ratio of zero in the oldest population with 2.7-2.8 Ga  $T_{\text{RD}}$  age, the BMS grains with ~1.9 Ga and ~2.2 Ga  $T_{\text{RD}}$  ages would require  $^{187}\text{Re}/^{188}\text{Os}$  of ~0.15 and ~0.10, respectively. In this scenario, the discrete distribution in  $^{187}\text{Re}/^{188}\text{Os}$  would resemble the variable partitioning of the two elements between different sulfide phases (e.g. Ballhaus et al., 2006; Liu and Brenan, 2015). As a consequence, populations with different  $T_{\text{RD}}$  ages are expected to show peculiar mineral assemblages, with fixed proportion of mineral phases. The lack of correlation between  $T_{\text{RD}}$  ages and sulfide mineral assemblages argues against this scenario. Therefore, most likely, the two BMS populations yielding  $T_{\text{RD}}$  ages of ~1.9 Ga and ~2.2 Ga are not related to the melting event at 2.7-2.8 Ga and their Os signature derives from later metasomatic processes.

Metasomatic BMS can be re-introduced in a residual peridotite by migration of sulfide melts or by sulfide precipitation from melts/fluids (Ackerman et al., 2009; Alard et al., 2011, 2000; Chesley et al., 1999; Delpech et al., 2012; Lorand et al., 2003; Lorand and Alard, 2001; Luguet et al., 2003; Mungall and Su, 2005). Since the ~2.2 Ga and ~1.9 Ga  $T_{\text{RD}}$  ages are recovered from BMS grains that are included in silicates, a recrystallization of the rock is required after sulfide addition. After this event, any textural evidence of the transport mechanism would be likely deleted, making it difficult to infer the nature of the metasomatic agent.

Although the behavior of Os (and Re) during melt/fluid percolation is not well known, it has been suggested that meaningful  $T_{\text{RD}}$  ages can be obtained from metasomatic BMS grains (Griffin et al., 2004). This possibility was proposed on the basis of a correlation between major crustal collision events and  $T_{\text{RD}}$  ages from mantle BMS grains. This implies that metasomatic BMS inherited their Os signature directly from a mantle reservoir with a primitive-like composition that melted in response to changes in the geodynamic setting (Griffin et al., 2004). Following these considerations, the ~1.9 Ga and ~2.2 Ga  $T_{\text{RD}}$  ages recorded in BMS from Somerset Island can be correlated to crustal events.

A Nd model age of an orthogneiss in the Boothia uplift provides hints of magmatism in the area of Somerset Island at ~2.2 Ga (Frisch and Hunt, 1993). On a larger scale, at 2.19 Ga, the east part of the Rae craton (~1200 km south of Somerset Island) was intruded by the Tulemalu-MacQuoid dyke swarm (Hanmer et al., 2006; Tella et al., 1997). Interestingly, almost simultaneous magmatism is observed in the Slave craton with the formation of the 2.23 Ga Malley and 2.21 MacKay dykes (Buchan et al., 2012). Based on paleomagnetic data, Halls (2014) proposed that the 2.2 Ga magmatism in the area occurred during extensive rifting of the Slave from the Rae craton. The rifting process resulted in large-scale melting of the asthenospheric mantle to form oceanic crust between the two cratons (Halls, 2014). Therefore, it is likely that portions of the produced melts percolated in the lithospheric mantle and that metasomatic BMS were introduced into the mantle that was already depleted at 2.7-2.8 Ga.

The Boothia uplift, which is interpreted as an extension of the 1.9–2.0 Ga Taltson–Thelon orogen (Frisch and Hunt, 1993; Hoffman, 1989; Kitsul et al., 2000), is located only 100 km from the JP and Nikos kimberlite pipes (Figure 3-1). Moreover, three of the four xenocryst zircons collected from Battey kimberlite (Somerset Island) yielded U-Pb ages between 1.89 and 1.94 Ga (Parrish and Reichenbach, 1991). This evidence, along with aeromagnetic anomaly maps, suggests that the main crystalline basement of Somerset Island is Paleoproterozoic in age and possibly related to the Thelon orogen (Frisch, 2011; Parrish and Reichenbach, 1991). Due to the intense tectonic activity of the area, it is likely that a portion of the mantle melted during the Thelon orogeny. In particular, the eastward subduction of the Slave craton beneath the Rae craton (Hoffman, 1989), supports the formation of a mantle wedge in the area of Somerset Island. Thus, some of the metasomatic BMS might have formed due to the percolation of the magma produced in an arc-like setting.

In conclusion,  $T_{RD}$  model ages recorded by metasomatic BMS can be interpreted in the context of the complex geodynamic setting that interested the SCLM beneath Somerset Island. If the interpretation is correct, this portion of the mantle experienced metasomatism associated with mantle melting events that resulted from the relative movements of the Rae from the Slave craton. The peculiar position of Somerset Island, on the edge of the Rae

craton, and in proximity of the Thelon orogeny, might justify the geological record of mantle xenoliths from this locality.

According to the proposed geodynamic scenario, the metasomatic BMS inherited their Os isotopic composition from a mantle with a primitive like composition. This requires that the two mantle sources were not enriched or depleted before the melting process at 1.9 and 2.2 Ga. Since the 1.9 Ga melting event was interpreted to have occurred in an arc like setting, this implies that no radiogenic Os was transferred to the mantle wedge from the subducting plate.

## **2.7 CONCLUDING REMARKS**

The two investigated xenoliths with the most overprinted HSE signature (e.g. supra-chondritic Pt/Pd) are distinguished by their high sulfide modal abundance, the occurrence of large interstitial BMS grains and the extreme  $^{187}\text{Os}/^{188}\text{Os}$  variation measured in BMS grains ( $^{187}\text{Os}/^{188}\text{Os} = 0.172\text{-}0.108$ ). The whole rock  $T_{\text{RD}}$  ages (and  $T_{\text{RD}}$  eruption ages) of these samples largely underestimate the real melting age, confirming that caution should be taken in interpreting Re-Os model ages from samples with evidence of metasomatism. Instead, BMS can still preserve the original Os isotopic composition, providing reliable age information.

Petrographic investigations combined with literature HSE data, reveal a strong interaction between many mantle xenoliths from Somerset Island and the kimberlite host magma. This process is visible on the whole rock scale as a strong Re-enrichment, which yielded an errorchron overlapping with the age of the kimberlite (94  $\pm$  24/-20 Ma). On the mineral scale, the interaction with the kimberlite resulted in the formation of djerfisherite and in the crystallization of clinopyroxene at the expense of orthopyroxene. Portions of BMS that survived the interaction with the kimberlite preserved unradiogenic Os ( $^{187}\text{Os}/^{188}\text{Os} = 0.109$ ) while the djerfisherite overgrowth contain highly radiogenic Os ( $^{187}\text{Os}/^{188}\text{Os} = 0.172$ ). This attests the ability of BMS grains (or portions of them) to preserve the original Os isotopic composition even after extensive metasomatism.

Single BMS  $T_{RD}$  ages confirm that the ages recorded in the SCLM beneath Somerset Island are younger ( $\leq 2.8$  Ga) than the oldest ages observed in the nearby Slave (up to  $3.9 \pm 0.3$  Ga, Aulbach et al. 2004), Superior (up to  $\sim 3.7$  Ga, Smit et al. 2014) and North Atlantic cratons (up to  $\sim 3.1$  Ga, Wittig et al. 2010). Three of the four analyzed samples show evidence of a large melting event at 2.7-2.8 Ga, coeval with the widespread formation of greenstone belts in the Rae craton (Irvine et al., 2003). Because a similar Neoproterozoic scenario was proposed for the Slave craton (Heaman and Pearson, 2010), it is consistent that the Slave and the Rae Cratons share the same Neoproterozoic history (Heaman and Pearson, 2010; Pehrsson et al., 2013).

Two more  $T_{RD}$  ages ( $\sim 1.9$  and  $\sim 2.2$  Ga) are clearly recorded by BMS grains from Somerset Island. The two ages are not resolvable on the whole rock scale (Figure 2-10) and they might record a complex tectonic and magmatic history. The  $T_{RD}$  ages of metasomatic BMS grains are consistent with two processes of mantle melting in the Paleoproterozoic. In this scenario, the  $\sim 2.2$  Ga  $T_{RD}$  age testifies the opening of a new ocean between the Slave and Rae craton (Halls, 2014), while the  $\sim 1.9$  Ga can be related to the subduction of such ocean beneath the Rae craton at the beginning of the Thelon orogeny (Hoffman, 1989).

It is shown here that BMS grains underwent a complex geological history, which needs to be better constrained in order to make the best use of the age information carried by the Os isotopic composition. A fundamental progress in this direction might be provided by the combined determinations of  $^{187}\text{Os}/^{188}\text{Os}$  and HSE content from the same individual BMS grain. A method that allows this type of investigation is developed in the next chapter of this thesis.

### *Chapter 3:*

## HSE AND $^{187}\text{Os}/^{188}\text{Os}$ CHARACTERIZATION OF SINGLE SULFIDES VIA MICRO-CHEMISTRY

### **3.1 INTRODUCTION**

Due to the compatible behavior of Os and the relative incompatibility of Re during mantle melting, the  $^{187}\text{Re}$ - $^{187}\text{Os}$  decay system is the chronometer of choice to date the formation of lithospheric roots (Carlson, 2005; Rudnick and Walker, 2009; Shirey and Walker, 1998; Walker et al., 1989). Despite being the most robust geochemical tool for dating mantle rocks, the Re-Os isotopic systematic can still be affected by overprinting processes (e.g. melts/fluids percolation) as usually revealed by modifications of the original whole rock HSE signature (Lorand et al., 2013 and references therein). A whole rock HSE and  $^{187}\text{Os}/^{188}\text{Os}$  investigation, thus provides only average estimations, which are the result of mixed signatures inherited from several geological events, represented by multiple generations of base metal sulfides (BMS) (Alard et al., 2011, 2000; Griffin et al., 2004; Rudnick and Walker, 2009). As the main host phase of the HSE in mantle rocks, BMS control the Re-Os isotopic system along with platinum group minerals (PGM). Residual BMS are enriched in IPGE (i.e. Ir, Os, Ru) and depleted in PPGE (i.e. Pt, Pd) while metasomatic BMS formed during percolation of basaltic melts are typically enriched in PPGE over IPGE (e.g. Alard et al., 2000). Moreover, volatile rich fluids are thought to form metasomatic BMS enriched in Os over other IPGE (Alard et al., 2011; Delpech et al., 2012; Lee, 2002; Lorand et al., 2004). Hence, the coupled investigation of  $^{187}\text{Os}/^{188}\text{Os}$  and HSE signature of BMS represents a fundamental tool to discriminate and characterize melting and metasomatic processes occurring in the mantle.

In recent years several studies have been carried out on BMS using laser ablation (LA-ICP-MS) for in situ Re-Os dating and HSE characterization (e.g. Alard et al., 2000; Griffin

et al., 2004; Luguet et al., 2001; Pearson et al., 2002). However, the LA-ICP-MS technique has some limitations:

1) Measurements via LA-ICP-MS are affected by the isobaric interference of  $^{187}\text{Re}$  on  $^{187}\text{Os}$  (Nowell et al., 2008; Pearson et al., 2002). The maximum limit on the  $^{187}\text{Re}/^{188}\text{Os}$  ratio for accurate measurements varies in the literature between 0.5 (Nowell et al., 2008) and 3 (Brueckner et al., 2004).

2) The application is restricted to relatively large grains ( $> 50 \mu\text{m}$ ) with a sufficiently high Os content, which varies between 5 and 20  $\mu\text{g/g}$ , depending on the spot size (Reisberg and Meisel, 2002). Moreover, very few grains are large enough ( $> 150 \mu\text{m}$ ) to be analyzed with the two laser spots that are necessary for a combined characterization of HSE signature and  $^{187}\text{Os}/^{188}\text{Os}$ .

3) The presence of ubiquitous polymineral assemblages among BMS grains results in heterogeneous distribution of the HSE even within a single grain. Thus, two LA-ICP-MS measurements (for Re-Os geochronology and HSE signature) carried out in two different volumes of BMS might not be comparable and in any case unrepresentative of the whole BMS grain (Aulbach et al., 2004).

4) Ablation properties of sulfide reference materials and natural BMS can be different due to the large compositional variability of natural BMS assemblages (e.g. Gilbert et al., 2014).

5) Poor inter-laboratory reproducibility observed when sulfide reference materials are cross calibrated (Gilbert et al., 2013).

To date single BMS grains with the Re-Os systematic, Pearson et al. (1998) used an alternative approach based on isotope dilution with chemical separation of the analytes. This technique overcomes the aforementioned issues encountered in LA-ICP-MS analyses and allows the combination of multi-isotope (e.g. Pb and Os Burton et al., 2012; Warren and Shirey, 2012) and elemental (e.g. Re and Os concentrations) analyses from the same BMS grain. Moreover, very precise and accurate measurements can be achieved because of the chemical separation of the analytes from matrix elements and from their isobaric interferences. In the procedure of Pearson et al. (1998), the sample is digested in a  $\text{H}_2\text{SO}_4$ - $\text{CrO}_3$  solution with Os being simultaneously separated by distillation into HBr. Rhenium is

further separated from the residue of the micro-distillation via anion exchange resin. Hereafter, this procedure will be called “S-D $\mu$ D” for “Simultaneous digestion and micro-distillation”. Using a small amount of reagents, the S-D $\mu$ D allows to minimize procedural blank contributions, which can be as low as 5 fg for Os and 50 fg for Re (e.g. Gannoun et al., 2007; Pearson et al., 1998; Wiggers de Vries et al., 2013). A characteristic of S-D $\mu$ D is that the sample-spike equilibration and the Os extraction take place at the same time. Hence, S-D $\mu$ D differs significantly from typical isotope dilution analyses where the full spike-sample equilibration is achieved before extracting the analytes of interest. Pearson et al. (1998) tested the accuracy of S-D $\mu$ D by measuring Os concentrations on fragments of the Filomena iron meteorite and aliquots of an eclogitic BMS grain. These concentrations were then compared with those obtained on the same materials after Carius tubes digestion followed by Os extraction via double distillation-from  $\text{H}_2\text{SO}_4$  (Shirey and Walker, 1995). The Os concentrations obtained after Carius tube digestion and S-D $\mu$ D differ for < 10%.

The single grain procedure of Pearson et al. (1998) is modified here with the addition of elemental analyses of Ru, Pd, Ir, and Pt. A homogeneous sulfide was synthesized and fully characterized before being used to test different micro-analytical procedures optimized for single BMS grain analyses. Variations in the analytical procedure include two digestion methods, different micro-distillation temperatures and two resin-exchange methods. It is here shown that accurate and precise measurements for HSE concentrations and  $^{187}\text{Os}/^{188}\text{Os}$  ratios can be achieved when a pre-digestion step is added to the procedure of Pearson et al. (1998). Concentrations obtained with this modified technique are in agreement with those independently determined after HP-Asher digestion. Deviations are within 10% for Pd, Os and Ir, and within 20% for Ru, Re and Pt. The Os isotopic composition is indistinguishable from the one obtained after HP-Asher digestions within the analytical precision of the method, which is typically 0.01% (2SD, i.e. two times the standard deviation).

### **3.2 *EXPERIMENTAL AND ANALYTICAL METHODS***

A large, homogenous and well characterized sulfide is required to test the accuracy of single BMS grain analytical techniques. For this purpose, the use of natural sulfide

materials has some intrinsic limitations. Mantle or melt-derived BMS are small (typically < 500  $\mu\text{m}$  across) and show ubiquitous polymineral assemblages, resulting in heterogeneous distribution of major and trace elements. Larger BMS can be found in ore deposits but they are also heterogeneous and they are compositionally different when compared to typical mantle BMS. Therefore, the synthesis of a homogenous mantle-like BMS is necessary.

Two sulfides were synthesized and sufficient material was produced to: 1) characterize large fragments (mg amount) for bulk HSE measurements with an already well-established analytical procedure (i.e. isotope dilution combined with HP-Asher digestion); 2) analyze two aliquots with LA-ICP-MS to establish spatial homogeneity of HSE contents; 3) use small fragments (15-340  $\mu\text{g}$ ) to test micro-procedures for analyzing single BMS.

### ***3.2.1 Synthesis of the sulfide standard materials***

The two sulfides (BonnSulfII and BonnSulfVI) were synthesized following the procedure described by Wohlgemuth-Ueberwasser et al. (2007). Sulfur powder (Alfa Aesar, Puratronic 99.9995% purity) was weighed and crushed into an agate mortar. Rhenium was pipetted directly from  $\text{HNO}_3$  based solutions (Alfa Aesar, Specpure) into the sulfur powder before introducing the mixture into an oven at 60  $^\circ\text{C}$  for one day. Ruthenium, Rh, Pd, Os, Ir, and Pt were then added to the powder (Rh was added only to BonnSulfVI) as HCl based solutions (Alfa Aesar, Specpure) before placing the mixture into a drying oven for at least 24 hours at 60  $^\circ\text{C}$ . Iron and Ni metallic powders (Alfa Aesar, Puratronic > 99.995% purity) were then added to obtain a molar sulfide composition of 53% S, 43% Fe, and 4% Ni. This composition was chosen in order to resemble a typical mantle BMS and to avoid the formation of exsolution lamellae during cooling (Wohlgemuth-Ueberwasser et al., 2007).

After crushing and homogenizing the reagents in a mortar, the powder (~200 mg) was introduced into a  $\text{SiO}_2$  glass tube with  $\text{SiO}_2$  wool on top. The tube was then evacuated with a vacuum pump reaching an internal pressure of  $10^{-3}$  Pa. The tube was sealed before placing it in a one atmosphere furnace for 3 days at 900  $^\circ\text{C}$ . After breaking the capsule, the sulfide was carefully extracted to avoid collecting any portion of the glass tube or  $\text{SiO}_2$  wool. The resulting fragments were carefully ground into homogeneous powder using an

agate mortar. The fine material was then transferred into a silica capsule and covered with silicate powder. To better isolate the sulfide material from the Re-W thermocouple (used for checking the temperature during the high pressure synthesis), an additional MgO disk was placed on top of the silica powder during the preparation of BonnSulfVI. The capsule was positioned in a 1/2 inch talc-borosilicate pressure assemblage and introduced into a piston cylinder apparatus for 3 hours at 1.5 GPa and 1050 °C. The resulting materials consist of polycrystalline sulfides exhibiting polygonal textures with a crystal size between 50 and 500  $\mu\text{m}$ .

### ***3.2.2 Characterization of the sulfide standard materials***

#### ***3.2.2.1 Electron microprobe***

Two sulfide fragments, collected from the bottom and the top of the quartz capsule were analyzed with a JEOL JXA 8900 electron microprobe (Steinmann-Institut, Universität Bonn, Germany). No exsolution features were observed in backscatter images and the material appeared monomineralic except for some minor  $\text{SiO}_2$  grains (< 5 vol.%) in BonnSulfII. These fragments are likely remnants of the  $\text{SiO}_2$  wool that was not completely removed during the sulfide preparation. Sulfur, Fe and Ni were measured in wavelength dispersive mode (WDS). Thirteen and eleven spot analyses were performed on BonnSulfII and BonnSulfVI respectively using 15 kV acceleration voltage, 15 nA beam current, and 1  $\mu\text{m}$  beam size. Calibrations were carried out on Canyon Diablo troilite (for Fe and S), and pure Ni metal, following the procedure described in Fonseca et al. (2012).

#### ***3.2.2.2 LA-ICP-MS***

The two synthesized standards were measured via LA-ICP-MS to test for elemental homogeneity and to determine HSE concentrations. The used LA-ICP-MS instrument consists of a Resonetics M50-E ATL excimer 193 nm laser system combined with an X-Series 2 Q-ICP-MS (Steinmann-Institut, Universität Bonn). Measurements were performed monitoring the isotopes  $^{33}\text{S}$ ,  $^{57}\text{Fe}$ ,  $^{60}\text{Ni}$ ,  $^{101}\text{Ru}$ ,  $^{103}\text{Rh}$ ,  $^{105}\text{Pd}$ ,  $^{185}\text{Re}$ ,  $^{189}\text{Os}$ ,  $^{193}\text{Ir}$ , and  $^{195}\text{Pt}$ . Ruthenium, Rh, Pd, Re, Os, Ir, and Pt content were determined on spot analyses using the PGE sulfide reference material PGE\_Ni7b (Wohlgemuth-Ueberwasser et al., 2007) for external calibration. Ablation yield correction was made by internal normalization to  $^{57}\text{Fe}$

(Longerich et al., 1996). The spot size used in the analysis varied between 44 and 100  $\mu\text{m}$ . Laser fluence energy was measured to be 4-6  $\text{J}/\text{cm}^2$  and the frequency was set at 5 Hz.

### 3.2.2.3 Isotope dilution analyses with HP-Asher digestion

For bulk HSE isotope dilution and  $^{187}\text{Os}/^{188}\text{Os}$  characterization, three and four aliquots were taken for BonnSulfII and BonnSulfVI, respectively. Each fragment was weighed using an ultra-microbalance Mettler Toledo XP6U. The error on the weighing is negligible due to the relatively large amount of analyzed material ( $> 1$  mg). After weighing, the fragments were introduced in quartz reaction vessels before adding a multi-element spike solution ( $^{99}\text{Ru}$ ,  $^{106}\text{Pd}$ ,  $^{185}\text{Re}$ ,  $^{190}\text{Os}$ ,  $^{191}\text{Ir}$  and  $^{194}\text{Pt}$ ) and 7.5 ml of reverse *aqua regia* (2.5 ml concentrated HCl and 5 ml concentrated  $\text{HNO}_3$ ). Due to the immediate reaction, the reverse *aqua regia* was introduced ice-cold and any sulfide fragment attached to the vessel walls was washed out while adding the acids. BonnSulfII and BonnSulfVI fragments were digested for 14 hours in an Anton Paar HP-Asher at 220  $^\circ\text{C}$  and  $> 100$  bar. After digestion, the solutions were clear and no solid particles were observed. Osmium was extracted from the reverse *aqua regia* using  $\text{CHCl}_3$  or  $\text{CCl}_4$  and then back-extracted into HBr (Cohen and Waters, 1996). The HBr solutions containing Os were dried down and re-dissolved in  $\text{H}_2\text{SO}_4$  before being microdistilled using a  $\text{Cr}^{6+}$ - $\text{H}_2\text{SO}_4$  solution (Birck et al., 1997). After extracting the Os, the reverse *aqua regia* solutions were dried down, re-dissolved in 10 mL 6 N HCl, dried down again and re-dissolved in 5 mL 0.5 M HCl. The solutions were then loaded onto columns filled with 1 mL of a Bio-Rad AG1X-8 (100–200 mesh) anion exchange resin. Ruthenium, Pd, Re, Ir, and Pt were collected following the procedure of Pearson and Woodland (2000) and modified by Luguét et al. (2015).

### 3.2.3 Single grain procedures

Fragments of the two synthesized sulfides were used to test different analytical procedures for single grain analysis. The grains were weighed with a Mettler Toledo XP6U ultra-microbalance (0.1  $\mu\text{g}$  nominal precision). Every fragment was weighed between 5 and 15 times to assess weighing errors. Repeated weighing of the same grain yielded a reproducibility of about  $\pm 0.3$   $\mu\text{g}$  resulting in almost negligible error (minimum weight 15  $\mu\text{g}$ ). Twenty fragments were treated following the S-D $\mu$ D procedure of Pearson et al. (1998). Twenty-one more tests were performed adding a pre-digestion step. This procedure

will be called “Pre-digestion followed by microdistillation” or “P-D $\mu$ D”. The S-D $\mu$ D and P-D $\mu$ D procedures are described hereafter.

### 3.2.3.1 *Simultaneous digestion and microdistillation (S-D $\mu$ D)*

A multi-elemental HSE spike solution (HCl based) was pipetted and weighed on the center of a lid of a 5 mL PFA Savillex conical vial (step 1S in Figure 3-1). The lid was then placed on a hotplate at 60 °C (step 2S in Figure 3-1). Once the spike droplet was fully evaporated, 10  $\mu\text{L}$  12 M  $\text{H}_2\text{SO}_4$  (Millipore-Ultrapur) were pipetted to the lid being careful to re-dissolve the spike by moving the  $\text{H}_2\text{SO}_4$  drop around the center of the lid. The sulfide fragment was placed on the top of the  $\text{H}_2\text{SO}_4$  drop before adding 10  $\mu\text{L}$  of a 4 M  $\text{H}_2\text{SO}_4$  solution saturated in  $\text{Cr}^{6+}$  (Aldrich) (step 3S in Figure 3-1).

### 3.2.3.2 *Pre-digestion followed by microdistillation (P-D $\mu$ D)*

The sulfide fragments were first digested in 5-7 mL PFA Savillex beakers. A multi-element HSE spike solution was added to the beaker followed by 1 mL of reagent. For this purpose three different reagents were used: concentrated HBr (~9 M), concentrated HCl (~10 M) or a diluted mixture of both (0.4 mL concentrated HCl + 0.4 mL concentrated HBr + 0.2 mL  $\text{H}_2\text{O}$ -MQ). The sulfide fragment was then introduced in the beaker, which was immediately closed and placed on a hotplate (step 1P in Figure 3-1). The temperature of the hotplate during the digestion was varied between 90 and 120 °C. After about 8 and 20 hours on the hotplate, the warm beaker was placed in an ultrasonic bath for 15 minutes, and then put back on the hotplate. After a total of at least 48 hours on the hotplate, the beaker was allowed to cool down and was subsequently opened and checked for any solid particles before evaporating the solution on a hotplate at 70 °C (step 2P in Figure 3-1). Once evaporated, four tests were further treated with the following extra re-dissolution step: 1) 0.5 mL 8 M HCl were added to the residue (step 3P-b1 in Figure 3-1); 2) the beaker was placed on hotplate at 70 °C until the volume is reduced to < 100  $\mu\text{L}$ ; 3) the solution was transferred to the lid of a conical vial (step 3P-b2 in Figure 3-1); 4) the solution was evaporated to dryness at 70 °C; 5) the residue was re-dissolved in 10  $\mu\text{L}$  12 M  $\text{H}_2\text{SO}_4$  (step 3P-b3 in Figure 3-1). When the extra re-dissolution step was not performed, the residue was directly re-dissolved with 10  $\mu\text{L}$  12 M  $\text{H}_2\text{SO}_4$  (step 3P-a1 in Figure 3-1) inside the 5-7

mL beaker. The  $\text{H}_2\text{SO}_4$  drop was then transferred to the lid of a conical vial before adding  $10 \mu\text{L}$  of a  $4 \text{ M H}_2\text{SO}_4$  solution saturated in  $\text{Cr}^{6+}$  (steps 3P-a2 in Figure 3-1).

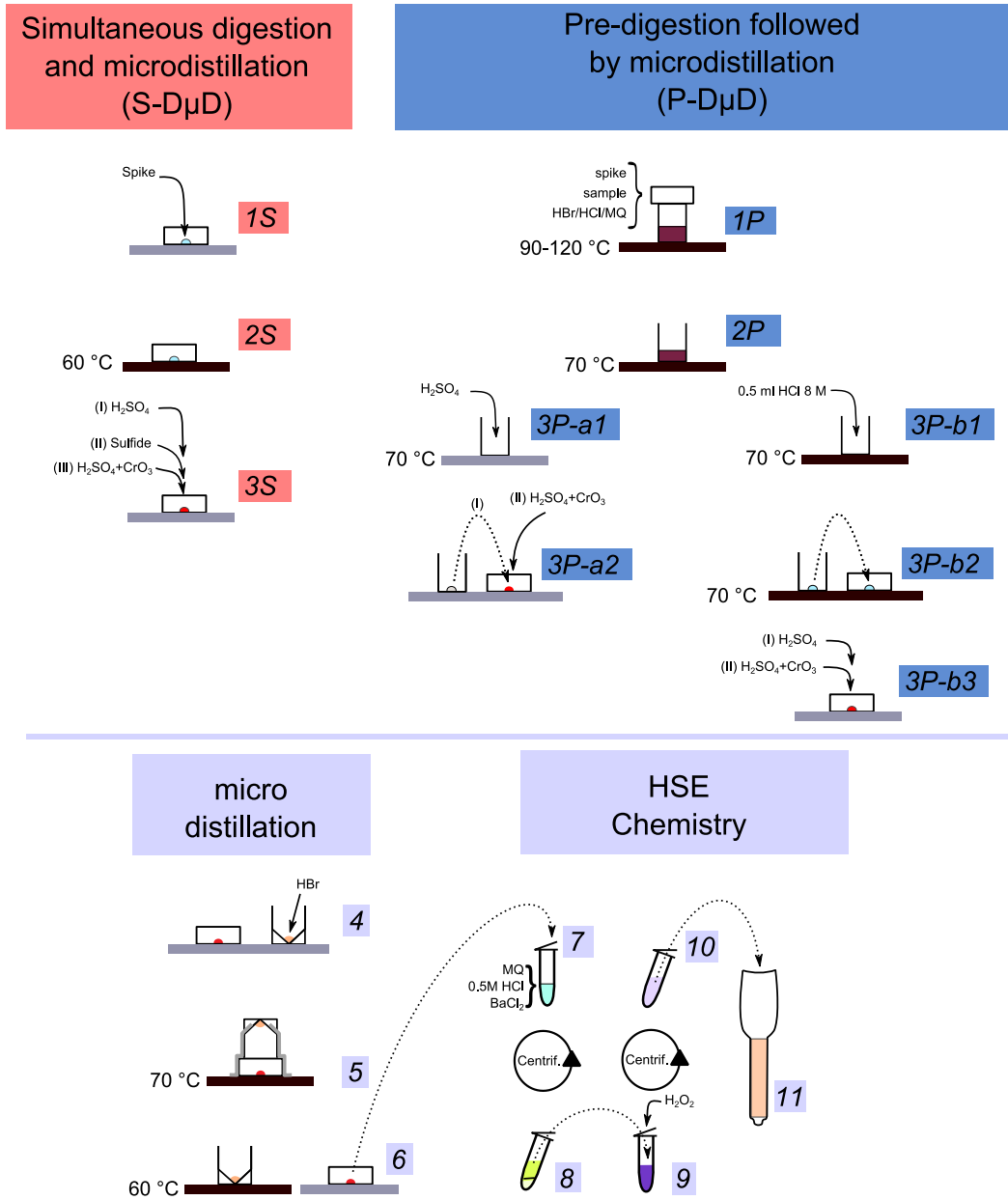


**Figure 3-1** Flowchart describing the different procedures tested for single grain chemistry.

### 3.2.3.3 Microdistillation

After adding the  $\text{H}_2\text{SO}_4\text{-Cr}^{6+}$  solution, the procedure proceeds in a similar way for both P-D $\mu$ D and S-D $\mu$ D. The first step consists in the typical micro-distillation technique (from step 4 to 6 in Figure 3-1) that is also used for Os purification during whole rock Os chemistry (Birck et al., 1997). During the micro-distillation, the  $\text{H}_2\text{SO}_4\text{-Cr}^{6+}$  solution acts as strong oxidizing agent, it digests the sulfide in the case of S-D $\mu$ D, and it promotes the formation of the highly volatile  $\text{OsO}_4$ . The Os released from the spike and the sulfide is then trapped in the HBr drop where it is reduced to form  $\text{OsBr}_6^{2-}$  (Birck et al., 1997).

Ten  $\mu\text{L}$  of concentrated HBr were placed on the tip of the conical vial (step 4 in Figure 3-1). The vial was closed upside down being careful to avoid moving/dislodging the  $\text{H}_2\text{SO}_4\text{-Cr}^{6+}$  and HBr drops. The vial was then wrapped in aluminum foil, leaving only the tip uncovered and placed on hotplate (step 5 in Figure 3-1). The duration of the micro-distillation ranged from 2 to 20 hours and the temperature of the hotplate was set at 70 or 80 °C. After the micro-distillation, the beaker was carefully opened and the HBr drop in the conical tip of the vial was dried down. The  $\text{H}_2\text{SO}_4\text{-Cr}^{6+}$  solution was then treated to collect the Ru, Pd, Re, Ir, and Pt fractions.

### 3.2.3.4 HSE chemistry: Pre-treatment

After the micro-distillation all the HSE, except Os, are contained in the  $\text{H}_2\text{SO}_4\text{-Cr}^{6+}$  residue. This solution was transferred to a 1.5 mL centrifuge tube together with 100  $\mu\text{L}$  of  $\text{H}_2\text{O-MQ}$  and 400  $\mu\text{L}$  1 M (anion chemistry) or 0.2 M (cation chemistry) HCl. One hundred  $\mu\text{L}$  of a  $\text{BaCl}_2$  saturated solution was added to precipitate  $\text{H}_2\text{SO}_4$  and  $\text{Cr}^{6+}$  as  $\text{BaSO}_4$  and  $\text{BaCrO}_4$ , respectively (step 7 in Figure 3-1). The centrifuge tube was placed in a vortex and in a centrifugation device before removing the precipitate by transferring the supernatant liquid into a new 1.5 mL centrifuge tube (step 8 in Figure 3-1). After transferring the supernatant liquid into a new centrifuge tube, any  $\text{Cr}^{6+}$  still present in the liquid was further reduced to  $\text{Cr}^{3+}$  by the addition of 20  $\mu\text{L}$   $\text{H}_2\text{O}_2$  (Pearson et al., 1998).

The treatment with  $\text{BaCl}_2$  is necessary because the  $\text{H}_2\text{SO}_4$  residue is otherwise not fully removed during the following column chemical separation and can therefore disturb the HSE measurements via ICP-MS. Tests done with a ThermoScientific Element XR SF-ICP-

MS (Steinmann-Institut, Universität Bonn) revealed that the HSE background measured in 0.5 M HCl changes significantly when traces (~3 vol %) of H<sub>2</sub>SO<sub>4</sub> are added. During one day of testing, this effect was particularly pronounced for Ir as the background signal was observed to increase of about ten times in the presence of H<sub>2</sub>SO<sub>4</sub>. A change in the background signal in the presence of H<sub>2</sub>SO<sub>4</sub> is likely due to “transport effects” as small amounts of H<sub>2</sub>SO<sub>4</sub> can significantly change the physical conditions during sample introduction (e.g. during the nebulization process) in the ICP-MS (Hu and Qi, 2014; Todolí and Mermet, 1999). However, it remains unclear why this effect was more pronounced for Ir than for other HSE.

### 3.2.3.5 Anion and cation HSE separation

Six tests resulting from the previous S-D $\mu$ D and P-D $\mu$ D were treated with anion exchange chromatography (Pearson and Woodland, 2000) using 150  $\mu$ L of Bio-Rad AG1X-8 (100–200 mesh) resin loaded in columns prepared from polyethylene Pasteur pipettes. Seventeen more tests were treated with cation exchange chromatography (Ely et al., 1999) using 2 mL of Dowex 50W-X8 (200–400 mesh) resin loaded in a Bio-Rad polypropylene column. In eight tests the cation exchange procedure was repeated twice in order to further purify the HSE fractions.

The anion exchange procedure was obtained by scaling down the whole rock HSE separation procedure of Pearson and Woodland (2000) and modified by Luguét et al. (2015). The resin was cleaned with 0.8 mL H<sub>2</sub>O-MQ, 0.8 mL 13.5 M HNO<sub>3</sub>, 0.8 mL H<sub>2</sub>O-MQ, 0.8 mL 9 M HCl and pre-conditioned with 0.8 mL 1 M HCl. The solution containing the digested sulfide fragment was loaded in ~0.5 mL 1 M HCl and eluted with 1.5 mL 1 M HCl, 0.8 mL H<sub>2</sub>O-MQ, 0.8 mL 0.8 M HNO<sub>3</sub> to remove matrix elements. The cut containing Re, Ir, Pt, and Ru was then collected with 3 mL 13.5 M HNO<sub>3</sub>. Further 0.8 mL H<sub>2</sub>O-MQ were eluted before collecting in a new beaker the Pd cut with 3.5 mL 9 M HCl. The 13.5 M HNO<sub>3</sub> cut was evaporated and re-dissolved in 0.5 M HCl for Re, Ir, and Pt measurements. After carrying out the ICP-MS analyses for these elements, the leftover solution (ca. 50% of the original one) was transferred into the dried 9 M HCl cut, evaporated and re-dissolved in 0.56 M HNO<sub>3</sub> for Ru and Pd measurements.

The cation exchange resin was cleaned with 15 mL 6 M HCl and pre-conditioned with 10 mL 0.2 M HCl. The solution containing the digested sulfide fragment was loaded in ~0.5 mL 0.2 M HCl. The HSE cut was collected upon loading and during the following two elutions with 1 mL 0.2 M HCl. After evaporation, the HSE cut was re-dissolved in 0.5 M HCl for Re, Ir, and Pt measurements. The leftover solution was then evaporated again and re-dissolved in 0.56 M HNO<sub>3</sub> for Ru and Pd measurements.

### 3.2.4 Mass spectrometry

The Os isotopic and elemental composition was measured at the Northern Centre for Isotopic and Elemental Tracing (NCIET) of the University of Durham (UK) by thermal ionization mass spectrometry in negative ion mode (N-TIMS) using a ThermoScientific Triton. Osmium was loaded in concentrated HBr (Romil) on a 99.99% Pt-filament with ~0.5  $\mu\text{L}$  of a 0.1 M NaOH/Ba(OH)<sub>2</sub> solution as activator (Luguet et al., 2008). Osmium was measured as  $\text{OsO}_3^-$  and any isobaric interference of  $^{187}\text{ReO}_3^-$  on  $^{187}\text{OsO}_3^-$  was monitored and corrected by measuring  $^{185}\text{ReO}_3^-$ . All measurements were performed in peak jumping mode using an electron multiplier and analyzing  $^{185}\text{ReO}_3^-$ ,  $^{186}\text{OsO}_3^-$ ,  $^{187}\text{OsO}_3^-$ ,  $^{188}\text{OsO}_3^-$ ,  $^{189}\text{OsO}_3^-$ ,  $^{190}\text{OsO}_3^-$ ,  $^{192}\text{OsO}_3^-$ . Each mass was corrected for isobaric oxide interference formed by  $^{17}\text{O}$  and  $^{18}\text{O}$  with other lighter Os isotopes. Mass fractionation is corrected using  $^{192}\text{Os}/^{188}\text{Os} = 3.083$  (Luguet et al., 2008). Accuracy was daily monitored by measuring 10 and 100 pg loads of the Durham Romil Os Standard (DROsS, Luguet et al., 2008) prior to sample measurements. The  $^{187}\text{Os}/^{188}\text{Os}$  measured in DROsS (average 0.16094, SD = 0.00016, n = 5) is in good agreement with the range reported by Luguet et al. (2008) ( $^{187}\text{Os}/^{188}\text{Os} = 0.160924$ , SD = 0.000004) who used larger loads of Os (10-100 ng).

Ruthenium, Pd, Re, Ir, and Pt were analyzed with a ThermoScientific Element XR SF-ICP-MS (Steinmann-Institut, Universität Bonn). Rhenium, Ir, and Pt were measured in the same session using a double pass spray chamber made of borosilicate glass. Hafnium oxide interferences on  $^{193}\text{Ir}$ ,  $^{194}\text{Pt}$ ,  $^{195}\text{Pt}$ , and  $^{196}\text{Pt}$  were corrected by analyzing  $^{178}\text{Hf}$  in each measurement and by quantifying the Hf oxide production on a 1  $\mu\text{g/L}$  Hf standard solution at the beginning and the end of each analytical session. Palladium and Ru were measured in 0.56 M HNO<sub>3</sub> using an ESI-Apex introduction system in order to minimize molecular

interferences. Oxide interferences on Pd isotopes were corrected measuring  $^{89}\text{Y}$ ,  $^{90}\text{Zr}$ , and  $^{95}\text{Mo}$  after estimating their relative oxide production by running 1  $\mu\text{g/L}$  Y, Zr, and Mo standard solutions. Possible isobaric interferences of Cd on Pd isotopes were monitored using the mass 111. One single analysis for Re, Ir, Pt, or Ru-Pd consists of 50 measurements of each mass for a total measurement time of ~150 seconds.

### **3.3 RESULTS**

#### **3.3.1 Total procedural blanks**

Total procedural blanks were obtained for HP-Asher digestions and single BMS grain procedures (Table 3-1). The only HP-Asher blank shows high Os content (30 pg) when compared to blanks routinely obtained for the same analytical procedure in the same laboratory (usually  $< 1$  pg, e.g. Lissner et al. 2014, Luguet et al. 2015). The procedural blank yielded  $^{187}\text{Os}/^{188}\text{Os} = 0.161$ , which suggests that the high Os content results from cross contamination during the chemical procedure. However, the large amount of Os contained in sulfide fragments dissolved via HP-Asher (minimum 8.4 ng of Os) makes any blank correction negligible ( $< 1\%$ ). HP-Asher procedural blanks for Ru, Pd, Re, Ir, and Pt are 50, 3.0, 0.8, 1.6, 4.8 pg, respectively, and in agreement with blanks routinely obtained in the same laboratory (Lissner et al., 2014; Luguet et al., 2015).

For the single BMS grain procedure, Os procedural blanks show a variation between 22 and 150 fg ( $n = 9$ , average = 86 fg, Table 3-1). Other HSE blanks (Table 3-1) vary between 0.5 pg and 95 pg for Pd ( $n = 10$ , average = 14 pg), 0.03 pg and 4.3 pg for Re ( $n = 11$ , average 2.1 pg), 0.4 pg and 1.4 pg for Ir ( $n = 8$ , average 0.6 pg), and 0.07 pg and 2.8 pg for Pt ( $n = 10$ , average 1.4 pg). No reliable procedural blanks were obtained for Ru due to the poor counting statistics of the measurements. However, despite the large uncertainties, counts on  $^{101}\text{Ru}/^{99}\text{Ru}$  were always  $< 1$  ( $n = 4$ ), which correspond to blanks  $< 30$  pg. The  $^{187}\text{Os}/^{188}\text{Os}$  ratio measured in blanks ( $n = 5$ ) varies between 0.298 and 0.137, with an average value of 0.190. Overall, there is no systematic difference between HSE blanks obtained with P-D $\mu$ D and S-D $\mu$ D (Table 3-1). The large variation in both P-D $\mu$ D and S-D $\mu$ D blanks show that there was no significant contribution from the reagents and that the

main blank sources are un-systematic. Despite the small size of the analyzed sulfides, any blank correction is negligible (< 1%).

**Table 3-1** Procedural blanks obtained using different digestion methods.

blanks	Predigestion steps		Microdis.		HSE resin	Ru pg	Pd pg	Re pg	Os pg	Ir pg	Pt pg	
	step I	T °C	step II	t hrs								T °C
<b>S-D<math>\mu</math>D</b>												
blkAB61			2	70		-	-	-	0.034	-	-	
blkAB62			20	70		-	-	-	0.141	-	-	
blkAB66			2	70	anion	-	2.87	3.10	0.022	0.92	2.70	
blkAB65			20	70	cation	-	0.47	1.67	0.079	0.05	1.52	
<b>P-D<math>\mu</math>D</b>												
blkAB60	HBr	90	14	70		-	-	#	0.152	#	#	
blkAB64	HBr	120	2	70		-	-	-	0.062	-	-	
blkAB63	HBr	90	20	70	cation	-	15.64	1.58	-	1.36	2.81	
blkAB59	HBr	90	14	70	cation	-	-	0.03	-	#	#	
blkAB67	HBr	120	2	70	cation	-	1.67	1.91	-	#	1.37	
blkAB68	HBr	120	2	70	cation	-	3.87	1.81	-	0.40	1.29	
blkAB70	HBr	120	2	70	cation	-	0.72	1.58	-	#	1.23	
blkAB73	HBr	120	2	70	2*cation	§	5.39	2.45	0.140	0.06	0.07	
blkAB74	HBr	120	HCl	2	70	2*cation	§	94.94	1.84	0.110	0.69	1.51
blkAB75	HBr+HCl	120	2	70	2*cation	§	11.01	3.19	0.035	0.77	0.91	
blkAB76	HBr+HCl	120	HCl	2	70	2*cation	§	3.68	4.26	-	0.04	0.32
HP-Asher digestion						50	3.0	0.77	30	1.63	4.78	

Step I is the main reagent used to dissolve the sulfide in P-D $\mu$ D, Step II is the reagent used for re-dissolving the residue before micro-distillation. (#) measurement yielding negative concentration. (§) Ruthenium measurement with poor counting statistics as the background/sample signal is > 50% for at least one of the masses used for isotope dilution calculations (i.e.  $^{99}\text{Ru}$  and  $^{101}\text{Ru}$ ). (-) not analyzed.

### 3.3.2 Composition of the two synthesized sulfide standards

Electron microprobe analyses show S, Fe, and Ni molar (%) content of 52.2 (SD = 0.3), 44.5 (SD = 0.3), 3.3 (SD = 0.1) for BonnSulfII (n = 13) and 50.8 (SD = 0.2), 45.8 (SD = 0.2), 3.4 (SD = 0.1) for BonnSulfVI (n = 11). For each sulfide standard the microprobe analyses were performed on two different portions of the sample (bottom and top of the experimental run). The small standard deviation proves that the distribution of all major elements is homogeneous within the two synthesized sulfides.

Laser ablation spot analyses (LA-ICP-MS) show a standard deviation < 10% for every HSE except for Re in BonnSulfII (Table 3-2). Moreover, anomalous peaks in the HSE signals were not observed in any LA-ICP-MS spectra. This proves that the synthesized materials have a homogenous HSE distribution at the scale of tens of microns (except Re in

BonnSulfII). The poor reproducibility of Re concentrations in LA-ICP-MS analyses from BonnSulfII (average = 2  $\mu\text{g/g}$ , SD = 71%) is due to four spots analysis with very high Re content (up to 7  $\mu\text{g/g}$ ). These spot analyses were performed in the middle of the top portion of the experimental run, which was in close proximity to the Re-W thermocouple wire during the piston cylinder synthesis. If these spot analyses are excluded, the average Re concentration in BonnSulfII is 1.5  $\mu\text{g/g}$  ( $n = 16$ ) and the standard deviation is 0.1  $\mu\text{g/g}$  (6% RSD, i.e. the relative standard deviation). The Re enriched area is not observed in BonnSulfVI where a MgO disk was placed between the top of the quartz capsule and the tip of the thermocouple.

The average HSE content measured with ID-ICP-MS after HP-Asher digestion varies between 1.5  $\mu\text{g/g}$  (Re) and 11.1  $\mu\text{g/g}$  (Ir) in BonnSulfII and between 3.9  $\mu\text{g/g}$  (Re) and 20.8  $\mu\text{g/g}$  (Ir) in BonnSulfVI (Table 3-2). The replicates for BonnSulfII ( $n = 3$ ) and BonnSulfVI ( $n = 4$ ) show an excellent reproducibility in HSE concentrations as they yield a RSD that is typically  $< 2\%$  (Ru, Ir, Pt in BonnSulfII and Ru, Pd, Ir, Pt in BonnSulfVI) and always  $< 4\%$ . The only exception is Re in BonnSulfII that displays a RSD of 18%. The calculated average for  $^{187}\text{Os}/^{188}\text{Os}$  is 0.16001 in BonnSulfII and 0.16052 in BonnSulfVI (Table 3-2). The  $^{187}\text{Os}/^{188}\text{Os}$  measured in different aliquots are always in agreement within two times the standard deviation of the analytical error, except ID1 and ID3 from BonnSulfVI where they overlap within three times the standard deviation of the analytical error (Table 3-2).

Overall, the average concentrations obtained by ID-ICP-MS and LA-ICP-MS are in agreement within 10% for both, BonnSulfVI and BonnSulfII (Table 3-2). Hereafter, the concentrations obtained after HP-Asher digestions are used as reference values as this isotope dilution procedure is largely accepted to provide accurate and precise HSE compositional data (e.g. Meisel et al., 2003), while LA-ICP-MS data are more easily affected by analytical biases (e.g. isobaric and polyatomic interferences, calibration of the reference materials).

**Table 3-2** Highly Siderophile Element concentrations (Ru, Rh, Pd, Re, Os, Ir, Pt) and isotopic composition ( $^{187}\text{Os}/^{188}\text{Os}$ ) of the two synthesized standards via HP-Asher digestions and LA-ICP-MS.

	weight mg	$^{187}\text{Os}/^{188}\text{Os}$	$\pm$	Ru $\mu\text{g/g}$	Rh $\mu\text{g/g}$	Pd $\mu\text{g/g}$	Re $\mu\text{g/g}$	Os $\mu\text{g/g}$	Ir $\mu\text{g/g}$	Pt $\mu\text{g/g}$
<b>BonnSulfII</b>										
<i>Isotope dilution (HPA digestion)</i>										
ID 1	4.472	0.16004	0.00009	4.8		7.1	1.4	8.4	11.3	10.8
ID 2	2.042	0.16004	0.00016	5.0		7.5	1.3	8.4	11.2	10.8
ID 3	2.058	0.15996	0.00048	4.8		7.5	1.8	8.9	11.0	10.7
Average		<b>0.16001</b>		<b>4.9</b>		<b>7.4</b>	<b>1.5</b>	<b>8.6</b>	<b>11.1</b>	<b>10.8</b>
SD		0.00005		0.1		0.2	0.3	0.3	0.2	0.1
RSD (%)		0.03		1.7		3.3	17.6	3.3	1.6	0.5
<i>LA-ICP-MS</i>										
Average (n = 20)				5.4		7.9	2.0	9.8	11.2	10.0
SD (n = 20)				0.4		0.2	1.4	0.4	0.4	0.3
RSD (%)				7		2	71	4	4	3
<b>BonnSulfVI</b>										
<i>Isotope dilution (HPA digestion)</i>										
ID 1	2.8122	0.16066	0.00010	19.4		16.4	3.9	19.0	21.0	17.7
ID 2	3.0017	0.16050	0.00015	19.2		16.4	3.8	18.9	20.9	17.4
ID 3	5.7928	0.16036	0.00010	19.2		16.4	4.1	17.6	20.2	17.8
ID 4	0.4374	0.16057	0.00028	19.6		16.0	3.9	19.2	21.1	17.7
Average		<b>0.16052</b>		<b>19.4</b>		<b>16.3</b>	<b>3.9</b>	<b>18.6</b>	<b>20.8</b>	<b>17.6</b>
SD		0.00011		0.2		0.2	0.1	0.6	0.4	0.2
RSD (%)		0.07		0.9		1.0	2.8	3.3	1.7	0.9
<i>LA-ICP-MS</i>										
Average (n = 35)				21.7	20.4	17.0	4.4	22.6	21.3	16.6
SD (n = 35)				1.5	0.9	0.8	0.4	1.4	1.3	1.0
RSD (%)				6.9	4.5	4.7	8.1	6.2	5.9	6.3

Replicate analyses by isotope dilution (ID) from the same sulfide material standard yielded very reproducible HSE concentrations and Os isotopic composition. Their average is considered as the best estimate for trace element content in the two sulfides. HPA : HP-Asher. The uncertainty on  $^{187}\text{Os}/^{188}\text{Os}$  is expressed as 2SD.

### 3.3.3 Osmium concentration and $^{187}\text{Os}/^{188}\text{Os}$ in single grain procedures

In order to test the ability of S-D $\mu$ D and P-D $\mu$ D to provide reliable Os isotopic and elemental composition, the results obtained with these two techniques are compared to the ones determined after HP-Asher digestion.

Single grain tests on BonnSulfII were done only for S-D $\mu$ D (Table 3-3). These five tests were performed varying the temperature (70 and 80 °C) and the duration of the micro-distillation (2-20 hours). In all of them no solid residue was observed after the S-D $\mu$ D. The Os concentration varies between 7 and 11  $\mu\text{g/g}$  and only one test yielded a concentration (8.5  $\mu\text{g/g}$ ) that overlaps with the concentration range obtained after HP-Asher digestion (8.4-8.9  $\mu\text{g/g}$ ) (Figure 3-2A). The  $^{187}\text{Os}/^{188}\text{Os}$  varies between 0.1596 and 0.1603, with an average of 0.1600 which is similar to that observed after HP-Asher digestion (0.1601) (Figure 3-3B). One test with long micro-distillation duration (20 hours) yielded  $^{187}\text{Os}/^{188}\text{Os} = 0.1595$ , which does not overlap with the HP-Asher range within the analytical error (Figure 3-3B).

Most of the tests ( $n = 36$ ) were carried on BonnSulfVI (Table 3-3). No solid residues, clearly attributable to undigested sulfide fragments, were observed in these tests after S-D $\mu$ D and P-D $\mu$ D in HBr or HBr + HCl. On the contrary, after P-D $\mu$ D in HCl only, a clear solid particle was recovered. The shape of this solid particle resembled that of the starting fragment suggesting that the sulfide was barely digested.

**Table 3-3** Highly Siderophile Elements concentrations (Ru, Pd, Os, Re, Ir, and Pt) and isotopic composition (<sup>187</sup>Os/<sup>188</sup>Os) obtained in BonnSulfVI and BonnSulfII using S-D $\mu$ D and P-D $\mu$ D.

sample name	wt. $\mu$ g	Predigestion steps			Microdis.		HSE resin	<sup>187</sup> Os/ <sup>188</sup> Os $\pm$	Ru $\mu$ g/g	Pd $\mu$ g/g	Re $\mu$ g/g	Os $\mu$ g/g	Ir $\mu$ g/g	Pt $\mu$ g/g	
		step I	T $^{\circ}$ C	step II	t hrs	T $^{\circ}$ C									
<b>BonnSulfII</b>															
<i>S-D<math>\mu</math>D</i>															
SGBNII-2	204.9				20	80		0.1595 0.0001	-	-	-	10.9	-	-	
SGBNII-3	141.2				2	80		0.1602 0.0001	-	-	-	8.5	-	-	
SGBNII-4	28.7				2	80		0.1602 0.0002	-	-	-	10.7	-	-	
SGBNII-5	15.4				2	70		0.1603 0.0002	-	-	-	9.5	-	-	
SGBNII-6	137.0				2	70		0.1596 0.0007	-	-	-	7.1	-	-	
<i>HP-Asher average (n = 3)</i>								<i>0.1600</i>	<i>4.9</i>	<i>7.4</i>	<i>1.5</i>	<i>8.6</i>	<i>11.1</i>	<i>10.8</i>	
<b>BonnSulfVI</b>															
<i>S-D<math>\mu</math>D</i>															
SGBNVI-32	28.6				2	70		0.1605 0.0002	-	-	-	36.9	-	-	
SGBNVI-9	40.4				2	70		0.1604 0.0001	-	-	-	23.9	-	-	
SGBNVI-10	79.1				2	70		0.1607 0.0001	-	-	-	21.8	-	-	
SGBNVI-2	344.0				2	70		æ	-	-	-	9.9	-	-	
SGBNVI-28	72.5				2	70	an.	0.1606 0.0001	°	17.2	3.7	26.6	0.2	0.2	
SGBNVI-29	33.6				2	70	an.	0.1604 0.0001	°	17.2	3.7	41.2	0.3	0.3	
SGBNVI-30	43.3				2	70	cat.	0.1604 0.0002	°	16.2	3.4	28.6	5.3	0.2	
SGBNVI-31	28.2				2	70	cat.	0.1604 0.0001	°	16.6	3.5	25.2	6.7	0.2	
SGBNVI-8*	25.5				2	70		0.1608 0.0002	-	-	-	-	-	-	
SGBNVI-12	64.2				20	70		§	-	-	-	28.6	-	-	
SGBNVI-24	38.8				20	70	an.	0.1606 0.0001	°	16.1	3.6	38.7	1.9	0.2	
SGBNVI-25	36.4				20	70	an.	0.1605 0.0002	°	16.2	3.5	31.4	0.9	0.6	
SGBNVI-26	27.4				20	70	cat.	0.1604 0.0002	°	16.9	3.1	52.1	5.7	0.3	
SGBNVI-27	32.6				20	70	cat.	0.1606 0.0001	°	15.9	3.3	45.0	6.2	0.4	
SGBNVI-1	131.3				20	80		0.1601 0.0001	-	-	-	28.7	-	-	
<i>P-D<math>\mu</math>D</i>															
SGBNVI-4	99.1	HCl	90		14	70		0.1583 0.0005	-	-	-	0.7	-	-	
SGBNVI-5	28.3	HBr	90		14	70		0.1607 0.0002	-	-	-	12.4	-	-	
SGBNIV-6	35.1	HBr	90		14	70		0.1604 0.0001	-	-	-	12.0	-	-	
SGBNVI-15	20.8	HBr	90		20	70	an.	0.1608 0.0001	°	15.7	3.5	14.9	#	12.7	
SGBNVI-16	46.1	HBr	90		20	70	an.	0.1599 0.0002	°	13.4	2.9	11.2	#	14.0	
SGBNVI-19	18.4	HBr	90		2	70	cat.	0.1604 0.0001	°	14.2	3.8	14.5	17.0	10.2	
SGBNVI-17	21.3	HBr	90		20	70	cat.	0.1598 0.0001	°	16.3	3.1	12.7	17.3	24.7	
SGBNVI-18	37.1	HBr	90		20	70	cat.	0.1602 0.0003	°	14.6	2.6	8.5	18.2	57.2	
SGBNVI-13	67.6	HBr	120		2	70		0.1603 0.0003	-	-	-	18.5	-	-	
SGBNVI-14	43.4	HBr	120		2	70		0.1604 0.0001	-	-	-	19.9	-	-	
SGBNVI-23	35.2	HBr	120		2	70		0.1603 0.0001	-	-	-	16.0	-	-	
SGBNVI-21	52.3	HBr	120		2	70	cat.	0.1605 0.0001	°	18.0	3.9	19.6	21.9	16.2	
SGBNVI-22	26.3	HBr	120		2	70	cat.	0.1605 0.0001	°	15.1	3.3	18.3	20.5	13.7	
SGBNVI-42	17.6	HBr	120		2	70	2*cat	æ		15.9	16.3	3.6	17.5	#	14.1
SGBNVI-43	50.0	HBr	120		2	70	2*cat	0.1603 0.0001		18.4	16.4	3.8	17.0	25.6	14.6
SGBNVI-44	45.8	HBr	120	HCl	2	70	2*cat	0.1604 0.0003		17.6	16.1	5.5	17.6	16.7	15.3
SGBNVI-45	33.7	HBr	120	HCl	2	70	2*cat	-		16.8	15.8	4.6	-	16.7	14.5
SGBNVI-48	18.1	HBr+HCl	120	HCl	2	70	2*cat	-		18.8	16.6	4.6	-	19.5	17.0
SGBNVI-49	28.8	HBr+HCl	120	HCl	2	70	2*cat	-		20.4	16.9	4.2	-	20.4	17.0
SGBNVI-46	46.7	HBr+HCl	120		2	70	2*cat	0.1600 0.0001		22.9	16.6	3.7	15.9	20.5	15.8
SGBNVI-47	39.3	HBr+HCl	120		2	70	2*cat	0.1606 0.0004		23.3	16.5	4.2	19.2	22.0	16.3
<i>HP-Asher average (n = 4)</i>								<i>0.1605</i>	<i>19.4</i>	<i>16.3</i>	<i>3.9</i>	<i>18.6</i>	<i>20.8</i>	<i>17.6</i>	

Step I is the main reagent used to dissolve the sulfide in P-D $\mu$ D, Step II is the reagent used for re-dissolving the residue before micro-distillation. cat : cation, an : anion. Uncertainties are expressed as 2SD. \*Unspiked. (#) measurement with poor counting statistics as the background/sample signal is > 10% for at least one of the masses used for isotope dilution calculations. (°) Unreliable Ru analysis due to shift in <sup>101</sup>Ru/<sup>99</sup>Ru over the time of the measurement. (§) anomalous TIMS analysis with Os isotopic ratios changing over time (<sup>190</sup>Os/<sup>188</sup>Os increased of about 1%). The observed shifts do not have a significant effect on the calculated Os concentrations. (æ) Measurement with signal on mass 233 (<sup>185</sup>Re<sup>16</sup>O<sub>3</sub>) higher than 0.003\*[signal on mass 235]. These measurements, when corrected for the <sup>187</sup>ReO<sub>3</sub> isobaric interference on <sup>187</sup>OsO<sub>3</sub> (mass 235), yield anomalously low <sup>187</sup>Os/<sup>188</sup>Os ( $\leq$  0.1592). This is possibly due to secondary interferences on mass 233, which were also observed running blank filaments. Thus, these measurements are considered unreliable and are not reported. (-) not analyzed.

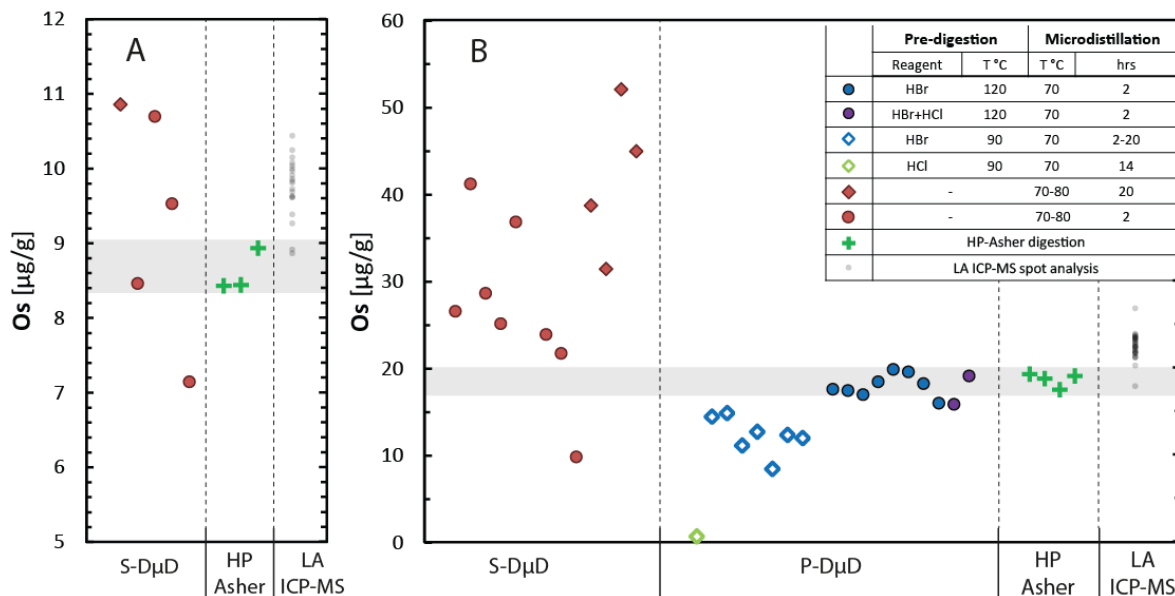


**Figure 3-2** Osmium concentration measured with different methods in BonnSulfII (A) and BonnSulfVI (B). S-D $\mu$ D are single grain tests with "Simultaneous digestion and microdistillation", i.e. the grain is digested while microdistilling the Os. P-D $\mu$ D are single grains tests with a pre-digestion step (in HBr, HCl or HBr + HCl) followed by microdistillation. The light grey field shows the concentration range obtained after HP-Asher digestions.

Single grain tests on BonnSulfVI yielded Os concentrations between 1 and 52  $\mu\text{g/g}$  (Figure 3-2B). None of the S-D $\mu$ D ( $n = 12$ ) shows Os concentrations in the range of the HP-Asher values (18-19  $\mu\text{g/g}$ ) and only one test yielded a Os concentration  $< 21 \mu\text{g/g}$  (Figure 3-2B). In S-D $\mu$ D, long micro-distillation duration (20 hours) tend to yield higher Os concentrations (average 37  $\mu\text{g/g}$ ) when compared to shorter (2 hours) micro-distillation procedures (average 27  $\mu\text{g/g}$ ). However, there is a large overlap in the Os concentrations obtained by the 2 and 20 hours micro-distillation tests (Figure 3-2). Tests with P-D $\mu$ D generally yielded lower Os concentrations (1-20  $\mu\text{g/g}$ ) when compared to S-D $\mu$ D. The lowest concentration is observed for P-D $\mu$ D in HCl where a clear solid residue was observed. If only the P-D $\mu$ D in HBr and HBr + HCl are considered, the Os concentration is limited between 9 and 20  $\mu\text{g/g}$  and two distinct ranges are observed depending on the temperature of the digestion (Figure 3-2B). The P-D $\mu$ D in HBr and HBr + HCl with a first digestion step at 120 °C yielded an Os concentration between 16 and 20  $\mu\text{g/g}$ , with an average of 18  $\mu\text{g/g}$ , which is in good agreement with the HP-Asher range (18-19  $\mu\text{g/g}$ ).

Conversely, the P-D $\mu$ D in HBr with a low digestion temperature (90 °C), show systematically lower Os concentrations ranging between 9 and 15  $\mu\text{g/g}$  (average 12  $\mu\text{g/g}$ ).

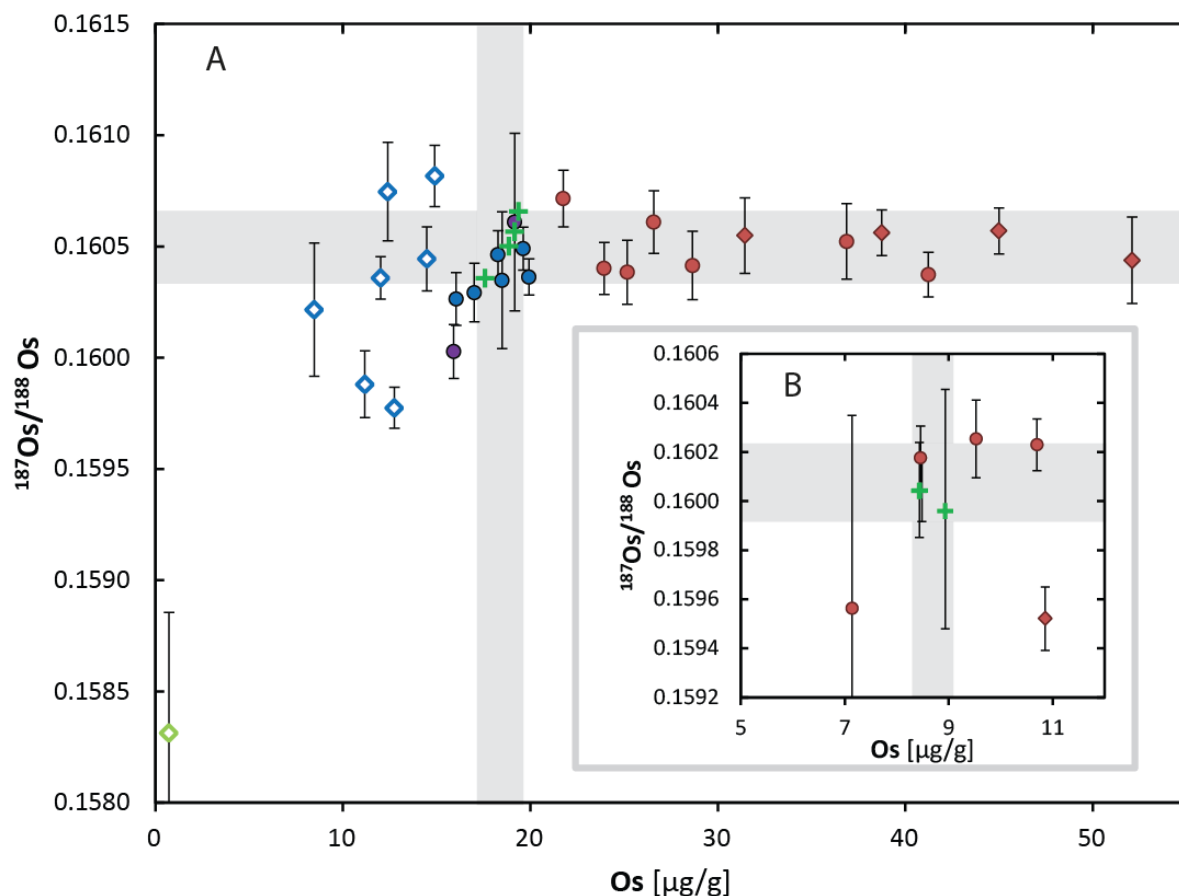


**Figure 3-3** Osmium concentration and  $^{187}\text{Os}/^{188}\text{Os}$  composition of the standard BonnSulfVI (A) and BonnSulfIII (B) obtained using different single grain analytical procedures and HP-Asher digestions. Symbols as in Figure 3-2. The light grey field represents the concentration range obtained for HP-Asher digestions. Error bars are 2 std. dev. Analytical uncertainties obtained after HP-Asher digestions are not reported for BonnSulfVI and they are  $< 0.0003$  (2 std. dev).

The average  $^{187}\text{Os}/^{188}\text{Os}$  measured in single grain tests on BonnSulfVI does not change significantly between S-D $\mu$ D and P-D $\mu$ D in HBr or HBr + HCl (Table 3-2, Figure 3-3A). The  $^{187}\text{Os}/^{188}\text{Os}$  scatter is similar in all S-D $\mu$ D and in P-D $\mu$ D for 120 °C digestion. With the exception of SGBNVI-66, in each of these test, the  $^{187}\text{Os}/^{188}\text{Os}$  overlap within the analytical error (2SD) with those obtained after HP-Asher digestions ( $0.1604 < ^{187}\text{Os}/^{188}\text{Os} < 0.1607$ ). A larger scatter is observed for P-D $\mu$ D in HBr with 90 °C digestion. In this case, only four of the seven measurements are in agreement (within 2SD of the measurements) with the

HP-Asher range and two tests yielded significantly lower  $^{187}\text{Os}/^{188}\text{Os}$  ( $< 0.1600$ ) (Figure 3-3A). The lowest  $^{187}\text{Os}/^{188}\text{Os}$  (0.1583) is observed after P-D $\mu$ D in HCl.

### ***3.3.4 Ruthenium, Pd, Re, Ir, and Pt concentrations in single grain procedures***

Only tests performed with BonnSulfVI were measured for Ru, Pd, Re, Ir, and Pt. These tests include S-D $\mu$ D and P-D $\mu$ D in HBr and HBr + HCl. The concentrations determined with S-D $\mu$ D ( $n = 8$ ) are always extremely low for Pt ( $< 1 \mu\text{g/g}$ ) and Ir (0-7  $\mu\text{g/g}$ ) (Figure 3-4A-B, Figure 3-5A). In the five P-D $\mu$ D in HBr with 90 °C digestion, Pt concentrations varies between 10 and 57  $\mu\text{g/g}$  ( $n = 5$ ), while Ir varies between 17 and 18  $\mu\text{g/g}$  ( $n = 3$ ). In these tests the concentrations of Pt are always at least 30% higher or lower than the HP-Asher range (17-18  $\mu\text{g/g}$ ) while Ir concentrations are systematically lower (10-20%) than any HP-Asher value (20-21  $\mu\text{g/g}$ ) (Figure 3-4A-B, Figure 3-5A). The results obtained using a similar digestion method (P-D $\mu$ D in HBr) but at higher temperature (120 °C) yielded concentrations between 17 and 25  $\mu\text{g/g}$  ( $n = 5$ ) for Ir and between 14 and 16 for Pt ( $n = 6$ ). Overall, these tests show average concentrations for Pt (15  $\mu\text{g/g}$ ) and Ir (20  $\mu\text{g/g}$ ) that differ for less than 20% from the ones observed after HP-Asher digestion (Figure 3-4A-B, Figure 3-5A). The four P-D $\mu$ D in HBr + HCl tests show a small variation in concentrations with respect to both Ir (20-22  $\mu\text{g/g}$ ) and Pt (16-17  $\mu\text{g/g}$ ). The latter concentrations are almost identical to the ones obtained after HP-Asher digestion as every P-D $\mu$ D in HBr + HCl yielded Pt and Ir concentrations that overlap with the HP-Asher range within a 10% difference (Figure 3-4A-B, Figure 3-5A).

In P-D $\mu$ D and S-D $\mu$ D, Pd shows a concentration range between 13 and 18  $\mu\text{g/g}$  (Figure 3-4C, Figure 3-5B-C). The smallest scatter is obtained for S-D $\mu$ D (15.9-17.2  $\mu\text{g/g}$ ,  $n=8$ ) and P-D $\mu$ D in HBr + HCl (16.5-16.9  $\mu\text{g/g}$ ,  $n=4$ ) (Figure 3-4C, Figure 3-5B-C). A larger scatter in Pd concentrations is observed for P-D $\mu$ D in HBr for both 120 °C (15.1-18  $\mu\text{g/g}$ ,  $n=6$ ) and 90 °C (13.4-16.3  $\mu\text{g/g}$ ,  $n=5$ ) digestions. With the exception of P-D $\mu$ D with 90 °C digestion, the Pd concentrations obtained with different digestion methods are in good agreement ( $< 10\%$  difference) with that inferred after HP-Asher digestions (16.0-16.4  $\mu\text{g/g}$ ).

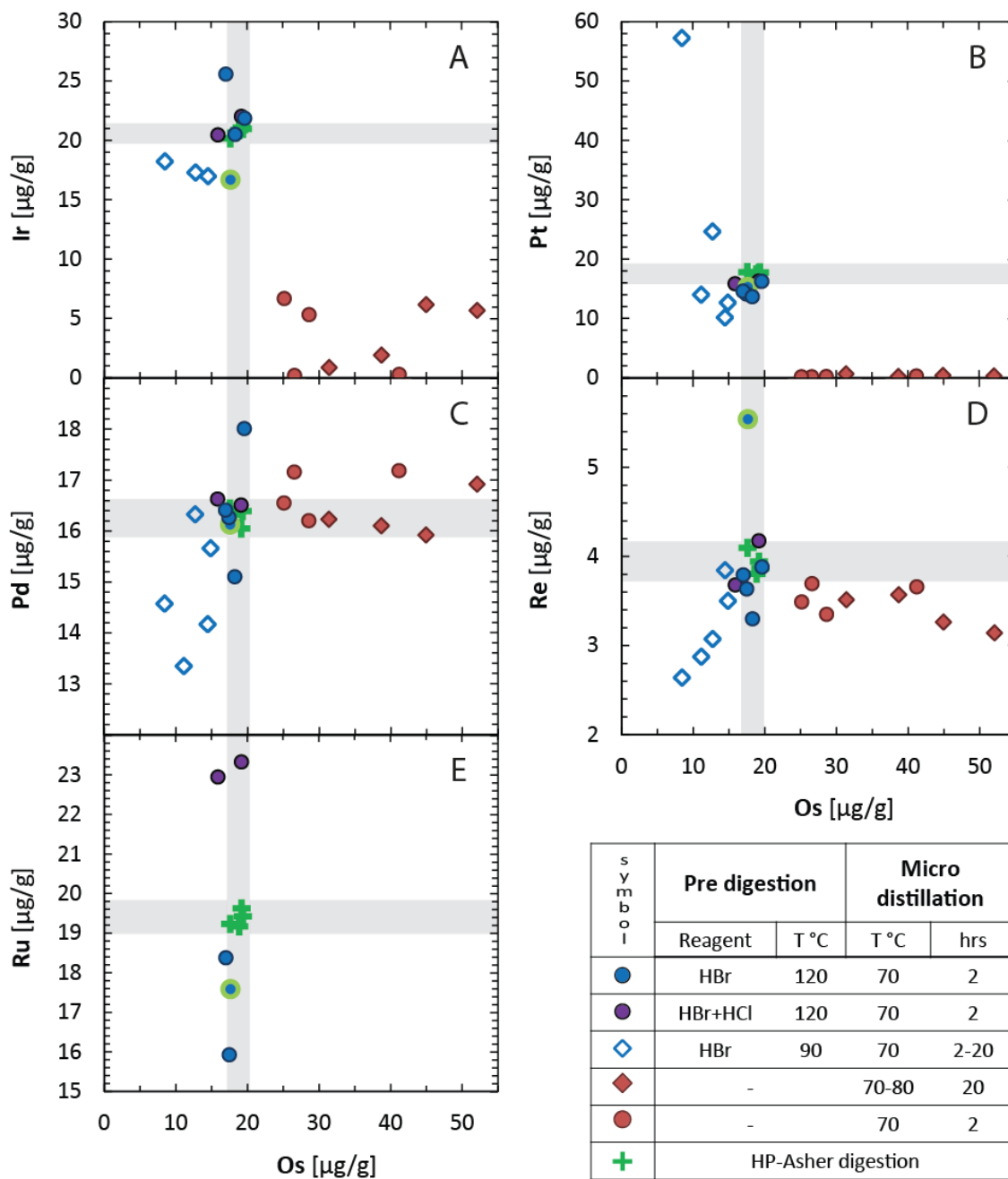


**Figure 3-4** Highly Siderophile Elements vs. Os concentrations measured in BonnSulfVI after HP-Asher digestions and single grain tests. The light grey fields represent the concentration range obtained after HP-Asher digestions. Symbols surrounded by a light green circle are tests re-dissolved in HCl after the pre-digestion (see text for explanation).

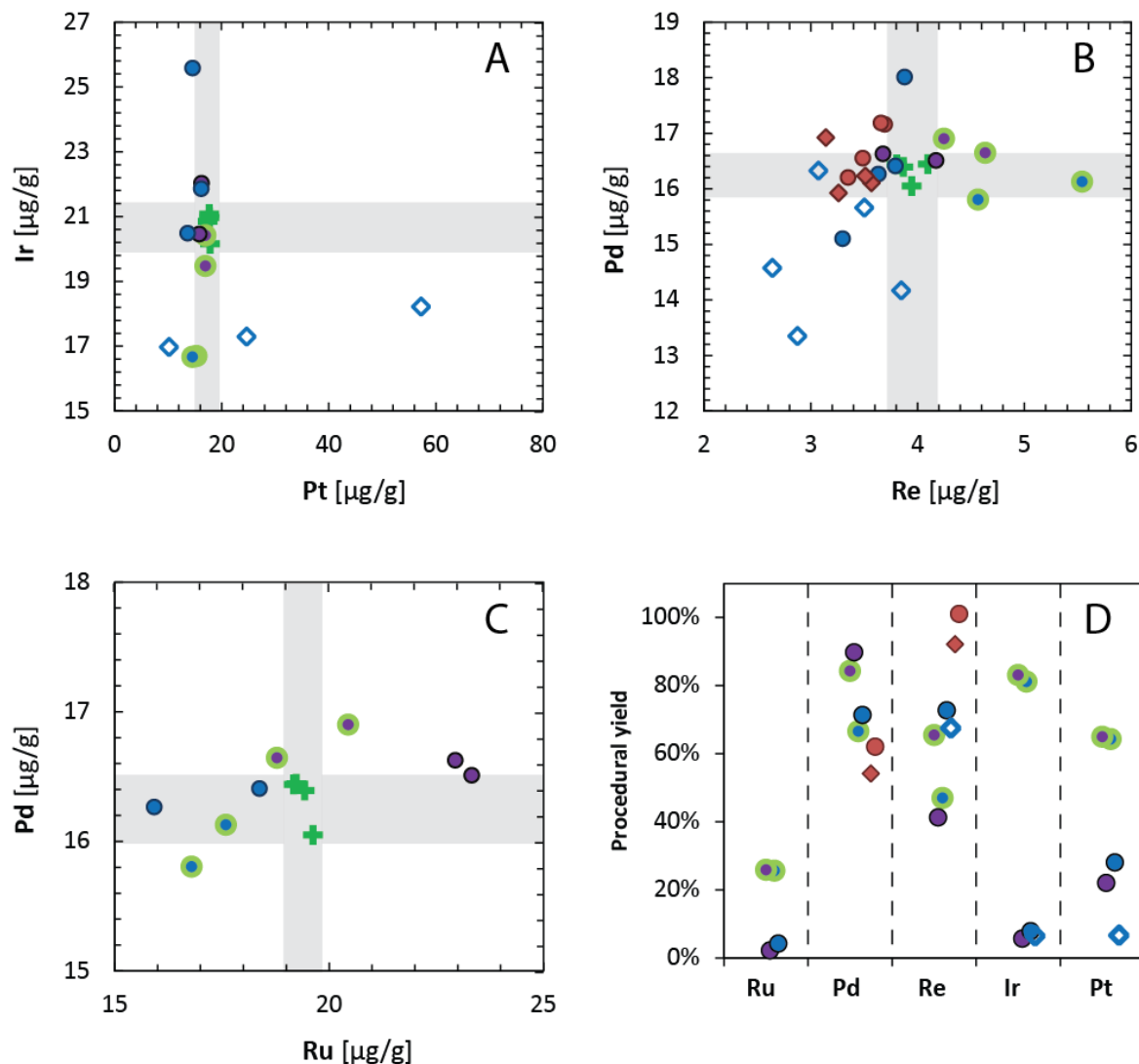


**Figure 3-5** A-C) Highly Siderophile Elements concentrations measured after HP-Asher digestions and single grain tests (BonnSulfVI). D) Highly Siderophile Elements procedural yields for different sets of single grain test. Only test performed with cation exchange resin are reported, each point is the average of at least two tests. The S-D $\mu$ D tests are not shown in (A) because out of scale. Symbols as in Figure 3-4.

Tests with S-D $\mu$ D show a Re content between 3.1 and 3.7  $\mu\text{g/g}$  ( $n = 8$ ); P-D $\mu$ D (120  $^{\circ}\text{C}$  digestions) between 3.3 and 5.5  $\mu\text{g/g}$  ( $n = 10$ ), P-D $\mu$ D (90  $^{\circ}\text{C}$  digestions) between 2.6 and 3.8  $\mu\text{g/g}$  ( $n = 5$ ) (Figure 3-4C-D, Figure 3-5B). The latter tests show a positive correlation with the Os content (Figure 3-4D). The P-D $\mu$ D in HCl + HBr show a narrower range in the Re content (3.7-4.6  $\mu\text{g/g}$ ,  $n=4$ ) when compared to tests performed at the same temperature in HBr only (3.3-5.5  $\mu\text{g/g}$ ,  $n=6$ ) (Figure 3-4C-D, Figure 3-5B). Despite the large scatter, the average Re concentrations obtained after P-D $\mu$ D with 120  $^{\circ}\text{C}$  digestion (4.1  $\mu\text{g/g}$ ) is in agreement with the Re content measured after HP-Asher digestions (3.8-4.1  $\mu\text{g/g}$ ).

Rhenium measured after S-D $\mu$ D is always lower than the HP-Asher values (Figure 3-4D, Figure 3-5B).

Only eight tests were successfully measured for Ru. In these tests, which include only P-D $\mu$ D with 120 °C digestion, Ru varies between 16 and 23  $\mu\text{g/g}$  (Figure 3-4E, Figure 3-5C) with an average of 19  $\mu\text{g/g}$ . P-D $\mu$ D in HBr + HCl yielded higher concentrations (19-23  $\mu\text{g/g}$ ) when compared to P-D $\mu$ D in HBr only (16-18  $\mu\text{g/g}$ ). The concentrations measured after HP-Asher digestion range between 19.2 and 19.6, overlapping with the range of P-D $\mu$ D in HBr + HCl (Figure 3-4E, Figure 3-5C).

Overall, no significant difference is observed using cation or anion exchange chemistry. The only exception is the Ir concentration after S-D $\mu$ D, which is at least a factor of two higher in all the cation-based tests when compared to the anion-based ones (Table 3-3).

## 3.4 DISCUSSION

### 3.4.1 Osmium concentrations and $^{187}\text{Os}/^{188}\text{Os}$ in single grain procedures

#### 3.4.1.1 Osmium concentrations: incomplete sulfide digestion and spike loss

Osmium concentrations show a large variation depending on the used analytical technique, and only few tests yielded concentrations in agreement with those determined after HP-Asher digestion. The different concentrations will be interpreted here in terms of spike loss and/or incomplete sulfide digestion.

The four tests performed on BonnSulfII (Table 3-3, Figure 3-2A, Figure 3-3B) show that the Os concentrations obtained with S-D $\mu$ D are usually significantly higher (three tests) or lower (one test) when compared to those obtained after HP-Asher digestions. The only test that yielded a Os concentration of 8.5  $\mu\text{g/g}$ , i.e. in agreement with the HP-Asher range (8.4-8.9  $\mu\text{g/g}$ ) is not reproduced by the test that was run at the same conditions (2 hours and 80 °C micro-distillation), which resulted in an Os content of 10.7  $\mu\text{g/g}$ . The tests on BonnSulfII show that changes in temperature and in the duration of the micro-distillation does not have a direct effect on the determined Os concentration, which often

differs from the ones obtained after HP-Asher digestions (up to 30%). Tests on BonnSulfVI were thus performed with the micro-distillation temperature fixed at 70 °C (except SGBNVI-1). Hereafter, only the results from BonnSulfVI, which also includes Ru, Pd, Re, Ir and Pt concentrations for both P-D $\mu$ D and S-D $\mu$ D, are discussed.

The majority of S-D $\mu$ D tests in BonnSulfVI yielded Os concentrations higher than those obtained after HP-Asher digestion (Table 3-3, Figure 3-2B). This can be explained by spike loss during the evaporation of the spike solution on the beaker lid (step 2S in Figure 3-1), or by incomplete re-dissolution of the spike during micro-distillation (steps 4 and 5 in Figure 3-1). The highest Os concentrations are observed for small grains (Table 3-3); hence the fraction of spike lost was larger for small grains. This argues against an incomplete re-dissolution after evaporation because small amount of spike are likely easier dissolved.

Regarding the P-D $\mu$ D tests, it is clear that the HCl does not fully dissolve the sulfide as shown by the presence of a solid residue after digestion. The use of HBr or HBr + HCl for P-D $\mu$ D tests resulted in the absence of any solid residue. However, P-D $\mu$ D in HBr with 90 °C digestion yielded Os concentrations between 8 and 15  $\mu$ g/g, which are systematically lower than those determined after HP-Asher digestion (18-19  $\mu$ g/g), and thus suggesting that portions of the sulfide fragments were not fully dissolved. Given that a rough inverse correlation is observed between the Os concentrations and the size of the original fragments for P-D $\mu$ D in HBr with 90 °C digestion (Table 3-3), it is likely that the kinetic of the dissolution process is relatively slow at 90 °C and not sufficient to fully digest sulfides in two days. The fact that no solid residue was clearly visible after the digestion is probably due to the very small size of the analyzed material (18-46  $\mu$ g). In fact, a partial dissolution would likely result in particles that are too small to be detected with naked eye. The average Os concentration obtained after P-D $\mu$ D with 120 °C digestion (18  $\mu$ g/g) is in very good agreement with the one determined after HP-Asher digestion (18-19  $\mu$ g/g). The small scatter in Os concentrations shown by these tests (16-20  $\mu$ g/g) is similar to the variation observed between LA-ICP-MS spot analyses (2SD = 3  $\mu$ g/g) and might reflect small scale heterogeneities in the analyzed material. This indicates that digestions carried out in HBr or HBr + HCl at high temperature (120° C) are well suited for the dissolution of sulfide fragments and allow accurate determination of Os concentrations in BMS.

In order to test if HBr and HBr + HCl are also able to successfully dissolve natural BMS with variable composition, relatively large fragments (a few mg) of pentlandite, pyrrhotite, chalcopyrite, and pyrite were placed into 3 mL of HBr and HBr + HCl. No solid residue was observed in the beaker containing pentlandite, pyrrhotite, and chalcopyrite after one day at 120 °C, while the pyrite fragment was clearly undissolved in both HBr and HBr + HCl. Because of the large size of the initial fragments, the lack of visible residue of pentlandite, pyrrhotite, and chalcopyrite, suggests that many natural BMS are quickly digested by HBr and HBr + HCl at 120 °C.

#### 3.4.1.2 Variations from $^{187}\text{Os}/^{188}\text{Os}$ obtained after HP-Asher digestion

Overall the measured Os isotopic compositions determined after S-D $\mu$ D, P-D $\mu$ D with 120 °C digestion and HP-Asher are in good agreement (Figure 3-3A). In contrast, the P-D $\mu$ D in HCl and three tests of P-D $\mu$ D in HBr with 90 °C digestion show anomalous  $^{187}\text{Os}/^{188}\text{Os}$  as they plot outside the range defined by HP-Asher digestions. As previously discussed, these tests were affected by incomplete digestion of the sulfide fragments. Poorly digested samples might yield anomalous  $^{187}\text{Os}/^{188}\text{Os}$  if the starting material has a heterogeneous isotopic composition. Because no significant variation is observed in the Os isotopic composition of other tests, an isotopic heterogeneity is only possible at the very small scale ( $\mu\text{m}$  or sub  $\mu\text{m}$  level). In this scenario, the analyzed material can be assumed to consist of two components with different isotopic composition and Os concentration. Thus, a linear correlation would be expected in a  $^{187}\text{Os}/^{188}\text{Os}$  vs.  $1/\text{Os}$  plot as the result of a binary mixing of two components. This is not observed in Figure 3-6A-B, arguing against a heterogeneous  $^{187}\text{Os}/^{188}\text{Os}$  composition of the synthesized sulfide.

Tests with anomalous  $^{187}\text{Os}/^{188}\text{Os}$  are the only ones that yielded  $^{189}\text{Os}/^{188}\text{Os}$  more than 1% lower than the natural value of 0.12197 (Luguet et al., 2008) (Figure 3-6C). Since these tests show the lowest Os concentrations, they are characterized by high spike/sample ratio. In fact, all the tests were spiked depending on the weight, assuming an Os concentration of 18  $\mu\text{g}/\text{g}$  and aiming for  $^{190}\text{Os}/^{192}\text{Os}$  of 2.5. Therefore, the tests yielding Os concentrations lower than 18  $\mu\text{g}/\text{g}$  were “overspiked” ( $^{190}\text{Os}/^{192}\text{Os}$  up to 4.4). In the process of data reduction (e.g. spike deconvolution, oxygen correction and mass bias correction), overspiked measurements are more affected by uncertainties (e.g. on the measured

$^{190}\text{Os}/^{188}\text{Os}$  and on the spike composition) that are usually not considered. Disregarding these uncertainties can potentially lead to overestimate the precision of critically “overspiked” samples and possibly explain the apparent poor accuracy. In order to test this hypothesis, a Monte Carlo simulation was carried out in few samples to fully propagate the uncertainties. All the uncertainties on the measured ratios were included (i.e. on  $^{185}\text{Os}/^{188}\text{Os}$ ,  $^{186}\text{Os}/^{188}\text{Os}$ ,  $^{187}\text{Os}/^{188}\text{Os}$ ,  $^{189}\text{Os}/^{188}\text{Os}$ ,  $^{190}\text{Os}/^{188}\text{Os}$ ,  $^{192}\text{Os}/^{188}\text{Os}$ ) as well as on spike and sample weighing (2SD of 0.1 mg and 1  $\mu\text{g}$  respectively). The uncertainty on the spike composition was assumed to be 1% (2SD) on each isotope normalized to  $^{188}\text{Os}$  (e.g. on  $^{187}\text{Os}/^{188}\text{Os}$ ). When all these deliberately overestimated uncertainties are considered, the increase on the 2SD associated with  $^{187}\text{Os}/^{188}\text{Os}$  measurements is larger for overspiked tests (e.g. 2SD on SGBNVI-16 and SGBNVI-17 are 195  $\mu\text{g}/\text{g}$  and 135  $\mu\text{g}/\text{g}$  respectively, while unpropagated 2SD are 150 and 92  $\mu\text{g}/\text{g}$  respectively) than for underspiked tests (e.g. 2SD on SGBNVI-28 is 155  $\mu\text{g}/\text{g}$  while the unpropagated 2SD is 141  $\mu\text{g}/\text{g}$ ). However, the small effect on 2SD is not sufficient to justify the poor reproducibility of overspiked tests.

In conclusion, at this stage it is not possible to give a clear explanation of the unexpected  $^{187}\text{Os}/^{188}\text{Os}$  measured in some of the tests that yielded the lowest Os concentrations. However, the data depicted here show that measurements are critical when, using a  $^{190}\text{Os}$  spike, the measured  $^{190}\text{Os}/^{188}\text{Os}$  is higher than 10. Moreover, it is shown that non accurate  $^{187}\text{Os}/^{188}\text{Os}$  measurements yield  $^{189}\text{Os}/^{188}\text{Os}$  that differs for more than 1% from the natural value. Therefore this ratio can be used (when not adopted for corrections) as a monitor for critical conditions.

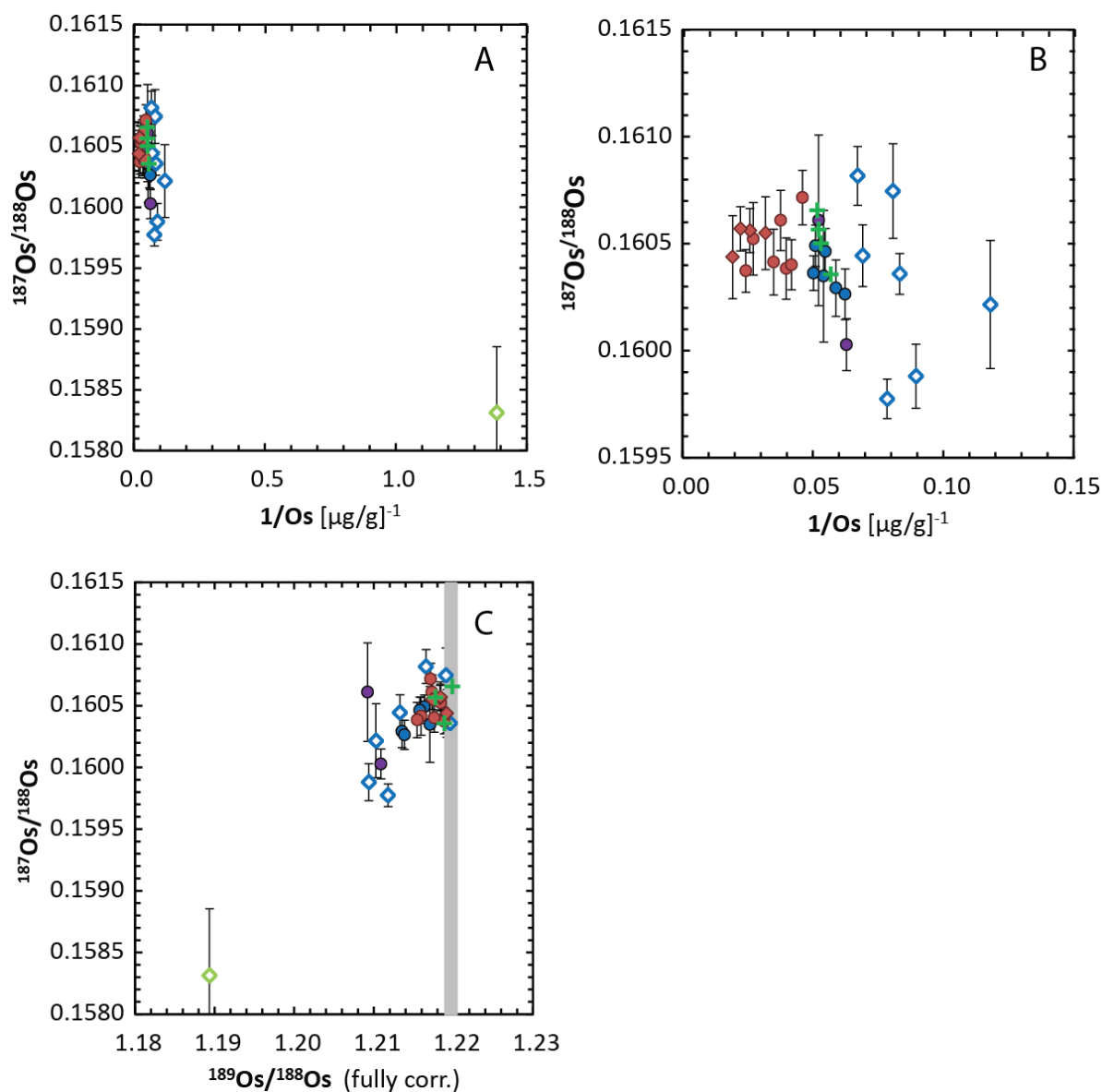


**Figure 3-6** A) and B)  $^{187}\text{Os}/^{188}\text{Os}$  vs.  $1/\text{Os}$  showing that there is no linear correlation. This argues against a  $^{187}\text{Os}/^{188}\text{Os}$  variation due to the mixing of two different components. C)  $^{187}\text{Os}/^{188}\text{Os}$  vs.  $^{189}\text{Os}/^{188}\text{Os}$  for HP-Asher digestions and single grain tests in BonnSulfVI. Both isotopic ratios are fully corrected for oxides interferences, mass bias and spike contribution. One analysis after HP-Asher digestion is not reported due to anomalous behavior of the  $^{189}\text{Os}$  signal during the N-TIMS measurement. The grey area represents the natural isotopic ratio reported by Luguët et al. (2008). Symbols as in Figure 3-2.

### ***3.4.2 Ruthenium, Pd, Re, Ir, and Pt concentrations in single grain procedures***

#### ***3.4.2.1 Palladium and Re concentrations***

Both S-D $\mu$ D and P-D $\mu$ D with 120 °C digestion yielded Pd concentrations that always agree within 10% with the HP-Asher values (Figure 3-4C, Figure 3-5B-C). This proves that the BMS were fully digested and that the two techniques provide reliable Pd concentrations. Furthermore, the overall good reproducibility of Pd concentrations implies that the spike loss observed for Os in S-D $\mu$ D does not necessarily affect the other HSE. The P-D $\mu$ D with 90 °C digestion comprise the only group of tests that result in almost systematic lower Pd and Re concentrations when compared to those obtained after HP-Asher digestions (Figure 3-4C-D, Figure 3-5B). As mentioned before, low HSE concentrations could result from an incomplete digestion of the fragments at 90 °C. The correlation between Re and Os in these tests seems to confirm this possibility. At this stage, it is difficult to explain the scatter observed in Re concentrations obtained with P-D $\mu$ D with 120 °C digestion (i.e. between 3.3 and 5.5  $\mu$ g/g, 2SD = 1.2  $\mu$ g/g) because Re does not correlate with any other HSE concentrations. A possible explanation might be the heterogeneity of the starting material because Re shows the largest relative variability in LA-ICP-MS measurements (2SD = 0.8  $\mu$ g/g, Table 3-2). It is worth to note that the average Re concentrations obtained with P-D $\mu$ D with 120 °C is 4.1  $\mu$ g/g and that it is in good agreement with the values obtained after HP-Asher digestions (3.9-4.1  $\mu$ g/g). This indicates that this technique provides accurate Re concentrations. In contrast, every test performed with S-D $\mu$ D yielded Re concentrations (3.1-3.7  $\mu$ g/g) that are systematically lower than the range defined by HP-Asher digestions, attesting the inaccuracy of this technique for Re concentrations.

#### ***3.4.2.2 Implications for Re-Os geochronology***

For Re-Os geochronology it is important to note that S-D $\mu$ D yielded concentrations that are slightly lower for Re (about 10%) and much higher for Os (up to more than 250%) when compared to the expected values. This leads to an underestimation of the Re/Os ratio of a given sample, and will therefore affect Re-Os model ages. In particular, any Re-decay corrected age (e.g.  $T_{MA}$ ) will result in artificially younger ages. The use of S-D $\mu$ D for Re-

Os dating would also hamper the investigation of any preserved isochron. According to these considerations it is somehow surprising that Westerlund et al. (2006) reported an isochron after analyzing BMS inclusions with the S-D $\mu$ D procedure. Moreover, in the pioneer study of Pearson et al. (1998), where four fragments of the same BMS inclusion were analyzed, it was shown that none of the three S-D $\mu$ D replicates yielded Os concentrations higher than the replicate obtained after Carius tube digestion. Since the data of Westerlund et al. (2006) and Pearson et al. (1998) were obtained in the same laboratory (DTM, Carnegie Institution of Washington, USA) it is possible that these authors used some measures in the S-D $\mu$ D procedure that improved the accuracy of their data when compared to the tests performed in the present study. However, it is important to stress that the S-D $\mu$ D tests performed on BonnSulfII and BonnSulfVI followed strictly the procedure described by Pearson et al. (1998) and that they clearly failed in reproducing the concentrations obtained after HP-Asher digestion. This leads to suggest extreme caution in using the S-D $\mu$ D procedure at least as far as details about the method are not available to solve any possible analytical issue (e.g. on spike loss) and the accuracy of the procedure is fully attested. From what discussed before, these issues can be successfully overcome by the use of P-D $\mu$ D with 120 °C digestion, which was shown to provide more accurate Re and Os concentrations and is more likely to yield realistic age information.

#### 3.4.2.3 *Platinum and Ir concentrations: the effect of PGM?*

Surprisingly, S-D $\mu$ D leads to extremely low Pt and Ir concentrations (Figure 3-4A-B, Figure 3-5A). Reasons for that are difficult to address because the sulfides were fully digested as shown by the good recovery of Pd. One possibility is that the spike and the sample do not fully equilibrate during the  $\text{H}_2\text{SO}_4\text{-Cr}^{6+}$  digestion. In this scenario Ir and Pt would be released from the sulfide but, in spite of equilibrating with the spike, they would form insoluble compounds. A second possibility is that Pt and Ir are not located in the crystal lattice of the synthetic sulfide and are controlled by other nano-phases that are not digested in  $\text{H}_2\text{SO}_4\text{-Cr}^{6+}$ . The formation of nano-phases carrying HSE (i.e. PGM) is common in sulfides and they can also occur in HSE-unsaturated media (Helmy et al., 2013). If this is the case, the PGM controlling Pt and Ir should be homogeneously distributed in the synthetic material and should be extremely small (< 100 nm) as they are not detectable in backscattered electron images (electron microprobe) and laser ablation spectra. According

to this, one might speculate that the low Re concentration observed after S-D $\mu$ D (about 10% lower than what observed after HP-Asher digestion) might be due to the fact that about 10% of Re is controlled by PGM. The occurrence of PGM seems to do not affect the tests performed with a pre-digestion step in HBr and HBr + HCl because these tests show Pt and Ir concentrations always higher than 10  $\mu$ g/g. As it is not clear if the PGM were present as nano-phases in the starting material or they formed during the sulfide digestion in H<sub>2</sub>SO<sub>4</sub>, it is difficult to assess if HBr and HBr + HCl are able to dissolve such phases or if their formation is hampered by the pre-digestion step. However, both possibilities are not surprisingly since Pt and Ir show a high affinity for anionic chloride and bromide complexes (e.g. Cotton, 1997). Regardless the presence of Pt- and Ir-bearing PGM, tests with P-D $\mu$ D in HBr + HCl yielded Ir and Pt concentrations that always overlap with the range defined by HP-Asher digestions within 10%. Therefore, this technique seems to provide the most accurate Pt and Ir concentrations for the analyses of BMS. The large scatter in Pt and Ir concentrations observed after P-D $\mu$ D in HBr with digestion at 90 and 120 °C is difficult to explain since it is not observed for other HSE.

#### *3.4.2.4 Ion exchange resins and procedural yield*

Both types of exchange resin, cation and anion, give reliable and similar results with similar efficiency in removing interferences (Hf, Y, Zr, Mo), which in this case were most likely introduced via the reagents. The main difference resides in the yield of the columns (Figure 3-5D). An estimation of the full procedure yield was qualitatively determined by comparing the counts of each measurement with the expected ones. The expected count rates were calculated considering the dilution of the measured solution and the daily sensitivity of the ICP-MS. A yield  $\geq$  40% is achieved with both resins for Re and Pd. However, with anion separation, very poor yields ( $\leq$  1%) are obtained for Pt and Ir. Conversely, when cation exchange resins are used, the yield is always  $>$  10% for both elements. The tests that included two steps of cation exchange separation show similar yields when compared to the tests with only one step, attesting the overall good yield of the resin. When only one separation step was made, it was not possible to measure Ru as the <sup>101</sup>Ru/<sup>99</sup>Ru ratio increased during the measurement. This most likely results from polyatomic Cr-based interferences on <sup>101</sup>Ru (Dale et al., 2012; Wittig et al., 2010). In fact, a green residue, likely Cr-rich, was observed to form after evaporating the samples, while it

was not observed after a second step of cation exchange separation. A significant improvement of the Ru, Pt, and Ir yields is observed when the tests are re-dissolved in HCl after the pre-digestion. In this case the yield is always > 60% for Pd, Ir and Pt, > 40% for Re, and > 20% for Ru. The improvement of the procedural yield is particularly pronounced for Pt, Ir, and Ru (between 2 and 10 times) and likely results from a better recovery of these elements during the transfer of the pre-digested aliquot to the micro-distillation beaker. This would suggest that Pt, Ir, and Ru are not easy to dissolve in  $\text{H}_2\text{SO}_4$  so that, in the absence of a second pre-digestion step, they are mostly left behind in the 5 ml beaker. Ruthenium can be volatile during the micro-distillation process (Becker et al., 2002; Chu et al., 2014), which might explain the general low procedural yield of Ru (always < 30%).

Due to the high yields and the ability of reproducing HP-Asher concentrations, the P-D $\mu$ D in HBr + HCl with a second digestion step in HCl and two passes into cation exchange resin allows the accurate determination of  $^{187}\text{Os}/^{188}\text{Os}$  and HSE concentrations in natural single grain BMS.

### **3.5 CONCLUDING REMARKS AND PROPOSED PROTOCOL**

Two sulfides with major element compositions similar to that of natural BMS were synthesized and doped with HSE. LA-ICP-MS analyses on the two materials show a homogenous HSE content at the scale of tens of microns. The HSE concentrations and the Os isotopic composition were determined by isotope dilution after HP-Asher digestion HSE concentrations are between 1.5  $\mu\text{g/g}$  (Re) and 11.1  $\mu\text{g/g}$  (Ir) in BonnSulfII and between 3.9  $\mu\text{g/g}$  (Re) and 20.8  $\mu\text{g/g}$  (Ir) in BonnSulfVI. The HSE concentrations of the two sulfides resemble those of typical mantle BMS (e.g. Alard et al., 2000; Aulbach et al., 2004). Therefore, both the elemental composition and the homogeneous distribution of HSE in the two synthesized sulfides, makes them perfectly suitable as standard materials for the determination of  $^{187}\text{Os}/^{188}\text{Os}$  and HSE contents in natural BMS.

A novel analytical technique that allows the determination of the HSE content along with  $^{187}\text{Os}/^{188}\text{Os}$  in BMS was set up (Figure 3-7). In order to fully dissolve sulfides and to ensure full sample/spike equilibration (i.e. no spike loss and full BMS digestion) the

technique of Pearson et al. (1998) was modified by adding a pre-digestion step. In the procedure proposed here (Figure 3-7), the BMS is first digested in an HBr-HCl mixture (0.4 mL concentrated HBr + 0.4 mL concentrated HCl + 0.2 mL H<sub>2</sub>O-MQ) along with a multi-element HSE spike solution at 120 °C for two days with two intermediate steps of ultrasonication. The solution is then evaporated at 70 °C, re-dissolved in 0.5 mL 8 M HCl, and re-evaporated on the lid of a conical vial. The residue is dissolved in H<sub>2</sub>SO<sub>4</sub> and micro-distilled to separate the Os fraction. Afterwards, the H<sub>2</sub>SO<sub>4</sub>-based solution is then treated with BaCl<sub>2</sub> and H<sub>2</sub>O<sub>2</sub> to separate SO<sup>4-</sup> and Cr<sup>6+</sup> by centrifugation and to reduce the remnant Cr<sup>6+</sup> to Cr<sup>3+</sup>. The HSE are separated using two steps of cation exchange columns before being analyzed with SF-ICP-MS. The Os isotopic and elemental composition is measured with N-TIMS.

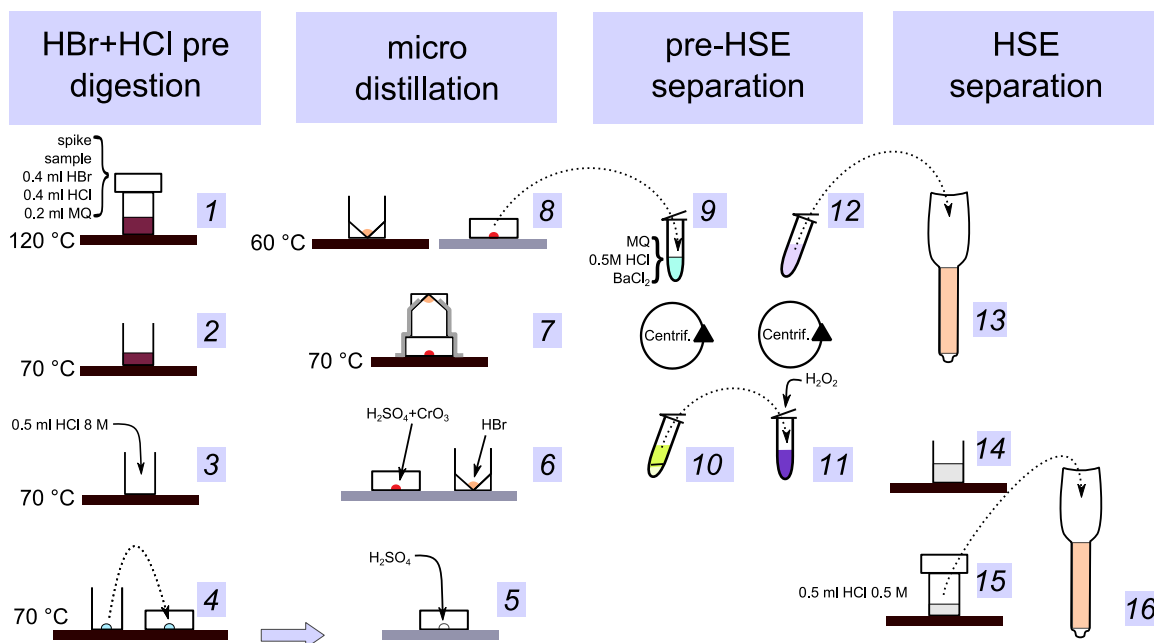


**Figure 3-7** Flowchart describing the procedure proposed for analyzing Os isotopic composition and HSE concentrations in single grain sulfides.

The accuracy of this technique was estimated by comparing the concentrations with those obtained after HP-Asher digestion on the same sulfide material. Accuracy is better than 90% for Pd, Os, and Ir concentrations, and better than 80% for Ru, Re, and Pt concentrations. Within the analytical precision of the measurements (typical 2SD = 0.01%),

the Os isotopic composition is also consistent with the one obtained after HP-Asher digestions. A well-known critical condition for accurate  $^{187}\text{Os}/^{188}\text{Os}$  measurements is represented by the sample/spike solution ratio. In this study, where a  $^{190}\text{Os}$ -enriched spike was used, a reasonable limit for accurate measurements is obtained when the measured  $^{190}\text{Os}/^{188}\text{Os}$  is  $< 10$ .



## Chapter 4:

# SUMMARY, CONCLUSIONS AND FUTURE WORK

This work provides information and tools to investigate processes affecting the  $^{187}\text{Re}$ - $^{187}\text{Os}$  decay system and the highly siderophile elements (HSE - Ru, Rh, Pd, Re, Os, Ir, Pt, and Au) in the sub-continental lithospheric mantle (SCLM). This aim was achieved by the investigation of single base metal sulfides (BMS) in natural samples (Chapter 2) and the development of an improved analytical method for further studies (Chapter 3).

Mantle xenoliths from Somerset Island show a complex record of geological processes, which include high degrees of partial melting, mantle metasomatism, interaction with the kimberlite magma and serpentinization. The two analyzed samples with the most overprinted HSE signature (i.e. supra-chondritic Pd/Pt) show evidence of sulfide metasomatism as indicated by the high sulfide modal abundance, the occurrence of large interstitial BMS grains and the extremely variable  $^{187}\text{Os}/^{188}\text{Os}$  recorded in individual BMS grains ( $^{187}\text{Os}/^{188}\text{Os} = 0.172\text{-}0.108$ ). The whole rock Os budget of these two samples is controlled by different populations of BMS grains. As a result, the whole rock  $T_{\text{RD}}$  age of one sample predates the first Re-depletion event for more than 500 Ma. This confirms that whole Re-Os model ages is of limited value in samples with metasomatic HSE signature and it should be used with caution (e.g. Luguet et al., 2015; Pearson et al., 2004; Wainwright et al., 2015).

The kimberlite magmatism strongly affected many mantle xenoliths from Somerset Island. It is shown here that the interaction with the kimberlite can lead to a large enrichment in Re along with the formation of djferfisherite and the crystallization of clinopyroxene at the expense of orthopyroxene. Djferfisherite is the most abundant sulfide formed during the kimberlite infiltration and it occurs in fractures or as overgrowth coronae around older Fe-Ni sulfides. The Os isotopic composition of djferfisherite is extremely radiogenic ( $^{187}\text{Os}/^{188}\text{Os} > 0.172$ ) while portions of older BMS surrounded by djferfisherite show unradiogenic Os ( $^{187}\text{Os}/^{188}\text{Os} = 0.109$ ). This suggests that, even in extremely

metasomatized peridotites, pristine portions of BMS can preserve the original pre-metasomatism Os isotopic signature.

During serpentinization, the replacement of pentlandite by heazlewoodite can trigger exsolutions of PGM (Ir, Ru, Pt-rich). These submicron phases are observed along the interface between the two sulfide phases, suggesting that during the pentlandite-heazlewoodite reaction they might grow and coalesce to form larger grains. The formation of PGM does not seem to affect the mobility of HSE as indicated by the residual pattern of the hosting xenolith.

Single BMS grains from samples with overprinted HSE signature yielded  $T_{RD}$  ages that are as old as 2.8 Ga, in agreement with  $T_{RD}$  ages (BMS and whole rock) recorded in the most residual sample. This leads to conclude that single BMS grain investigations can overcome the issue observed on the whole rock scale to successfully date melting events in samples with an overprinted HSE signature. Single BMS grains with  $T_{RD}$  ages of 2.7-2.8 Ga were recovered from three samples over a total of four analyzed xenoliths. This suggests a large-scale event of SCLM formation in the north portion of the Rae craton, which might be associated with the emplacement of the local greenstone belts in a continental rift setting. A similar scenario was also proposed for the nearby Slave Craton, attesting a similar Neoproterozoic evolution for the two cratons (Heaman and Pearson, 2010; Pehrsson et al., 2013).

The  $T_{RD}$  ages obtained from BMS grains in different samples are clearly grouped in three time ranges of ~1.9, ~2.2 and 2.7-2.8 Ga. In a speculative scenario, the ~1.9 and ~2.2 Ga  $T_{RD}$  ages can be reconciled with the geodynamic evolution of the Canadian Shield. At ~2.2 Ga, following extensive rifting, a new ocean formed between the Slave and the Rae craton (Halls, 2014). This process required large partial melting of the asthenospheric mantle. It is thus possible that part of melt percolated through the already depleted SCLM mantle, leaving behind metasomatic BMS. At 1.9-2.0 Ga, after the ending of the rifting, the Slave and the Rae craton converged again, consuming the oceanic crust in an eastward subduction (Hoffman, 1989). As a consequence, it is likely that a mantle wedge formed beneath Somerset Island and that part of it experienced partial melting. Some of the rising magma could have impregnated the SCLM, crystallizing a second generation of

metasomatic BMS. This scenario implies that the two Paleoproterozoic melting processes occurred in a mantle with a primitive-like composition and that the Os isotopic composition of the melts was not affected by the migration through the mantle. Moreover, the role of Re decay after the melting events is assumed to be negligible. With the awareness that further investigations are required to confirm the proposed interpretation, the former considerations highlight the potentialities of single grain Re-Os investigations to study a large variety of mantle events.

In order to provide new tools to exploit the abilities of single grain Re-Os investigations, in Chapter 3 a new analytical method is proposed to measure the Os isotopic composition and the HSE concentrations from single sulfide grains ( $\mu\text{g}$ -scale) by isotope dilution. This method was developed and its accuracy established by performing tests on fragments of two sulfide standards that were synthesized specifically for that purpose. The proposed protocol consists of a first pre-digestion step where a spike solution and the sulfide grain are dissolved in HBr and HCl. Afterwards the solution is evaporated and micro-distilled to collect the Os fraction, which is then measured by N-TIMS. The residue of the micro-distillation is processed with  $\text{BaCl}_2$  and  $\text{H}_2\text{O}_2$  to remove  $\text{H}_2\text{SO}_4$  and  $\text{Cr}^{6+}$ , which can cause interferences during mass spectrometry measurements. The HSE are then separated with cation-based exchange chemistry and measured with SF-ICP-MS. Large fragments of the two analyzed sulfides were independently characterized by isotope dilution and HP-Asher digestion. The concentrations obtained with the two methods differ  $< 10\%$  for Pd, Os and Ir and  $< 20\%$  for Ru, Re and Pt. The total procedural yield is  $> 60\%$  for Pd, Ir and Pt,  $> 40\%$  for Re, and  $> 20\%$  for Ru. The Os isotopic compositions measured with the two techniques are identical within the analytical precision of the measurements (2SD  $\sim 0.1\%$ ). Conversely, tests that were performed following the protocol proposed in the literature for Re-Os geochronology (Pearson et al., 1998) yielded inaccurate concentrations.

The proposed analytical procedure can be combined with the technique developed in Chapter 2 to extract single sulfide grains from thin sections. By this, it is possible to perform in-situ textural and mineralogical investigations before extracting and analyzing the grain of interest for its Os isotopic composition and HSE concentrations. When

compared to LA-ICP-MS analyses, this approach has the advantage to provide HSE concentrations and  $^{187}\text{Os}/^{188}\text{Os}$  from the whole sulfide grain. Moreover, analytical issues encountered with LA-ICP-MS analyses like, polyatomic interference of  $^{187}\text{Re}$  on  $^{187}\text{Os}$  and matrix-dependent effects can be overcome.

Investigations on the mineral-scale provide supplementary information when compared to whole rock analyses and thus help us to understand and infer metasomatic and magmatic processes within the Earth's mantle. Therefore, this method can be used to characterize sulfides from the lithospheric mantle, to better constrain its origin and age, but it is also open to other applications. Ultra-deep mantle xenoliths (Haggerty and Sautter, 1990) could represent a promising target for this method since these samples might provide the opportunity to trace asthenospheric processes, like deep subduction. As a further application, investigations on sulfides from different crustal lithologies, as for example, differentiated magmas can be used to constrain the behavior of HSE during differentiation processes (cf. Liu and Brenan, 2015). Altogether, this method yields the opportunity to study a number of processes with the advantage of enhanced spatial resolution and optical control of the material under investigation, in combination with accurate and precise concentration and isotope data.

# Appendix A

**Table A-1** Whole rock Re–Os Isotopic data for Somerset Island peridotites (Irvine et al., 2003).

sample name	$^{187}\text{Os}/^{188}\text{Os}$	±	$^{187}\text{Re}/^{188}\text{Os}$	±	$T_{\text{MA}}$ (Ma)	±	$T_{\text{RD}}$ (Ma)	±	$T_{\text{RD eruption}}$ (Ma)	±
K11A16	0.11227	0.00010	0.0506	0.0036	2645	28	2343	13	2354	13
K13A3	0.11100	0.00013	0.0317	0.0022	2704	24	2511	17	2518	17
K13B4	0.10940	0.00012	0.0180	0.0013	2837	19	2723	16	2727	16
X07	0.10973	0.00012	0.0534	0.0038	3045	35	2679	16	2691	16
K13A1	0.11113	0.00012	0.1438	0.0102	3688	131	2494	16	2526	16
K15A4	0.11871	0.00010	6.2511	0.4420	-		1483	13	2869	191
JP2X2	0.11150	0.00011	0.0343	0.0024	2650	23	2445	15	2453	15
JP3X1	0.11135	0.00027	1.4213	0.1005	-		2465	36	2778	56
JPN11	0.11487	0.00014	0.0574	0.0041	2295	33	1998	19	2010	19
JPS1	0.11092	0.00009	1.3058	0.0923	-		2522	12	2809	42
K11A14	0.11291	0.00009	0.0347	0.0025	2450	20	2258	12	2266	12
K11A15	0.11431	0.00014	0.0526	0.0037	2351	31	2072	19	2084	19
K11A17	0.11157	0.00016	0.0384	0.0027	2667	30	2436	21	2445	21
K11A18	0.11493	0.00015	0.1051	0.0074	2609	64	1990	20	2013	20
K12A1	0.11460	0.00015	0.0732	0.0052	2436	42	2034	20	2050	20
K13A4	0.11955	0.00018	0.0866	0.0061	1706	42	1370	24	1390	24
N2B	0.11348	0.00016	0.1153	0.0082	2950	80	2183	21	2208	22
JP1X2	0.11339	0.00012	0.1567	0.0111	3395	137	2195	16	2229	17
JP3X	0.11388	0.00010	0.0852	0.0060	2636	48	2129	13	2148	14
JPN2	0.11086	0.00012	0.0569	0.0040	2901	36	2530	16	2543	16
JPN3A	0.11274	0.00010	0.0568	0.0040	2616	31	2281	13	2294	13
JPN3B	0.11445	0.00011	0.1318	0.0093	2924	91	2054	15	2083	15
JPN4	0.11593	0.00010	0.0447	0.0032	2065	22	1856	13	1866	13
JPN9	0.11256	0.00012	0.1042	0.0074	3013	70	2305	16	2328	16
K13A5	0.11279	0.00010	0.3012	0.0213	-		2274	13	2341	16
N1C	0.11448	0.00011	0.2966	0.0210	-		2050	15	2115	17
X04	0.11644	0.00016	0.3331	0.0236	-		1788	21	1862	24
X05	0.11474	0.00016	0.5755	0.0407	-		2015	21	2143	28
X06	0.11393	0.00027	0.2198	0.0155	4214	316	2123	36	2172	37
JPS4	0.11036	0.00010	0.6213	0.0439	-		2596	13	2733	23
JPS6A	0.11410	0.00011	2.8099	0.1987	-		2100	15	2721	87
JPS6B	0.11390	0.00010	2.4125	0.1706	-		2127	13	2660	75

All the age estimates are recalculated using the present-day mantle values of Meisel et al. (2001) ( $^{187}\text{Os}/^{188}\text{Os} = 0.1296$  and  $^{187}\text{Re}/^{188}\text{Os} = 0.4353$ ). Uncertainties are reported as 2 std. dev. Uncertainties on  $^{187}\text{Re}/^{188}\text{Os}$  is assumed to be 3%, which is similar to the reproducibility of Re measurements reported by Irvine et al. (2003). For  $T_{\text{RD}}$  eruption ages calculations, the age of the kimberlite eruptions are assumed to be  $100 \pm 12$  Ma, following the range of ages reported by Wu et al. (2010).



# Appendix B

**Table B-1** Selected microprobe analyses of sulfides from Somerset Island.

Sulfide name	O	S	K	Cu	Ni	Fe	Co	Total	type	host phase	core/rim
<i>Sample A</i>											
	2.28	26.02	0.00	0.00	69.08	1.76	0.02	99.19	s-int		
X07-a-F	1.39	31.88	0.01	0.77	41.45	21.18	0.77	97.43	fi	olivine	
X07-a-F	2.98	30.44	0.00	0.50	40.82	20.61	0.82	96.22	fi	olivine	
X07-a-F	3.00	29.97	0.00	0.32	40.49	19.82	1.02	94.62	fi	olivine	
X07-a-D	9.26	23.84	0.02	0.05	54.26	6.23	0.30	94.02	fi?	olivine	
	0.49	27.82	0.01	0.00	66.53	2.12	3.22	100.20	s-int		
	1.87	26.67	0.04	0.00	70.17	1.76	0.02	100.53	s-int		
	0.52	27.42	0.00	0.00	72.00	1.59	0.00	101.55	s-int		
	0.47	26.60	0.00	0.00	70.75	1.85	0.00	99.67	s-int		
	1.33	26.83	0.00	0.00	69.31	1.68	0.01	99.16	s-int		
X07-e-A	0.26	32.09	0.00	0.00	34.84	11.79	16.56	95.54	fi	olivine	rim
X07-e-A	1.72	27.21	0.00	0.07	55.98	8.02	0.81	93.80	fi	olivine	core
X07-e-A	0.29	33.30	0.00	0.13	34.60	11.67	17.12	97.11	fi	olivine	
X07-e-A	0.77	28.08	0.00	0.00	59.95	6.18	0.72	95.70	fi	olivine	
X07-f-A	0.11	39.32	0.00	0.02	0.67	60.54	0.06	100.72	i-in	orthopyroxene	
X07-f-A	0.14	33.84	0.00	1.71	29.59	34.30	0.56	100.13	i-in	orthopyroxene	
X07-f-A	1.01	32.99	0.00	0.00	30.30	34.63	0.61	99.54	i-in	orthopyroxene	
X07-f-A	0.28	39.70	0.00	0.00	0.50	61.39	0.10	101.97	i-in	orthopyroxene	
X07-g-A	0.25	33.03	0.00	0.00	43.00	18.66	4.11	99.06	s-int		
X07-g-B	0.14	27.07	0.00	0.00	72.16	1.65	0.00	101.02	s-int		
X07-g-B	0.19	33.28	0.00	0.00	47.27	17.65	0.41	98.80	s-int		
X07-i-A	0.61	25.93	0.00	60.14	1.37	12.36	0.06	100.47	fi	olivine	rim
X07-i-A	0.68	33.16	0.00	0.44	40.67	22.16	1.03	98.13	fi	olivine	core
X07-i-A	2.42	32.36	0.00	0.64	39.23	21.74	0.64	97.02	fi	olivine	core
X07-i-A	2.31	31.44	0.00	0.01	40.02	20.94	0.83	95.53	fi	olivine	rim
X07-ii-A	0.62	20.89	0.00	77.09	1.58	1.75	0.16	102.09	fi	olivine	rim
X07-ii-A	0.27	27.49	0.00	4.81	66.00	1.91	0.03	100.51	fi	olivine	rim
X07-ii-B	2.95	31.71	0.00	0.00	41.09	18.41	3.68	97.83	fi	olivine	rim
X07-ii-B	1.88	33.24	0.00	3.12	39.76	20.59	0.84	99.44	fi	olivine	rim
X07-ii-B	1.25	32.64	0.00	0.00	40.23	17.65	7.55	99.30	fi	olivine	rim
X07-ii-B	1.41	31.74	0.00	0.00	44.06	19.47	1.28	97.95	fi	olivine	core
	2.38	26.98	0.00	0.00	69.20	1.72	1.28	101.55	s-int		
X07-cii-A	1.29	32.85	0.00	0.00	36.18	27.53	0.62	98.48	fi	orthopyroxene	core
X07-cii-A	2.56	33.90	0.00	26.75	7.55	29.06	0.19	100.00	fi	orthopyroxene	rim
X07-cii-A	0.98	33.17	0.00	0.00	35.32	28.59	0.59	98.63	fi	orthopyroxene	core
X07-fii-A	0.47	33.43	0.00	4.74	28.98	29.86	0.68	98.16	fi	olivine	rim
X07-fii-A	1.06	33.13	0.00	0.00	34.69	29.32	0.82	99.02	fi	olivine	core
X07-fii-A	0.73	32.82	0.00	28.09	4.67	28.61	0.18	95.11	fi	olivine	rim
X07-all-A	1.98	21.43	0.00	72.68	2.03	2.27	0.13	100.52	fi	olivine	
X07-all-A	0.19	33.61	0.01	0.80	43.14	20.50	0.78	99.03	fi	olivine	core
X07-all-A	0.08	32.97	0.00	3.65	40.22	19.91	2.36	99.20	fi	olivine	rim
X07-all-A	0.19	33.65	0.02	0.00	42.37	22.67	0.51	99.41	fi	olivine	core
X07-all-A	0.32	22.25	0.01	65.71	6.11	3.99	0.15	98.54	fi	olivine	
X07-dii-A	0.92	33.25	0.00	0.84	34.90	27.65	0.59	98.14	fi	orthopyroxene	
X07-dii-A	1.38	32.57	0.00	0.02	36.92	26.53	0.58	97.99	fi	orthopyroxene	rim
<i>Sample B</i>											
JPN11-0-a	0.10	39.04	0.00	0.00	13.20	47.60	0.13	100.07	i-in	olivine	
JPN11-0-a	0.48	33.94	0.00	0.00	32.34	31.69	0.73	99.17	i-in	olivine	
JPN11-0-a	0.11	38.41	0.00	0.00	12.53	48.72	0.16	99.93	i-in	olivine	
JPN11-0-b	0.04	33.17	0.00	1.23	30.64	31.40	0.48	96.96	i-in	olivine	core
	1.20	27.43	0.00	0.00	69.66	1.85	0.02	100.15	s-int		
	2.50	27.56	0.00	0.00	66.47	2.03	0.00	98.56	s-int		
	1.18	26.01	0.00	0.00	68.09	1.95	0.00	97.23	s-int		
JPN11-0-a	0.31	33.94	0.02	0.00	37.31	28.90	0.59	101.11	i-in	olivine	
JPN11-0-a	0.19	39.16	0.00	0.00	16.18	46.09	0.17	101.79	i-in	olivine	
JPN11-0-a	0.18	38.52	0.02	0.00	24.54	37.26	0.73	101.27	i-in	olivine	
JPN11-all-A	5.00	27.75	0.00	0.00	50.47	7.86	0.49	91.57	fi	orthopyroxene	rim

## Appendix B

Sulfide name	O	S	K	Cu	Ni	Fe	Co	Total	type	host phase	core/rim
JPN11-all-A	6.48	19.15	0.01	64.45	1.35	2.18	0.10	93.73	fi	orthopyroxene	rim
JPN11-all-A	5.84	30.09	0.00	0.00	35.70	21.45	1.07	94.15	fi	orthopyroxene	rim
JPN11-all-A	4.97	29.31	0.00	0.00	37.03	20.64	0.56	92.52	fi	orthopyroxene	core
JPN11-bII-A	0.37	33.47	0.00	0.00	33.91	29.81	0.75	98.31	fi	garnet	rim
JPN11-bII-A	0.92	32.95	0.01	0.00	33.47	28.59	0.74	96.68	fi	garnet	rim
JPN11-bII-A	0.56	33.34	0.01	0.12	32.74	28.90	0.90	96.57	fi	garnet	rim
JPN11-bII-A	1.80	32.34	0.00	0.00	34.20	28.27	0.38	96.99	fi	garnet	core
JPN11-bII-A	11.57	28.67	0.10	0.00	32.32	27.42	0.32	100.39	fi	garnet	core
JPN11-n-A	1.45	31.69	0.00	0.00	34.35	14.71	14.41	96.60	fi	olivine	
<i>Sample C</i>											
JPN3A-0-B	0.16	34.18	0.00	0.00	36.20	30.74	0.81	102.14	fi	olivine	rim
JPN3A-0-B	0.16	33.79	0.00	0.00	36.21	30.62	0.56	101.34	fi	olivine	rim
JPN3A-0-B	0.12	33.49	0.00	0.00	37.06	30.40	0.55	101.60	fi	olivine	core
JPN3A-0-C	0.21	33.47	0.03	0.00	36.72	30.63	0.75	101.82	l-int		
JPN3A-0-C	0.61	32.97	0.04	0.00	34.58	32.30	0.60	101.10	l-int		
JPN3A-0-D	0.27	33.72	0.01	0.00	33.37	34.17	0.55	102.08	fi	olivine	
JPN3A-0-D	0.12	33.43	0.00	0.52	33.85	32.60	0.61	101.14	fi	olivine	
JPN3A-0-F	0.21	33.80	0.03	0.00	39.64	26.22	0.91	100.79	fi	olivine	rim
JPN3A-0-F	0.22	33.38	0.01	0.00	38.67	25.65	1.74	99.67	fi	olivine	rim
JPN3A-0-F	1.53	32.95	0.00	0.00	39.87	25.29	0.69	100.34	fi	olivine	core
JPN3A-0-F	0.50	33.80	0.00	0.00	40.60	26.26	0.79	101.94	fi	olivine	core
	5.33	29.18	0.00	0.00	39.36	14.42	9.94	98.23	s-int		
JPN3A-d-A	0.21	33.03	0.00	0.00	38.07	28.28	0.77	100.36	fi	olivine	
JPN3A-d-A	0.14	33.23	0.00	0.00	38.30	26.56	1.17	99.40	fi	olivine	rim
JPN3A-d-C	1.12	31.83	0.00	0.00	38.01	24.83	1.70	97.48	fi	olivine	rim
JPN3A-d-C	0.61	33.03	0.00	0.23	38.12	26.94	0.57	99.50	fi	olivine	core
JPN3A-d-B	0.24	33.42	0.00	0.00	38.83	28.03	0.48	100.99	fi	olivine	core
JPN3A-d-B	0.27	33.00	0.00	0.00	37.95	27.33	0.87	99.42	fi	olivine	rim
JPN3A-d-D	0.17	33.19	0.00	0.00	34.30	32.41	0.80	100.87	l-int		core
JPN3A-d-D	0.19	33.77	0.00	0.00	33.18	33.29	0.73	101.16	l-int		rim
JPN3A-c-A	0.48	33.29	0.00	0.00	35.52	28.53	1.05	98.86	fi	olivine	
JPN3A-c-A	0.80	32.66	0.00	0.00	37.28	28.27	0.65	99.65	fi	olivine	
JPN3A-c-A	1.16	31.82	0.00	0.00	36.67	26.82	0.89	97.36	fi	olivine	
JPN3A-c-B	0.33	33.27	0.00	0.00	37.51	28.56	0.97	100.64	fi	olivine	
JPN3A-c-B	0.13	33.15	0.00	0.00	38.78	27.67	0.70	100.44	fi	olivine	
JPN3A-c-B	0.36	33.16	0.00	0.00	35.48	31.54	0.50	101.05	fi	olivine	
JPN3A-c-B	0.05	33.12	0.00	0.00	36.98	28.57	0.68	99.40	fi	olivine	
JPN3A-c-C	0.41	33.30	0.00	0.00	40.92	25.00	0.83	100.45	fi	olivine	core
JPN3A-c-C	0.35	32.75	0.00	0.00	40.84	25.16	0.78	99.87	fi	olivine	core
JPN3A-c-C	0.33	33.17	0.00	0.00	37.09	21.33	8.49	100.41	fi	olivine	rim
JPN3A-c-C	0.44	33.35	0.00	0.00	40.13	24.79	1.31	100.02	fi	olivine	rim
JPN3A-e-B	0.89	32.40	0.00	7.08	26.78	27.98	0.63	95.77	fi	clinopyroxene	
JPN3A-e-B	0.71	32.38	0.00	0.00	33.91	29.56	0.48	97.04	fi	clinopyroxene	
JPN3A-e-B	0.89	32.34	0.00	0.00	34.21	30.24	0.73	98.40	fi	clinopyroxene	
JPN3A-e-A	0.12	33.53	0.00	0.00	33.99	33.08	0.60	101.31	l-int		core
JPN3A-e-A	0.15	33.22	0.00	0.00	34.54	32.59	0.65	101.14	l-int		rim
JPN3A-e-A	1.13	32.59	0.00	0.00	33.74	31.77	0.93	100.16	l-int		rim
JPN3A-e-A	0.35	33.84	0.00	0.00	34.04	32.08	0.65	100.96	l-int		rim
JPN3A-h-A	0.06	33.39	0.00	0.00	37.87	29.20	0.63	101.16	fi	olivine	core
JPN3A-h-A	0.43	33.43	0.00	0.95	37.42	27.47	0.79	100.49	fi	olivine	core
JPN3A-h-A	0.30	33.39	0.00	0.00	36.70	28.96	0.96	100.30	fi	olivine	rim
JPN3A-h-A	0.17	33.32	0.00	0.00	38.13	27.41	0.94	99.96	fi	olivine	rim
	0.29	33.12	0.00	0.00	38.51	24.98	2.21	99.11	s-int		
JPN3A-h-C	0.72	32.41	0.00	0.00	34.51	29.48	0.88	97.99	fi	olivine	rim
JPN3A-h-C	0.35	32.39	0.00	0.00	37.81	28.31	0.53	99.38	fi	olivine	core
JPN3A-h-C	0.27	33.64	0.00	0.00	38.23	28.68	0.57	101.40	fi	olivine	core
JPN3A-h-C	0.22	33.56	0.00	0.00	34.86	32.04	0.74	101.42	fi	olivine	rim
JPN3A-f-A	0.09	33.94	0.00	0.22	33.64	32.27	0.58	100.73	fi	olivine	core
JPN3A-f-A	0.36	33.34	0.00	0.00	34.65	31.05	0.74	100.15	fi	olivine	rim
JPN3A-f-A	0.26	33.63	0.00	0.00	34.89	30.79	0.86	100.42	fi	olivine	rim
JPN3A-f-A	0.21	33.54	0.00	0.00	32.37	33.19	0.73	100.04	fi	olivine	rim
JPN3A-f-A	0.21	33.48	0.00	1.25	33.83	30.39	0.74	99.90	fi	olivine	core
JPN3A-f-A	0.29	33.34	0.00	0.49	32.86	32.24	0.55	99.77	fi	olivine	core
JPN3A-f-B	0.14	33.66	0.00	0.00	36.36	28.66	1.16	99.98	fi	olivine	rim
JPN3A-f-B	0.25	32.93	0.00	0.00	36.68	29.29	0.96	100.11	fi	olivine	rim

Sulfide name	O	S	K	Cu	Ni	Fe	Co	Total	type	host phase	core/rim
JPN3A-f-B	0.23	33.00	0.00	0.00	36.31	29.60	0.98	100.11	fi	olivine	rim
JPN3A-f-B	0.26	33.29	0.00	0.00	36.05	29.45	1.11	100.16	fi	olivine	
JPN3A-f-B	0.53	32.07	0.00	0.04	38.59	26.22	0.72	98.16	fi	olivine	core
JPN3A-f-B2	0.18	32.99	0.00	0.00	36.86	28.09	0.60	98.71	fi	olivine	rim
JPN3A-f-B2	0.08	32.99	0.00	0.00	36.21	28.88	0.59	98.74	fi	olivine	rim
JPN3A-f-B2	0.22	32.11	0.00	0.00	35.72	30.09	0.75	98.89	fi	olivine	rim
JPN3A-i-D	0.19	33.81	0.00	0.00	33.78	33.27	0.63	101.69	fi	orthopyroxene	
JPN3A-i-D	0.03	33.99	0.00	0.00	33.73	33.40	0.60	101.75	fi	orthopyroxene	
JPN3A-i-D	0.21	33.60	0.00	1.40	31.77	32.67	0.54	100.19	fi	orthopyroxene	
JPN3A-i-D	0.13	33.39	0.00	0.00	33.85	32.68	0.71	100.76	fi	orthopyroxene	
JPN3A-i-D	0.64	33.44	0.00	1.34	31.45	31.60	0.72	99.19	fi	orthopyroxene	
JPN3A-i-C	0.11	33.30	0.00	0.00	37.22	27.79	1.31	99.72	fi	olivine	rim
JPN3A-i-C	0.10	33.91	0.00	0.00	35.98	29.92	0.74	100.65	fi	olivine	rim
JPN3A-i-C	0.10	33.39	0.00	3.93	32.53	29.42	0.56	99.93	fi	olivine	core
JPN3A-i-C	0.23	34.25	0.00	0.00	36.55	29.99	0.55	101.57	fi	olivine	core
JPN3A-i-C	0.18	33.85	0.00	1.71	34.88	28.70	0.50	99.83	fi	olivine	core
JPS6-O-C	0.27	33.53	0.03	0.00	33.63	32.63	1.09	101.18	fi	olivine	
JPS6-O-C	0.15	33.46	0.00	0.00	33.68	32.90	0.96	101.16	fi	olivine	
<i>Sample D</i>											
	1.83	32.19	8.10	0.11	19.23	34.89	1.62	97.98	s-int		
	2.28	32.15	8.67	0.29	17.77	35.47	1.37	98.01	s-int		
JPS6-O-F	0.00	34.80	0.00	32.39	0.69	30.74	0.01	98.64	i-in	olivine	rim
JPS6-O-F	0.11	32.92	0.00	0.00	36.41	29.07	0.57	99.07	i-in	olivine	
JPS6-O-F	0.01	39.32	0.00	0.00	14.84	45.69	0.32	100.16	i-in	olivine	
JPS6-O-E	0.07	32.73	0.00	0.00	34.28	31.67	0.91	99.67	fi	clinopyroxene	
JPS6-O-E	0.25	33.06	0.00	0.00	34.20	31.41	1.01	99.94	fi	clinopyroxene	
JPS6-O-E	0.23	32.36	9.43	5.15	12.98	37.25	0.17	97.58	fi	clinopyroxene	
	0.25	33.11	9.10	1.51	18.42	35.72	0.28	98.43	s-int		
	0.25	32.50	9.42	4.55	15.45	35.73	0.28	98.25	s-int		
JPS6-O-F	0.21	39.63	0.00	0.00	14.23	48.16	0.27	102.50	i-in	olivine	
JPS6-O-F	0.08	35.08	0.04	33.11	0.21	31.27	0.07	99.98	i-in	olivine	
JPS6-O-F	0.26	33.77	0.00	0.00	36.37	30.31	0.63	101.39	i-in	olivine	
JPS6-O-D	0.26	34.79	0.01	32.93	0.72	30.95	0.08	99.93	fi	olivine	rim
JPS6-O-D	0.63	35.40	0.00	32.95	0.58	31.01	0.05	100.73	fi	olivine	rim
JPS6-O-D	1.26	33.20	0.00	0.00	32.78	32.25	0.74	100.22	fi	olivine	core
JPS6-O-C	0.29	34.04	0.01	0.89	32.10	32.24	0.89	100.45	fi	olivine	rim
JPS6-O-A	0.85	32.64	9.63	0.91	15.99	39.10	0.19	99.30	fi	olivine	core
JPS6-O-A	0.24	32.55	9.36	1.43	16.16	38.16	0.67	98.59	fi	olivine	rim
JPS6-O-A	0.35	33.45	9.87	0.70	14.60	39.69	0.19	98.86	fi	olivine	rim
	0.27	33.37	9.47	3.59	13.68	38.69	0.22	99.30	s-int		
	0.41	32.89	9.41	0.71	17.20	36.97	0.26	97.86	s-int		
	0.45	35.02	0.00	0.00	60.07	2.47	0.95	98.97	s-int		
	0.96	32.36	9.26	4.44	15.07	35.89	0.42	98.46	s-int		
JPS6A-e-A	0.00	34.47	0.00	32.63	0.17	31.55	0.31	99.13	fi	olivine	rim
JPS6A-e-A	0.07	34.74	0.00	32.98	0.22	31.38	0.13	99.51	fi	olivine	rim
JPS6A-e-A	1.49	32.95	0.00	0.00	30.95	33.06	1.40	99.86	fi	olivine	
JPS6A-e-E	0.24	32.95	9.49	3.71	13.65	38.80	0.25	99.08	l-int		
JPS6A-e-E	0.19	32.83	9.30	3.08	14.25	39.10	0.27	99.01	l-int		
JPS6A-e-E	0.20	32.38	9.57	2.62	15.01	38.84	0.21	98.83	l-int		
JPS6A-e-D	0.15	33.04	0.00	0.00	34.80	30.64	1.36	99.99	fi	olivine	
JPS6A-e-D	0.18	32.98	0.00	0.00	34.54	30.78	1.29	99.77	fi	olivine	
JPS6A-e-D	0.03	34.68	0.00	31.93	0.43	30.30	0.09	97.45	fi	olivine	
JPS6A-e-C	0.07	32.67	9.50	9.29	11.19	35.96	0.11	98.78	fi	olivine	
JPS6A-e-C	0.21	33.23	0.00	0.00	35.10	31.34	0.98	100.85	fi	olivine	
JPS6A-e-C	0.25	32.54	9.25	8.04	11.78	37.25	0.08	99.18	fi	olivine	
JPS6A-d-A	0.39	31.84	3.97	0.04	29.46	32.98	1.12	99.81	fi	olivine	
JPS6A-d-A	0.34	32.18	9.55	1.22	17.46	38.42	0.29	99.46	fi	olivine	
JPS6A-d-C	0.66	32.23	0.00	0.00	33.76	31.82	1.86	100.33	fi	garnet	core
JPS6A-d-A	0.15	33.06	0.01	0.00	34.70	31.93	1.84	101.69	fi	olivine	core
JPS6A-d-A	0.15	33.41	0.03	0.00	34.72	31.93	1.78	102.01	fi	olivine	core
JPS6A-d-A	0.25	32.29	9.64	1.14	18.03	37.50	0.31	99.16	fi	olivine	rim
JPS6A-d-D	0.24	32.96	0.00	0.00	33.11	33.82	0.98	101.11	fi	garnet	
JPS6A-d-B	0.06	33.54	0.00	33.22	0.31	31.12	0.00	98.25	fi	olivine	rim
JPS6A-d-B	0.12	30.81	0.00	0.00	34.28	30.74	1.72	97.68	fi	olivine	rim
JPS6A-a-B	0.45	38.96	0.02	0.00	15.42	44.70	0.28	99.83	i-in	olivine	

## Appendix B

Sulfide name	O	S	K	Cu	Ni	Fe	Co	Total	type	host phase	core/rim
JPS6A-a-C	1.28	34.47	0.02	31.54	1.13	30.96	0.10	99.49	i-in	olivine	rim
JPS6A-a-C	0.47	36.66	0.00	0.00	16.58	47.29	0.39	101.39	i-in	olivine	core
JPS6A-a-C	0.86	33.96	0.02	0.05	28.71	36.02	0.63	100.24	i-in	olivine	core
JPS6A-a-C	0.51	34.14	0.02	0.00	24.49	41.43	0.46	101.04	i-in	olivine	core
JPS6A-a-C	1.72	36.53	0.00	0.72	14.83	45.80	0.31	99.90	i-in	olivine	
JPS6A-a-D	0.30	33.49	0.00	0.00	34.42	31.77	0.78	100.76	fi	olivine	
JPS6A-a-D	0.72	32.65	9.13	7.21	12.04	37.63	0.11	99.49	fi	olivine	
JPS6A-d-F	0.26	33.38	0.00	0.00	33.81	31.99	1.01	100.45	fi	olivine	
JPS6A-d-F	0.34	33.39	0.00	0.00	34.45	32.23	0.88	101.29	fi	olivine	core
JPS6A-d-F	0.69	32.64	9.40	8.11	10.34	37.33	0.12	98.64	fi	olivine	rim
JPS6A-d-C	1.19	32.59	0.02	0.00	32.29	32.84	0.70	99.62	fi	garnet	
JPS6A-d-C	0.00	35.22	0.01	32.46	0.31	31.26	0.03	99.29	fi	garnet	rim
JPS6A-d-C	0.18	34.55	0.02	32.60	0.33	31.20	0.08	98.96	fi	garnet	rim
JPS6A-d-C	0.48	36.49	0.02	32.63	0.24	31.42	0.04	101.33	fi	garnet	rim
JPS6A-d-E	0.19	33.19	0.98	0.00	33.42	30.41	2.36	100.55	fi	olivine	
JPS6A-d-E	0.36	32.61	9.49	2.31	16.64	37.26	0.24	98.90	fi	olivine	
JPS6A-d-E	0.33	33.06	3.69	0.11	30.01	31.07	2.60	100.85	fi	olivine	
JPS6A-d-E	0.58	33.15	9.49	2.63	16.22	37.10	0.15	99.32	fi	olivine	
JPS6A-b-A	1.68	33.10	0.00	0.00	32.09	31.46	0.80	99.13	fi	olivine	rim

All the concentrations are reported as wt.%. The sulfides are subdivided in four types following the classification described in the text (fi : fractured inclusions, i-in : isolated inclusions, s-int : small interstitial, l-int : large interstitial). Some analyses have poor totals because they were performed in small sulfide domains (< 2  $\mu\text{m}$  across) due to the lack of larger homogenous portions. The data with totals < 98% are reported only for qualitative considerations.

## APPENDIX C

### SULFIDE MINERAL FORMULAE

In order to help the reader with the sulfide mineral nomenclature, in the following table the sulfide cited in this thesis are reported along with their chemical formulae.

<b>Sulfide name</b>	<b>Chemical formula</b>
Chalcocite	$\text{Cu}_2\text{S}$
Chalcopyrite	$\text{CuFeS}_2$
Digenite	$\text{Cu}_9\text{S}_5$
Djerfisherite	$\text{K}_6(\text{Fe,Cu,Ni})_{25}\text{S}_{26}\text{Cl}$
Erlichmanite	$\text{OsS}_2$
Heazlewoodite	$\text{Ni}_3\text{S}_2$
Laurite	$\text{RuS}_2$
Millerite	$\text{NiS}$
Monosulfide solid solution (mss)	$(\text{Fe,Ni,Cu})_{1-x}\text{S}$
Pentlandite	$(\text{Fe,Ni})_9\text{S}_8$
Pyrite	$\text{FeS}_2$
Pyrrhotite	$\text{Fe}_{1-x}\text{S}$
Sphalerite	$\text{ZnS}$
Troilite	$\text{FeS}$



## REFERENCES

- Abrajano, T.A.J., Pasteris, J.D., 1989. Zambales ophiolite, Philippines. *Contrib. Mineral. Petrol.* 103, 64–77. doi:10.1007/BF00371365
- Ackerman, L., Walker, R.J., Puchtel, I.S., Pitcher, L., Jelínek, E., Strnad, L., 2009. Effects of melt percolation on highly siderophile elements and Os isotopes in subcontinental lithospheric mantle: A study of the upper mantle profile beneath Central Europe. *Geochim. Cosmochim. Acta* 73, 2400–2414. doi:10.1016/j.gca.2009.02.002
- Alard, O., Griffin, W.L., Lorand, J.-P., Jackson, S.E., O'Reilly, S.Y., 2000. Non-chondritic distribution of the highly siderophile elements in mantle sulphides. *Nature* 407, 891–894. doi:10.1038/35038049
- Alard, O., Griffin, W.L., Pearson, N.J., Lorand, J.-P., O'Reilly, S.Y., 2002. New insights into the Re-Os systematics of sub-continental lithospheric mantle from in situ analysis of sulphides. *Earth Planet. Sci. Lett.* 203, 651–663. doi:10.1016/S0012-821X(02)00799-9
- Alard, O., Lorand, J.-P., Reisberg, L., Bodinier, J.-L., Dautria, J.-M., O'Reilly, S.Y., 2011. Volatile-rich Metasomatism in Montferrier Xenoliths (Southern France): Implications for the Abundances of Chalcophile and Highly Siderophile Elements in the Subcontinental Mantle. *J. Petrol.* 52, 2009–2045. doi:10.1093/petrology/egr038
- Albarède, F., Ballhaus, C., Blichert-Toft, J., Lee, C.-T., Marty, B., Moynier, F., Yin, Q.-Z., 2013. Asteroidal impacts and the origin of terrestrial and lunar volatiles. *Icarus* 222, 44–52. doi:10.1016/j.icarus.2012.10.026
- Alt, J.C., Shanks, W.C., 1998. Sulfur in serpentinized oceanic peridotites: Serpentinization processes and microbial sulfate reduction. *J. Geophys. Res. Solid Earth* 103, 9917–9929. doi:10.1029/98JB00576
- Anderson, D.L., 1989. *Theory of the Earth*. Blackwell Scientific.
- Arndt, N.T., Coltice, N., Helmstaedt, H., Gregoire, M., 2009. Origin of Archean subcontinental lithospheric mantle: Some petrological constraints. *Lithos* 109, 61–71. doi:10.1016/j.lithos.2008.10.019
- Aulbach, S., 2012. Craton nucleation and formation of thick lithospheric roots. *Lithos* 149, 16–30. doi:10.1016/j.lithos.2012.02.011

- Aulbach, S., Griffin, W.L., Pearson, N.J., O'Reilly, S.Y., 2013. Nature and timing of metasomatism in the stratified mantle lithosphere beneath the central Slave craton (Canada). *Chem. Geol.* 352, 153–169. doi:10.1016/j.chemgeo.2013.05.037
- Aulbach, S., Griffin, W.L., Pearson, N.J., O'Reilly, S.Y., Kivi, K., Doyle, B.J., 2004. Mantle formation and evolution, Slave Craton: constraints from HSE abundances and Re-Os isotope systematics of sulfide inclusions in mantle xenocrysts. *Chem. Geol.* 208, 61–88. doi:16/j.chemgeo.2004.04.006
- Aulbach, S., Krauss, C., Creaser, R.A., Stachel, T., Heaman, L.M., Matveev, S., Chacko, T., 2010. Granulite sulphides as tracers of lower crustal origin and evolution: An example from the Slave craton, Canada. *Geochim. Cosmochim. Acta* 74, 5368–5381. doi:10.1016/j.gca.2010.06.005
- Aulbach, S., Stachel, T., Creaser, R.A., Heaman, L.M., Shirey, S.B., Muehlenbachs, K., Eichenberg, D., Harris, J.W., 2009. Sulphide survival and diamond genesis during formation and evolution of Archaean subcontinental lithosphere: A comparison between the Slave and Kaapvaal cratons. *Lithos* 112, 747–757. doi:16/j.lithos.2009.03.048
- Aulbach, S., Stachel, T., Heaman, L.M., Creaser, R.A., Shirey, S.B., 2011. Formation of cratonic subcontinental lithospheric mantle and complementary komatiite from hybrid plume sources. *Contrib. Mineral. Petrol.* 161, 947–960. doi:10.1007/s00410-010-0573-4
- Ballhaus, C., Bockrath, C., Wohlgemuth-Ueberwasser, C., Laurenz, V., Berndt, J., 2006. Fractionation of the noble metals by physical processes. *Contrib. Mineral. Petrol.* 152, 667–684. doi:10.1007/s00410-006-0126-z
- Ballhaus, C., Laurenz, V., Münker, C., Fonseca, R.O.C., Albarède, F., Rohrbach, A., Lagos, M., Schmidt, M.W., Jochum, K.-P., Stoll, B., Weis, U., Helmy, H.M., 2013. The U/Pb ratio of the Earth's mantle—A signature of late volatile addition. *Earth Planet. Sci. Lett.* 362, 237–245. doi:10.1016/j.epsl.2012.11.049
- Barton Jr., P.B., Bethke, P.M., 1987. Chalcopyrite disease in sphalerite: pathology and epidemiology. *Am. Mineral.* 72, 451–467.
- Becker, H., Dalpe, C., Walker, R.J., 2002. High-precision Ru isotopic measurements by multi-collector ICP-MS. *Analyst* 127, 775–780. doi:10.1039/B200596D
- Becker, H., Horan, M.F., Walker, R.J., Gao, S., Lorand, J.-P., Rudnick, R.L., 2006. Highly siderophile element composition of the Earth's primitive upper mantle: Constraints from new data on peridotite massifs and xenoliths. *Geochim. Cosmochim. Acta* 70, 4528–4550. doi:16/j.gca.2006.06.004
- Begemann, F., Ludwig, K.R., Lugmair, G.W., Min, K., Nyquist, L.E., Patchett, P.J., Renne, P.R., Shih, C.-Y., Villa, I.M., Walker, R.J., 2001. Call for an improved set of decay

- constants for geochronological use. *Geochim. Cosmochim. Acta* 65, 111–121. doi:10.1016/S0016-7037(00)00512-3
- Bente, P.D.K., Doering, D.T., 1995. Experimental studies on the solid state diffusion of Cu + In in ZnS and on “Disease”, DIS (Diffusion Induced Segregations), in sphalerite and their geological applications. *Mineral. Petrol.* 53, 285–305. doi:10.1007/BF01160153
- Berman, R.G., Davis, W.J., Pehrsson, S., 2007. Collisional Snowbird tectonic zone resurrected: Growth of Laurentia during the 1.9 Ga accretionary phase of the Hudsonian orogeny. *Geology* 35, 911–914. doi:10.1130/G23771A.1
- Berman, R.G., Pehrsson, S., Davis, W.J., Ryan, J.J., Qui, H., Ashton, K.E., 2013. The Arrowsmith orogeny: Geochronological and thermobarometric constraints on its extent and tectonic setting in the Rae craton, with implications for pre-Nuna supercontinent reconstruction. *Precambrian Res.* 232, 44–69. doi:10.1016/j.precamres.2012.10.015
- Bézos, A., Lorand, J.-P., Humler, E., Gros, M., 2005. Platinum-group element systematics in Mid-Oceanic Ridge basaltic glasses from the Pacific, Atlantic, and Indian Oceans. *Geochim. Cosmochim. Acta* 69, 2613–2627. doi:10.1016/j.gca.2004.10.023
- Birck, J.L., Barman, M.R., Capmas, F., 1997. Re-Os Isotopic Measurements at the Femtomole Level in Natural Samples. *Geostand. Newsl.* 21, 19–27. doi:10.1111/j.1751-908X.1997.tb00528.x
- Bockrath, C., Ballhaus, C., Holzheid, A., 2004. Fractionation of the Platinum-Group Elements During Mantle Melting. *Science* 305, 1951–1953. doi:10.1126/science.1100160
- Borisov, A., Palme, H., 2000. Solubilities of noble metals in Fe-containing silicate melts as derived from experiments in Fe-free systems. *Am. Mineral.* 85, 1665–1673. doi:10.2138/am-2000-11-1209
- Bowring, S.A., Williams, I.S., 1999. Priscoan (4.00–4.03 Ga) orthogneisses from northwestern Canada. *Contrib. Mineral. Petrol.* 134, 3–16. doi:10.1007/s004100050465
- Boyd, F.R., Mertzman, S.A., 1987. Composition and structure of the Kaapvaal lithosphere, southern Africa. *Magmat. Process. Physicochem. Princ.* 1, 13–24.
- Brenan, J.M., 2008. Re–Os fractionation by sulfide melt–silicate melt partitioning: A new spin. *Chem. Geol., Highly Siderophile Element Geochemistry* 248, 140–165. doi:10.1016/j.chemgeo.2007.09.003

- Brenan, J.M., Andrews, D., 2001. High-temperature stability of laurite and Ru–Os–Ir alloy and their role in PGE fractionation in mafic magmas. *Can. Mineral.* 39, 341–360. doi:10.2113/gscanmin.39.2.341
- Brenan, J.M., Cherniak, D.J., Rose, L.A., 2000. Diffusion of osmium in pyrrhotite and pyrite: implications for closure of the Re–Os isotopic system. *Earth Planet. Sci. Lett.* 180, 399–413. doi:10.1016/S0012-821X(00)00165-5
- Brenan, J.M., McDonough, W.F., 2009. Core formation and metal–silicate fractionation of osmium and iridium from gold. *Nat. Geosci.* 2, 798–801. doi:10.1038/ngeo658
- Brenan, J.M., McDonough, W.F., Dalpé, C., 2003. Experimental constraints on the partitioning of rhenium and some platinum-group elements between olivine and silicate melt. *Earth Planet. Sci. Lett.* 212, 135–150. doi:10.1016/S0012-821X(03)00234-6
- Brueckner, H.K., Roermund, H.L.M.V., Pearson, N.J., 2004. An Archean(?) to Paleozoic Evolution for a Garnet Peridotite Lens with Sub-Baltic Shield Affinity within the Seve Nappe Complex of Jämtland, Sweden, Central Scandinavian Caledonides. *J. Petrol.* 45, 415–437. doi:10.1093/petrology/egg088
- Buchan, K.L., LeCheminant, A.N., van Breemen, O., 2012. Malley diabase dykes of the Slave craton, Canadian Shield: U–Pb age, paleomagnetism, and implications for continental reconstructions in the early Paleoproterozoic. *Can. J. Earth Sci.* 49, 435–454. doi:10.1139/e11-061
- Büchl, A., Brüggemann, G., Batanova, V.G., Münker, C., Hofmann, A.W., 2002. Melt percolation monitored by Os isotopes and HSE abundances: a case study from the mantle section of the Troodos Ophiolite. *Earth Planet. Sci. Lett.* 204, 385–402. doi:10.1016/S0012-821X(02)00977-9
- Burton, K.W., Cenki-Tok, B., Mokadem, F., Harvey, J., Gannoun, A., Alard, O., Parkinson, I.J., 2012. Unradiogenic lead in Earth’s upper mantle. *Nat. Geosci.* 5, 570–573. doi:10.1038/ngeo1531
- Burton, K.W., Schiano, P., Birck, J.-L., Allègre, C.J., 1999. Osmium isotope disequilibrium between mantle minerals in a spinel-lherzolite. *Earth Planet. Sci. Lett.* 172, 311–322. doi:10.1016/S0012-821X(99)00207-1
- Cabri, L.J., Weiser, T.W., 1996. The mineralogy and distribution of platinum-group mineral (PGM) placer deposits of the world. *Explor. Min. Geol.* 73–167.
- Canil, D., 2008. Canada’s craton: A bottoms-up view. *GSA Today* 18, 4–10. doi:10.1130/GSAT01806A.1
- Carbno, G.B., Canil, D., 2002. Mantle Structure Beneath the SW Slave Craton, Canada: Constraints from Garnet Geochemistry in the Drybones Bay Kimberlite. *J. Petrol.* 43, 129–142. doi:10.1093/petrology/43.1.129

- Carlson, R.W., 2005. Application of the Pt-Re-Os isotopic systems to mantle geochemistry and geochronology. *Lithos* 82, 249–272. doi:16/j.lithos.2004.08.003
- Chakhmouradian, A.R., Mitchell, R.H., 2001. Three compositional varieties of perovskite from kimberlites of the Lac de Gras field (Northwest Territories, Canada). *Mineral. Mag.* 65, 133–148. doi:10.1180/002646101550082
- Chesley, J., Righter, K., Ruiz, J., 2004. Large-scale mantle metasomatism: a Re–Os perspective. *Earth Planet. Sci. Lett.* 219, 49–60. doi:10.1016/S0012-821X(03)00698-8
- Chesley, J.T., Rudnick, R.L., Lee, C.-T., 1999. Re–Os systematics of mantle xenoliths from the East African Rift: age, structure, and history of the Tanzanian craton. *Geochim. Cosmochim. Acta* 63, 1203–1217. doi:10.1016/S0016-7037(99)00004-6
- Chu, Z., Yan, Y., Chen, Z., Guo, J., Yang, Y., Li, C., Zhang, Y., 2014. A Comprehensive Method for Precise Determination of Re, Os, Ir, Ru, Pt, Pd Concentrations and Os Isotopic Compositions in Geological Samples. *Geostand. Geoanalytical Res.* n/a–n/a. doi:10.1111/j.1751-908X.2014.00283.x
- Clarke, D.B., 1979. Synthesis of Nickeloan Djerfisherites and the Origin of Potassic Sulphides at the Frank Smith Mine, in: Boyd, F.R., Meyer, H.O.A. (Eds.), *The Mantle Sample: Inclusion in Kimberlites and Other Volcanics*. American Geophysical Union, pp. 300–308.
- Clarke, D.B., Chapman, C.A.T., MacKay, R.M., Mitchell, R.H., 1994. Occurrence and origin of djerfisherite from the Elwin Bay Kimberlite, Somerset Island, Northwest Territories. *Can. Mineral.* 32, 815–823.
- Coggon, J.A., Luguët, A., Nowell, G.M., Appel, P.W.U., 2013. Hadean mantle melting recorded by southwest Greenland chromitite 186Os signatures. *Nat. Geosci.* doi:10.1038/ngeo1911
- Cohen, A.S., Waters, F.G., 1996. Separation of osmium from geological materials by solvent extraction for analysis by thermal ionisation mass spectrometry. *Anal. Chim. Acta* 332, 269–275. doi:10.1016/0003-2670(96)00226-7
- Coltorti, M., Grégoire, M., 2008. Metasomatism in oceanic and continental lithospheric mantle: introduction. *Geol. Soc. Lond. Spec. Publ.* 293, 1–9. doi:10.1144/SP293.1
- Cotton, S.A., 1997. *Chemistry of Precious Metals*. Springer Netherlands, Dordrecht.
- Cousens, B., Falck, H., Ootes, L., Jackson, V., Mueller, W., Corcoran, P., Finnigan, C., van Hees, C.F., Alcazar, A., 2006. Regional correlations, tectonic settings, and stratigraphic solutions in the Yellowknife greenstone belt and adjacent areas from geochemical and Sm–Nd isotopic analyses of volcanic and plutonic rocks, in: Mineral Deposits Division, Special Publication No. 3. Geological Association of Canada.

- Cousens, B.L., 2000. Geochemistry of the Archean Kam Group, Yellowknife Greenstone Belt, Slave Province, Canada. *J. Geol.* 108, 181–197. doi:10.1086/314397
- Craig, J.R., 1973. Pyrite-pentlandite assemblages and other low temperature relations in the Fe-Ni-S system. *Am J Sci* 273, 496–510.
- Czamanske, G.K., Moore, J.G., 1977. Composition and phase chemistry of sulfide globules in basalt from the Mid-Atlantic Ridge rift valley near 37°N lat. *Geol. Soc. Am. Bull.* 88, 587–599. doi:10.1130/0016-7606
- Dale, C.W., Burton, K.W., Pearson, D.G., Gannoun, A., Alard, O., Argles, T.W., Parkinson, I.J., 2009. Highly siderophile element behaviour accompanying subduction of oceanic crust: Whole rock and mineral-scale insights from a high-pressure terrain. *Geochim. Cosmochim. Acta* 73, 1394–1416. doi:10.1016/j.gca.2008.11.036
- Dale, C.W., Luguet, A., Macpherson, C.G., Pearson, D.G., Hickey-Vargas, R., 2008. Extreme platinum-group element fractionation and variable Os isotope compositions in Philippine Sea Plate basalts: Tracing mantle source heterogeneity. *Chem. Geol.* 248, 213–238. doi:10.1016/j.chemgeo.2007.11.007
- Dale, C.W., Macpherson, C.G., Pearson, D.G., Hammond, S.J., Arculus, R.J., 2012. Inter-element fractionation of highly siderophile elements in the Tonga Arc due to flux melting of a depleted source. *Geochim. Cosmochim. Acta* 89, 202–225. doi:10.1016/j.gca.2012.03.025
- Dauphas, N., Marty, B., 2002. Inference on the nature and the mass of Earth's late veneer from noble metals and gases. *J. Geophys. Res. Planets* 107, 5129. doi:10.1029/2001JE001617
- Dawson, J.B., 2002. Metasomatism and Partial Melting in Upper-Mantle Peridotite Xenoliths from the Lashaine Volcano, Northern Tanzania. *J. Petrol.* 43, 1749–1777. doi:10.1093/petrology/43.9.1749
- Day, J.M.D., 2013. Hotspot volcanism and highly siderophile elements. *Chem. Geol.* 341, 50–74. doi:10.1016/j.chemgeo.2012.12.010
- Delpech, G., Lorand, J.-P., Grégoire, M., Cottin, J.-Y., O'Reilly, S.Y., 2012. In-situ geochemistry of sulfides in highly metasomatized mantle xenoliths from Kerguelen, southern Indian Ocean. *Lithos* 154, 296–314. doi:10.1016/j.lithos.2012.07.018
- Dickin, A.P., 2005. Radiogenic isotope geology. Cambridge University Press.
- Ely, J.C., Neal, C.R., O'Neill Jr., J.A., Jain, J.C., 1999. Quantifying the platinum group elements (PGEs) and gold in geological samples using cation exchange pretreatment and ultrasonic nebulization inductively coupled plasma-mass spectrometry (USN-ICP-MS). *Chem. Geol.* 157, 219–234. doi:10.1016/S0009-2541(98)00204-6

- Ertel, W., Dingwell, D.B., Sylvester, P.J., 2008. Siderophile elements in silicate melts — A review of the mechanically assisted equilibration technique and the nanonugget issue. *Chem. Geol., Highly Siderophile Element Geochemistry* 248, 119–139. doi:10.1016/j.chemgeo.2007.12.013
- Fischer-Gödde, M., Becker, H., Wombacher, F., 2011. Rhodium, gold and other highly siderophile elements in orogenic peridotites and peridotite xenoliths. *Chem. Geol.* 280, 365–383. doi:10.1016/j.chemgeo.2010.11.024
- Fischer-Gödde, M., Becker, H., Wombacher, F., 2010. Rhodium, gold and other highly siderophile element abundances in chondritic meteorites. *Geochim. Cosmochim. Acta* 74, 356–379. doi:10.1016/j.gca.2009.09.024
- Fonseca, R.O.C., Laurenz, V., Mallmann, G., Luguet, A., Hoehne, N., Jochum, K.P., 2012. New constraints on the genesis and long-term stability of Os-rich alloys in the Earth's mantle. *Geochim. Cosmochim. Acta* 87, 227–242. doi:10.1016/j.gca.2012.04.002
- Fonseca, R.O.C., Mallmann, G., O'Neill, H.S.C., Campbell, I.H., Laurenz, V., 2011. Solubility of Os and Ir in sulfide melt: Implications for Re/Os fractionation during mantle melting. *Earth Planet. Sci. Lett.* 311, 339–350. doi:10.1016/j.epsl.2011.09.035
- Fonseca, R.O.C., Mallmann, G., O'Neill, H., Campbell, I.H., 2007. How chalcophile is rhenium? An experimental study of the solubility of Re in sulphide mattes. *Earth Planet. Sci. Lett.* 260, 537–548. doi:10.1016/j.epsl.2007.06.012
- Fortenfant, S.S., Dingwell, D.B., Ertel-Ingrisch, W., Capmas, F., Birck, J.L., Dalpé, C., 2006. Oxygen fugacity dependence of Os solubility in haplobasaltic melt. *Geochim. Cosmochim. Acta* 70, 742–756. doi:10.1016/j.gca.2005.10.004
- Foustoukos, D.I., Bizimis, M., Frisby, C., Shirey, S.B., 2015. Redox controls on Ni–Fe–PGE mineralization and Re/Os fractionation during serpentinization of abyssal peridotite. *Geochim. Cosmochim. Acta* 150, 11–25. doi:10.1016/j.gca.2014.11.025
- Francis, R., 1990. Sulfide Globules in Midocean Ridge Basalts (morb), and the Effect of Oxygen Abundance in Fe-S-O Liquids on the Ability of Those Liquids to Partition Metals from Morb and Komatiite Magmas. *Chem. Geol.* 85, 199–213. doi:10.1016/0009-2541(90)90001-N
- Frisch, T., 2011. Geology, Precambrian geology of northern Boothia Peninsula and Somerset Island, Nunavut (No. 6051). Geological Survey of Canada.
- Frisch, T., Hunt, P.A., 1993. Reconnaissance U–Pb geochronology of the crystalline core of the Boothia Uplift, District of Franklin, Northwest Territories. *Geol. Surv. Can., Radiogenic age and isotopic studies: report 7 93*, 3–22.

- Gannoun, A., Burton, K.W., Parkinson, I.J., Alard, O., Schiano, P., Thomas, L.E., 2007. The scale and origin of the osmium isotope variations in mid-ocean ridge basalts. *Earth Planet. Sci. Lett.* 259, 541–556. doi:10.1016/j.epsl.2007.05.014
- Gannoun, A., Burton, K.W., Thomas, L.E., Parkinson, I.J., Calsteren, P. van, Schiano, P., 2004. Osmium Isotope Heterogeneity in the Constituent Phases of Mid-Ocean Ridge Basalts. *Science* 303, 70–72. doi:10.1126/science.1090266
- Gilbert, S., Danyushevsky, L., Robinson, P., Wohlgemuth-Ueberwasser, C., Pearson, N., Savard, D., Norman, M., Hanley, J., 2013. A Comparative Study of Five Reference Materials and the Lombard Meteorite for the Determination of the Platinum-Group Elements and Gold by LA-ICP-MS. *Geostand. Geoanalytical Res.* 37, 51–64. doi:10.1111/j.1751-908X.2012.00170.x
- Gilbert, S.E., Danyushevsky, L.V., Goemann, K., Death, D., 2014. Fractionation of sulphur relative to iron during laser ablation-ICP-MS analyses of sulphide minerals: implications for quantification. *J. Anal. At. Spectrom.* 29, 1024–1033. doi:10.1039/C4JA00012A
- Giuliani, A., Kamenetsky, V.S., Kendrick, M.A., Phillips, D., Goemann, K., 2013. Nickel-rich metasomatism of the lithospheric mantle by pre-kimberlitic alkali-S–Cl-rich C–O–H fluids. *Contrib. Mineral. Petrol.* 165, 155–171. doi:10.1007/s00410-012-0801-1
- Grégoire, M., Bell, D., Roex, A.L., 2002. Trace element geochemistry of phlogopite-rich mafic mantle xenoliths: their classification and their relationship to phlogopite-bearing peridotites and kimberlites revisited. *Contrib. Mineral. Petrol.* 142, 603–625. doi:10.1007/s00410-001-0315-8
- Griffin, W.L., Doyle, B.J., Ryan, C.G., Pearson, N.J., Suzanne, Y.O., Davies, R., Kivi, K., Van Achterbergh, E., Natapov, L.M., 1999. Layered Mantle Lithosphere in the Lac de Gras Area, Slave Craton: Composition, Structure and Origin. *J. Petrol.* 40, 705 – 727. doi:10.1093/ptroj/40.5.705
- Griffin, W.L., Graham, S., O'Reilly, S.Y., Pearson, N.J., 2004. Lithosphere evolution beneath the Kaapvaal Craton: Re-Os systematics of sulfides in mantle-derived peridotites. *Chem. Geol.* 208, 89–118. doi:10.1016/j.chemgeo.2004.04.007
- Griffin, W.L., O'Reilly, S.Y., Abe, N., Aulbach, S., Davies, R.M., Pearson, N.J., Doyle, B.J., Kivi, K., 2003. The origin and evolution of Archean lithospheric mantle. *Precambrian Res.* 127, 19–41. doi:10.1016/S0301-9268(03)00180-3
- Griffin, W.L., Spetsius, Z.V., Pearson, N.J., O'Reilly, S.Y., 2002. In situ Re-Os analysis of sulfide inclusions in kimberlitic olivine: New constraints on depletion events in the Siberian lithospheric mantle. *Geochem. Geophys. Geosystems* 3, 1–25. doi:10.1029/2001GC000287

- Haggerty, S.E., Sautter, V., 1990. Ultradeep (Greater Than 300 Kilometers), Ultramafic Upper Mantle Xenoliths. *Science* 248, 993–996. doi:10.1126/science.248.4958.993
- Halls, H., 2014. Crustal shortening during the Paleoproterozoic: Can it be accommodated by paleomagnetic data? *Precambrian Res.*, *Precambrian Supercontinents* 244, 42–52. doi:10.1016/j.precamres.2013.09.005
- Hanghøj, K., Kelemen, P.B., Hassler, D., Godard, M., 2010. Composition and Genesis of Depleted Mantle Peridotites from the Wadi Tayin Massif, Oman Ophiolite; Major and Trace Element Geochemistry, and Os Isotope and PGE Systematics. *J. Petrol.* 51, 201–227. doi:10.1093/petrology/egp077
- Hanmer, S., Tella, S., Ryan, J.J., Sandeman, H.A., Berman, R.G., 2006. Late Neoproterozoic thick-skinned thrusting and Paleoproterozoic reworking in the MacQuoid supracrustal belt and Cross Bay plutonic complex, western Churchill Province, Nunavut, Canada. *Precambrian Res.* 144, 126–139. doi:10.1016/j.precamres.2005.10.005
- Harte, B., 1977. Rock Nomenclature with Particular Relation to Deformation and Recrystallisation Textures in Olivine-Bearing Xenoliths. *J. Geol.* 85, 279–288.
- Hartlaub, R.P., Chacko, T., Heaman, L.M., Creaser, R.A., Ashton, K.E., Simonetti, A., 2005. Ancient (Meso- to Paleoproterozoic) crust in the Rae Province, Canada: Evidence from Sm–Nd and U–Pb constraints. *Precambrian Res.* 141, 137–153. doi:10.1016/j.precamres.2005.09.001
- Hartlaub, R.P., Heaman, L.M., Ashton, K.E., Chacko, T., 2004. The Archean Murmac Bay Group: evidence for a giant Archean rift in the Rae Province, Canada. *Precambrian Res.* 131, 345–372. doi:10.1016/j.precamres.2004.01.001
- Hartlaub, R.P., Heaman, L.M., Chacko, T., Ashton, K.E., 2007. Circa 2.3-Ga Magmatism of the Arrowsmith Orogeny, Uranium City Region, Western Churchill Craton, Canada. *J. Geol.* 115, 181–195.
- Hart, S.R., Gaetani, G.A., 2006. Mantle Pb paradoxes: the sulfide solution. *Contrib. Mineral. Petrol.* 152, 295–308. doi:10.1007/s00410-006-0108-1
- Hart, S.R., Ravizza, G.E., 1996. Os Partitioning Between Phases in Lherzolite and Basalt, in: Basu, A., Hart, S. (Eds.), *Earth Processes: Reading the Isotopic Code*. American Geophysical Union, pp. 123–134.
- Harvey, J., Dale, C.W., Gannoun, A., Burton, K.W., 2011. Osmium mass balance in peridotite and the effects of mantle-derived sulphides on basalt petrogenesis. *Geochim. Cosmochim. Acta* 75, 5574–5596. doi:10.1016/j.gca.2011.07.001
- Harvey, J., Gannoun, A., Burton, K.W., Rogers, N.W., Alard, O., Parkinson, I.J., 2006. Ancient melt extraction from the oceanic upper mantle revealed by Re–Os isotopes

- in abyssal peridotites from the Mid-Atlantic ridge. *Earth Planet. Sci. Lett.* 244, 606–621. doi:10.1016/j.epsl.2006.02.031
- Harvey, J., Gannoun, A., Burton, K.W., Schiano, P., Rogers, N.W., Alard, O., 2010. Unravelling the effects of melt depletion and secondary infiltration on mantle Re–Os isotopes beneath the French Massif Central. *Geochim. Cosmochim. Acta* 74, 293–320. doi:10.1016/j.gca.2009.09.031
- Haughton, D.R., Roeder, P.L., Skinner, B.J., 1974. Solubility of Sulfur in Mafic Magmas. *Econ. Geol.* 69, 451–467. doi:10.2113/gsecongeo.69.4.451
- Heaman, L.M., 1989. The nature of the subcontinental mantle from SrNdPb isotopic studies on kimberlitic perovskite. *Earth Planet. Sci. Lett.* 92, 323–334. doi:10.1016/0012-821X(89)90057-5
- Heaman, L.M., Pearson, D.G., 2010. Nature and evolution of the Slave Province subcontinental lithospheric mantle. *Can. J. Earth Sci.* 47, 369–388. doi:10.1139/E09-046
- Helmstaedt, H., 2009. Crust-mantle coupling revisited: The Archean Slave craton, NWT, Canada. *Lithos* 112, 1055–1068. doi:10.1016/j.lithos.2009.04.046
- Helmy, H.M., Ballhaus, C., Fonseca, R.O.C., Wirth, R., Nagel, T., Tredoux, M., 2013. Noble metal nanoclusters and nanoparticles precede mineral formation in magmatic sulphide melts. *Nat. Commun.* 4. doi:10.1038/ncomms3405
- Herwartz, D., Pack, A., Friedrichs, B., Bischoff, A., 2014. Identification of the giant impactor Theia in lunar rocks. *Science* 344, 1146–1150. doi:10.1126/science.1251117
- Herzberg, C., 2004. Geodynamic Information in Peridotite Petrology. *J. Petrol.* 45, 2507–2530. doi:10.1093/petrology/egh039
- Herzberg, C., O'hara, M.J., 2002. Plume-Associated Ultramafic Magmas of Phanerozoic Age. *J. Petrol.* 43, 1857–1883. doi:10.1093/petrology/43.10.1857
- Herzberg, C., Rudnick, R., 2012. Formation of cratonic lithosphere: An integrated thermal and petrological model. *Lithos* 149, 4–15. doi:10.1016/j.lithos.2012.01.010
- Hoffman, P.F., 1989. Precambrian geology and tectonic history of North America, in: *The Geology of North America—an Overview*. Geol. Soc. Am., pp. 447–512.
- Hoffman, P.F., 1988. United Plates of America, The Birth of a Craton: Early Proterozoic Assembly and Growth of Laurentia. *Annu. Rev. Earth Planet. Sci.* 16, 543–603. doi:10.1146/annurev.ea.16.050188.002551
- Hollings, P., Ansdell, K., 2002. Paleoproterozoic arc magmatism imposed on an older backarc basin: Implications for the tectonic evolution of the Trans-Hudson orogen, Canada. *Geol. Soc. Am. Bull.* 114, 153–168. doi:10.1130/0016-7606

- Holzheid, A., Sylvester, P., O'Neill, H.S.C., Rubie, D.C., Palme, H., 2000. Evidence for a late chondritic veneer in the Earth's mantle from high-pressure partitioning of palladium and platinum. *Nature* 406, 396–399. doi:10.1038/35019050
- Hu, Z., Qi, L., 2014. 15.5 - Sample Digestion Methods, in: Turekian, H.D.H.K. (Ed.), *Treatise on Geochemistry (Second Edition)*. Elsevier, Oxford, pp. 87–109.
- Ionov, D.A., Bodinier, J.-L., Mukasa, S.B., Zanetti, A., 2002. Mechanisms and Sources of Mantle Metasomatism: Major and Trace Element Compositions of Peridotite Xenoliths from Spitsbergen in the Context of Numerical Modelling. *J. Petrol.* 43, 2219–2259. doi:10.1093/petrology/43.12.2219
- Ionov, D.A., Shirey, S.B., Weis, D., Brüggmann, G., 2006. Os–Hf–Sr–Nd isotope and PGE systematics of spinel peridotite xenoliths from Tok, SE Siberian craton: Effects of pervasive metasomatism in shallow refractory mantle. *Earth Planet. Sci. Lett.* 241, 47–64. doi:10.1016/j.epsl.2005.10.038
- Irvine, G.J., 2001. Time constraints on the formation of lithospheric mantle beneath cratons: a Re-Os isotope and platinum group element study of peridotite xenoliths from northern Canada and Lesotho (Thesis). University of Durham.
- Irvine, G.J., Kopylova, M.G., Carlson, R.W., Pearson, D.G., Shirey, S.B., Kjarsgaard, B.A., 1999. Age of the Lithospheric Mantle Beneath and Around the Slave Craton: A Rhenium-Osmium-Isotopic Study of Peridotite Xenoliths from the Jericho and Somerset Island Kimberlites. Presented at the Ninth Annual V. M. Goldschmidt Conference, p. 7229.
- Irvine, G.J., Pearson, D.G., Kjarsgaard, B.A., Carlson, R.W., Kopylova, M.G., Dreibus, G., 2003. A Re-Os isotope and PGE study of kimberlite-derived peridotite xenoliths from Somerset Island and a comparison to the Slave and Kaapvaal cratons. *Lithos* 71, 461–488. doi:10.1016/S0024-4937(03)00126-9
- Jackson, I., 2000. *The Earth's mantle: composition, structure, and evolution*. Cambridge University Press.
- Jacobson, S.A., Morbidelli, A., Raymond, S.N., O'Brien, D.P., Walsh, K.J., Rubie, D.C., 2014. Highly siderophile elements in Earth's mantle as a clock for the Moon-forming impact. *Nature* 508, 84–87. doi:10.1038/nature13172
- Jenner, F.E., O'Neill, H.S.C., Arculus, R.J., Mavrogenes, J.A., 2010. The Magnetite Crisis in the Evolution of Arc-related Magmas and the Initial Concentration of Au, Ag and Cu. *J. Petrol.* 51, 2445–2464. doi:10.1093/petrology/egq063
- Jones, A.G., Lezaeta, P., Ferguson, I.J., Chave, A.D., Evans, R.L., Garcia, X., Spratt, J., 2003. The electrical structure of the Slave craton. *Lithos, A Tale of Two Cratons: The Slave-Kaapvaal Workshop* 71, 505–527. doi:10.1016/j.lithos.2003.08.001

- Jordan, T.H., 1978. Composition and development of the continental tectosphere. *Nature* 274, 544–548. doi:10.1038/274544a0
- Keays, R.R., Sewell, D.K.B., Mitchell, R.H., 1981. Platinum and palladium minerals in upper mantle-derived lherzolites. *Nature* 294, 646–648. doi:10.1038/294646a0
- Kimura, K., Lewis, R.S., Anders, E., 1974. Distribution of gold and rhenium between nickel-iron and silicate melts: implications for the abundance of siderophile elements on the Earth and Moon. *Geochim. Cosmochim. Acta* 38, 683–701. doi:10.1016/0016-7037(74)90144-6
- Kitsul, V.I., Glebovitsky, V.A., Vapnik, Y.A., Frisch, T., 2000. Gneisses from the Granulite Terrane of the Central Boothia Uplift, Arctic Canada. *Can. Mineral.* 38, 443–454. doi:10.2113/gscanmin.38.2.443
- Kjarsgaard, B.A., Peterson, T.D., 1992. Kimberlite - Derived Ultramafic Xenoliths From the Diamond Stability Field: a New Cretaceous Geotherm For Somerset Island, Northwest Territories (No. 92-1B), Current Research, Part B, Interior Plains and Arctic Canada. Geological Survey Of Canada.
- Klein, F., Bach, W., 2009. Fe–Ni–Co–O–S Phase Relations in Peridotite–Seawater Interactions. *J. Petrol.* 50, 37–59. doi:10.1093/petrology/egn071
- Kopylova, M.G., Caro, G., 2004. Mantle Xenoliths from the Southeastern Slave Craton: Evidence for Chemical Zonation in a Thick, Cold Lithosphere. *J. Petrol.* 45, 1045 – 1067. doi:10.1093/petrology/egh003
- Lassiter, J.C., 2003. Rhenium volatility in subaerial lavas: constraints from subaerial and submarine portions of the HSDP-2 Mauna Kea drillcore. *Earth Planet. Sci. Lett.* 214, 311–325. doi:10.1016/S0012-821X(03)00385-6
- Laurenz, V., Fonseca, R.O.C., Ballhaus, C., Sylvester, P.J., 2010. Solubility of palladium in picritic melts: 1. The effect of iron. *Geochim. Cosmochim. Acta* 74, 2989–2998. doi:10.1016/j.gca.2010.02.015
- Lecheminant, A.N., Roddick, J.C., 1991. U - Pb Zircon Evidence For Widespread 2.6 Ga Felsic Magmatism in the Central District of Keewatin, N.w.t. (No. 90-2). Geological Survey of Canada.
- Lee, C.-T.A., 2006. Geochemical/Petrologic Constraints on the Origin of Cratonic Mantle, in: Benn, K., Jean-Claudereschal, Condie, K.C. (Eds.), *Archean Geodynamics and Environments*. American Geophysical Union, pp. 89–114.
- Lee, C.-T.A., 2002. Platinum-group element geochemistry of peridotite xenoliths from the Sierra Nevada and the Basin and Range, California. *Geochim. Cosmochim. Acta* 66, 3987–4005. doi:10.1016/S0016-7037(02)00960-2

- Lee, C.-T.A., Luffi, P., Chin, E.J., 2011. Building and Destroying Continental Mantle. *Annu. Rev. Earth Planet. Sci.* 39, 59–90. doi:10.1146/annurev-earth-040610-133505
- Li, C., Ripley, E.M., 2009. Sulfur Contents at Sulfide-Liquid or Anhydrite Saturation in Silicate Melts: Empirical Equations and Example Applications. *Econ. Geol.* 104, 405–412. doi:10.2113/gsecongeo.104.3.405
- Lissner, M., König, S., Luguët, A., le Roux, P.J., Schuth, S., Heuser, A., le Roex, A.P., 2014. Selenium and tellurium systematics in MORBs from the southern Mid-Atlantic Ridge (47–50°S). *Geochim. Cosmochim. Acta* 144, 379–402. doi:10.1016/j.gca.2014.08.023
- Liu, Y., Brenan, J., 2015. Partitioning of platinum-group elements (PGE) and chalcogens (Se, Te, As, Sb, Bi) between monosulfide-solid solution (MSS), intermediate solid solution (ISS) and sulfide liquid at controlled fO<sub>2</sub>–fS<sub>2</sub> conditions. *Geochim. Cosmochim. Acta* 159, 139–161. doi:10.1016/j.gca.2015.03.021
- Lodders, K., 2003. Solar System Abundances and Condensation Temperatures of the Elements. *Astrophys. J.* 591, 1220. doi:10.1086/375492
- Lorand, D.J.P., 1985. The behaviour of the upper mantle sulfide component during the incipient alteration of “Alpine”-type peridotites as illustrated by the Beni Bousera (northern Morocco) and Ronda (southern Spain) ultramafic bodies. *Tschermaks Mineral. Petrogr. Mitteilungen* 34, 183–209. doi:10.1007/BF01082961
- Lorand, J.-P., Alard, O., 2001. Platinum-group element abundances in the upper mantle: new constraints from in situ and whole-rock analyses of Massif Central xenoliths (France). *Geochim. Cosmochim. Acta* 65, 2789–2806. doi:10.1016/S0016-7037(01)00627-5
- Lorand, J.-P., Alard, O., Luguët, A., 2010. Platinum-group element micronuggets and refertilization process in Lherz orogenic peridotite (northeastern Pyrenees, France). *Earth Planet. Sci. Lett.* 289, 298–310. doi:10.1016/j.epsl.2009.11.017
- Lorand, J.-P., Delpèch, G., Grégoire, M., Moine, B., O’Reilly, S.Y., Cottin, J.-Y., 2004. Platinum-group elements and the multistage metasomatic history of Kerguelen lithospheric mantle (South Indian Ocean). *Chem. Geol., Highly Siderophile Element Behavior in High Temperature Processes* 208, 195–215. doi:10.1016/j.chemgeo.2004.04.012
- Lorand, J.-P., Grégoire, M., 2006. Petrogenesis of base metal sulphide assemblages of some peridotites from the Kaapvaal craton (South Africa). *Contrib. Mineral. Petrol.* 151, 521–538. doi:10.1007/s00410-006-0074-7
- Lorand, J.-P., Luguët, A., Alard, O., 2013. Platinum-group element systematics and petrogenetic processing of the continental upper mantle: A review. *Lithos, Ore*

- deposits and the role of the lithospheric mantle 164–167, 2–21.  
doi:10.1016/j.lithos.2012.08.017
- Lorand, J.-P., Luguet, A., Alard, O., 2008a. Platinum-Group Elements: A New Set of Key Tracers for the Earth's Interior. *Elements* 4, 247–252.  
doi:10.2113/GSELEMENTS.4.4.247
- Lorand, J.-P., Luguet, A., Alard, O., Bezos, A., Meisel, T., 2008b. Abundance and distribution of platinum-group elements in orogenic lherzolites; a case study in a Fontete Rouge lherzolite (French Pyrénées). *Chem. Geol.* 248, 174–194.  
doi:10.1016/j.chemgeo.2007.06.030
- Lorand, J.-P., Reisberg, L., Bedini, R.M., 2003. Platinum-group elements and melt percolation processes in Sidamo spinel peridotite xenoliths, Ethiopia, East African Rift. *Chem. Geol., Highly Siderophile elements in the Earth and Meteorites: A volume in honor of John Morgan 196*, 57–75. doi:10.1016/S0009-2541(02)00407-2
- Ludwig, K.R., 2003. User's manual for Isoplot 3.00: a geochronological toolkit for Microsoft Excel. Kenneth R. Ludwig.
- Luguet, A., Alard, O., Lorand, J.-P., Pearson, N.J., Ryan, C., O'Reilly, S.Y., 2001. Laser-ablation microprobe (LAM)-ICPMS unravels the highly siderophile element geochemistry of the oceanic mantle. *Earth Planet. Sci. Lett.* 189, 285–294.  
doi:10.1016/S0012-821X(01)00357-0
- Luguet, A., Behrens, M., Pearson, D.G., König, S., Herwartz, D., 2015. Significance of the whole rock Re–Os ages in cryptically and modally metasomatised cratonic peridotites: Constraints from HSE–Se–Te systematics. *Geochim. Cosmochim. Acta* 164, 441–463. doi:10.1016/j.gca.2015.06.016
- Luguet, A., Jaques, A.L., Pearson, D.G., Smith, C.B., Bulanova, G.P., Roffey, S.L., Rayner, M.J., Lorand, J.-P., 2009. An integrated petrological, geochemical and Re–Os isotope study of peridotite xenoliths from the Argyle lamproite, Western Australia and implications for cratonic diamond occurrences. *Lithos* 112, Supplement 2, 1096–1108. doi:10.1016/j.lithos.2009.05.022
- Luguet, A., Lorand, J.-P., Alard, O., Cottin, J.-Y., 2004. A multi-technique study of platinum group element systematic in some Ligurian ophiolitic peridotites, Italy. *Chem. Geol.* 208, 175–194. doi:10.1016/j.chemgeo.2004.04.011
- Luguet, A., Lorand, J.-P., Seyler, M., 2003. Sulfide petrology and highly siderophile element geochemistry of abyssal peridotites: a coupled study of samples from the Kane Fracture Zone (45°W 23°20N, MARK area, Atlantic Ocean). *Geochim. Cosmochim. Acta* 67, 1553–1570. doi:10.1016/S0016-7037(02)01133-X
- Luguet, A., Nowell, G.M., Pearson, D.G., 2008.  $^{184}\text{Os}/^{188}\text{Os}$  and  $^{186}\text{Os}/^{188}\text{Os}$  measurements by Negative Thermal Ionisation Mass Spectrometry (N-TIMS):

- Effects of interfering element and mass fractionation corrections on data accuracy and precision. *Chem. Geol.* 248, 342–362. doi:16/j.chemgeo.2007.10.013
- Luguet, A., Shirey, S.B., Lorand, J.-P., Horan, M.F., Carlson, R.W., 2007. Residual platinum-group minerals from highly depleted harzburgites of the Lherz massif (France) and their role in HSE fractionation of the mantle. *Geochim. Cosmochim. Acta* 71, 3082–3097. doi:16/j.gca.2007.04.011
- Maier, W.D., Barnes, S.J., Campbell, I.H., Fiorentini, M.L., Peltonen, P., Barnes, S.-J., Smithies, R.H., 2009. Progressive mixing of meteoritic veneer into the early Earth's deep mantle. *Nature* 460, 620–623. doi:10.1038/nature08205
- Maier, W.D., Peltonen, P., McDonald, I., Barnes, S.J., Barnes, S.-J., Hatton, C., Viljoen, F., 2012. The concentration of platinum-group elements and gold in southern African and Karelian kimberlite-hosted mantle xenoliths: Implications for the noble metal content of the Earth's mantle. *Chem. Geol., Behaviour of chalcophile and siderophile elements in magmatic systems: Papers presented at the 11th International Platinum Symposium* 302–303, 119–135. doi:10.1016/j.chemgeo.2011.06.014
- Makovicky, M., Makovicky, E., Rose-Hansen, J., 1986. Experimental studies on the solubility and distribution of platinum group elements in base-metal sulphides in platinum deposits. *Metallog. Basic Ultrabasic Rocks* 415–425.
- Mallmann, G., O'Neill, H.S.C., 2007. The effect of oxygen fugacity on the partitioning of Re between crystals and silicate melt during mantle melting. *Geochim. Cosmochim. Acta* 71, 2837–2857. doi:10.1016/j.gca.2007.03.028
- Marchesi, C., Dale, C.W., Garrido, C.J., Pearson, D.G., Bosch, D., Bodinier, J.-L., Gervilla, F., Hidas, K., 2014. Fractionation of highly siderophile elements in refertilized mantle: Implications for the Os isotope composition of basalts. *Earth Planet. Sci. Lett.* 400, 33–44. doi:10.1016/j.epsl.2014.05.025
- Mather, K.A., Pearson, D.G., McKenzie, D., Kjarsgaard, B.A., Priestley, K., 2011. Constraints on the depth and thermal history of cratonic lithosphere from peridotite xenoliths, xenocrysts and seismology. *Lithos* 125, 729–742. doi:10.1016/j.lithos.2011.04.003
- Mathez, E.A., 1976. Sulfur solubility and magmatic sulfides in submarine basalt glass. *J. Geophys. Res.* 81, 4269–4276. doi:10.1029/JB081i023p04269
- Mavrogenes, J.A., O'Neill, H.S.C., 1999. The relative effects of pressure, temperature and oxygen fugacity on the solubility of sulfide in mafic magmas. *Geochim. Cosmochim. Acta* 63, 1173–1180. doi:10.1016/S0016-7037(98)00289-0
- McDonough, W.F., Sun, S. -s., 1995. The composition of the Earth. *Chem. Geol., Chemical Evolution of the Mantle* 120, 223–253. doi:10.1016/0009-2541(94)00140-4

- McSween Jr, H.Y., Huss, G.R., 2010. *Cosmochemistry*. Cambridge University Press.
- Meisel, T., Reisberg, L., Moser, J., Carignan, J., Melcher, F., Brüggmann, G., 2003. Re-Os systematics of UB-N, a serpentinized peridotite reference material. *Chem. Geol.* 201, 161–179. doi:10.1016/S0009-2541(03)00234-1
- Meisel, T., Walker, R.J., Irving, A.J., Lorand, J.-P., 2001. Osmium isotopic compositions of mantle xenoliths: a global perspective. *Geochim. Cosmochim. Acta* 65, 1311–1323. doi:10.1016/S0016-7037(00)00566-4
- Meisel, T., Walker, R.J., Morgan, J.W., 1996. The osmium isotopic composition of the Earth's primitive upper mantle. *Nature* 383, 517–520. doi:10.1038/383517a0
- Menzies, A., Westerlund, K., Grütter, H., Gurney, J., Carlson, J., Fung, A., Nowicki, T., 2004. Peridotitic mantle xenoliths from kimberlites on the Ekati Diamond Mine property, N.W.T., Canada: major element compositions and implications for the lithosphere beneath the central Slave craton. *Lithos* 77, 395–412. doi:10.1016/j.lithos.2004.04.013
- Misra, K.C., Anand, M., Taylor, L.A., Sobolev, N.V., 2003. Multi-stage metasomatism of diamondiferous eclogite xenoliths from the Udachnaya kimberlite pipe, Yakutia, Siberia. *Contrib. Mineral. Petrol.* 146, 696–714. doi:10.1007/s00410-003-0529-z
- Mitchell, R.H., 1978. Garnet lherzolites from Somerset Island, Canada and aspects of the nature of perturbed geotherms. *Contrib. Mineral. Petrol.* 67, 341–347. doi:10.1007/BF00383294
- Mitchell, R.H., 1977. Ultramafic xenoliths from the Elwin Bay kimberlite: the first Canadian paleogeotherm. *Can. J. Earth Sci.* 14, 1202–1210. doi:10.1139/e77-110
- Mitchell, R.H., 1975. Geology, Magnetic Expression, and Structural Control of the Central Somerset Island Kimberlites. *Can. J. Earth Sci.* 12, 757–764. doi:10.1139/e75-066
- Morbidelli, A., Marchi, S., Bottke, W.F., Kring, D.A., 2012. A sawtooth-like timeline for the first billion years of lunar bombardment. *Earth Planet. Sci. Lett.* 355–356, 144–151. doi:10.1016/j.epsl.2012.07.037
- Morgan, J.W., 1985. Osmium isotope constraints on Earth's late accretionary history. *Nature* 317, 703–705. doi:10.1038/317703a0
- Mundl, A., Ntaflou, T., Ackerman, L., Bizimis, M., Bjerg, E.A., Hauzenberger, C.A., 2014. Mesoproterozoic and Paleoproterozoic subcontinental lithospheric mantle domains beneath southern Patagonia: Isotopic evidence for its connection to Africa and Antarctica. *Geology* G36344.1. doi:10.1130/G36344.1
- Mungall, J.E., Brenan, J.M., 2014. Partitioning of platinum-group elements and Au between sulfide liquid and basalt and the origins of mantle-crust fractionation of the

- chalcophile elements. *Geochim. Cosmochim. Acta* 125, 265–289.  
doi:10.1016/j.gca.2013.10.002
- Mungall, J.E., Su, S., 2005. Interfacial tension between magmatic sulfide and silicate liquids: Constraints on kinetics of sulfide liquation and sulfide migration through silicate rocks. *Earth Planet. Sci. Lett.* 234, 135–149. doi:10.1016/j.epsl.2005.02.035
- Nadeau, L., Ryan, J.J., Brouillette, P., James, D.T., 2008. Mineral assay results for the 2005 and 2007 field seasons, Boothia mainland area, Kitikmeot region, Nunavut (No. 5907).
- Nickel, K.G., Green, D.H., 1985. Empirical geothermobarometry for garnet peridotites and implications for the nature of the lithosphere, kimberlites and diamonds. *Earth Planet. Sci. Lett.* 73, 158–170. doi:10.1016/0012-821X(85)90043-3
- Nicolaysen, L.O., 1961. Graphic Interpretation of Discordant Age Measurements on Metamorphic Rocks. *Ann. N. Y. Acad. Sci.* 91, 198–206.  
doi:10.1111/j.1749-6632.1961.tb35452.x
- Nimis, P., Grütter, H., 2012. Discussion of “The applicability of garnet–orthopyroxene geobarometry in mantle xenoliths”, by Wu C.-M. and Zhao G. (*Lithos*, v. 125, p. 1–9). *Lithos* 142–143, 285–287. doi:10.1016/j.lithos.2011.09.006
- Nimis, P., Grütter, H., 2010. Internally consistent geothermometers for garnet peridotites and pyroxenites. *Contrib. Mineral. Petrol.* 159, 411–427. doi:10.1007/s00410-009-0455-9
- Nowell, G.M., Pearson, D.G., Parman, S.W., Luguet, A., Hanski, E., 2008. Precise and accurate 186Os/188Os and 187Os/188Os measurements by Multi-collector Plasma Ionisation Mass Spectrometry, part II: Laser ablation and its application to single-grain Pt-Os and Re-Os geochronology. *Chem. Geol.* 248, 394–426.  
doi:10.1016/j.chemgeo.2007.12.004
- O’Hara, M.J., Saunders, M.J., Mercy, E.L.P., 1975. Garnet-peridotite, primary ultrabasic magma and eclogite; Interpretation of upper mantle processes in kimberlite. *Phys. Chem. Earth* 9, 571–604. doi:10.1016/0079-1946(75)90040-3
- O’Neill, H.S.C., Dingwell, D.B., Borisov, A., Spettel, B., Palme, H., 1995. Experimental petrochemistry of some highly siderophile elements at high temperatures, and some implications for core formation and the mantle’s early history. *Chem. Geol., Chemical Evolution of the Mantle* 120, 255–273.  
doi:10.1016/0009-2541(94)00141-T
- O’Reilly, S.Y., Griffin, W.L., 2013. Mantle Metasomatism, in: *Metasomatism and the Chemical Transformation of Rock*, Lecture Notes in Earth System Sciences. Springer Berlin Heidelberg, pp. 471–533.

- Palme, H., Lodders, K., Jones, A., 2014. 2.2 - Solar System Abundances of the Elements, in: Turekian, H.D.H.K. (Ed.), *Treatise on Geochemistry (Second Edition)*. Elsevier, Oxford, pp. 15–36.
- Parrish, R.R., Reichenbach, I., 1991. Age of xenocrystic zircon from diatremes of western Canada. *Can. J. Earth Sci.* 28, 1232–1238. doi:10.1139/e91-110
- Patten, C., Barnes, S.-J., Mathez, E.A., 2012. Textural Variations in Morb Sulfide Droplets Due to Differences in Crystallization History. *Can. Mineral.* 50, 675–692. doi:10.3749/canmin.50.3.675
- Patten, C., Barnes, S.-J., Mathez, E.A., Jenner, F.E., 2013. Partition coefficients of chalcophile elements between sulfide and silicate melts and the early crystallization history of sulfide liquid: LA-ICP-MS analysis of MORB sulfide droplets. *Chem. Geol.* 358, 170–188. doi:10.1016/j.chemgeo.2013.08.040
- Peach, C.L., Mathez, E.A., Keays, R.R., 1990. Sulfide melt-silicate melt distribution coefficients for noble metals and other chalcophile elements as deduced from MORB: Implications for partial melting. *Geochim. Cosmochim. Acta* 54, 3379–3389. doi:10.1016/0016-7037(90)90292-S
- Pearson, D.G., 1999. The age of continental roots. *Lithos* 48, 171–194. doi:16/S0024-4937(99)00026-2
- Pearson, D.G., Carlson, R.W., Shirey, S.B., Boyd, F.R., Nixon, P.H., 1995a. Stabilisation of Archaean lithospheric mantle: A Re-Os isotope study of peridotite xenoliths from the Kaapvaal craton. *Earth Planet. Sci. Lett.* 134, 341–357. doi:10.1016/0012-821X(95)00125-V
- Pearson, D.G., Irvine, G.J., Ionov, D.A., Boyd, F.R., Dreibus, G.E., 2004. Re-Os isotope systematics and platinum group element fractionation during mantle melt extraction: a study of massif and xenolith peridotite suites. *Chem. Geol.* 208, 29–59. doi:16/j.chemgeo.2004.04.005
- Pearson, D.G., Parman, S.W., Nowell, G.M., 2007. A link between large mantle melting events and continent growth seen in osmium isotopes. *Nature* 449, 202–205. doi:10.1038/nature06122
- Pearson, D.G., Shirey, S.B., Carlson, R.W., Boyd, F.R., Pokhilenko, N.P., Shimizu, N., 1995b. Re-Os, Sm-Nd, and Rb-Sr isotope evidence for thick Archaean lithospheric mantle beneath the Siberian craton modified by multistage metasomatism. *Geochim. Cosmochim. Acta* 59, 959–977. doi:10.1016/0016-7037(95)00014-3
- Pearson, D.G., Shirey, S.B., Harris, J.W., Carlson, R.W., 1998. Sulphide inclusions in diamonds from the Koffiefontein kimberlite, S Africa: constraints on diamond ages and mantle Re-Os systematics. *Earth Planet. Sci. Lett.* 160, 311–326. doi:10.1016/S0012-821X(98)00092-2

- Pearson, D.G., Wittig, N., 2008. Formation of Archaean continental lithosphere and its diamonds: the root of the problem. *J. Geol. Soc.* 165, 895–914. doi:10.1144/0016-76492008-003
- Pearson, D.G., Woodland, S.J., 2000. Solvent extraction/anion exchange separation and determination of PGEs (Os, Ir, Pt, Pd, Ru) and Re-Os isotopes in geological samples by isotope dilution ICP-MS. *Chem. Geol.* 165, 87–107. doi:10.1016/S0009-2541(99)00161-8
- Pearson, N.J., Alard, O., Griffin, W.L., Jackson, S.E., O'Reilly, S.Y., 2002. In situ measurement of Re-Os isotopes in mantle sulfides by laser ablation multicollector-inductively coupled plasma mass spectrometry: analytical methods and preliminary results. *Geochim. Cosmochim. Acta* 66, 1037–1050. doi:10.1016/S0016-7037(01)00823-7
- Pehrsson, S.J., Berman, R.G., Eglington, B., Rainbird, R., 2013. Two Neoproterozoic supercontinents revisited: The case for a Rae family of cratons. *Precambrian Res.* 232, 27–43. doi:10.1016/j.precamres.2013.02.005
- Peregoedova, A., Barnes, S.-J., Baker, D.R., 2004. The formation of Pt–Ir alloys and Cu–Pd-rich sulfide melts by partial desulfurization of Fe–Ni–Cu sulfides: results of experiments and implications for natural systems. *Chem. Geol.* 208, 247–264. doi:10.1016/j.chemgeo.2004.04.015
- Peucker-Ehrenbrink, B., Hanghoj, K., Atwood, T., Kelemen, P.B., 2012. Rhenium-osmium isotope systematics and platinum group element concentrations in oceanic crust. *Geology* 40, 199–202. doi:10.1130/G32431.1
- Rehkämper, M., Halliday, A.N., Fitton, J.G., Lee, D.-C., Wieneke, M., Arndt, N.T., 1999. Ir, Ru, Pt, and Pd in basalts and komatiites: new constraints for the geochemical behavior of the platinum-group elements in the mantle. *Geochim. Cosmochim. Acta* 63, 3915–3934. doi:10.1016/S0016-7037(99)00219-7
- Reisberg, L., Meisel, T., 2002. The Re-Os Isotopic System: A Review of Analytical Techniques. *Geostand. Newsl.* 26, 249–267. doi:10.1111/j.1751-908X.2002.tb00633.x
- Reisberg, L., Zhi, X., Lorand, J.-P., Wagner, C., Peng, Z., Zimmermann, C., 2005. Re–Os and S systematics of spinel peridotite xenoliths from east central China: Evidence for contrasting effects of melt percolation. *Earth Planet. Sci. Lett.* 239, 286–308. doi:10.1016/j.epsl.2005.09.010
- Richardson, S.H., Shirey, S.B., Harris, J.W., Carlson, R.W., 2001. Archean subduction recorded by Re–Os isotopes in eclogitic sulfide inclusions in Kimberley diamonds. *Earth Planet. Sci. Lett.* 191, 257–266. doi:10.1016/S0012-821X(01)00419-8

- Rollinson, H., 2010. Coupled evolution of Archean continental crust and subcontinental lithospheric mantle. *Geology* 38, 1083–1086. doi:10.1130/G31159.1
- Rudnick, R.L., Gao, S., 2014. 4.1 - Composition of the Continental Crust, in: Turekian, H.D.H.K. (Ed.), *Treatise on Geochemistry (Second Edition)*. Elsevier, Oxford, pp. 1–51.
- Rudnick, R.L., Walker, R.J., 2009. Interpreting ages from Re-Os isotopes in peridotites. *Lithos* 112, 1083–1095. doi:16/j.lithos.2009.04.042
- Ryan, J.J., Nadeau, L., Hinchey, A.M., James, D.T., Sandeman, H.A., Schetselaar, E.M., Davis, W.J., Berman, R.G., 2009. Bedrock geology of the southern Boothia mainland area (Pelly Bay-Rae Strait-Spence Bay map areas), Kitikmeot region, Nunavut (No. 2009-1). Geological Survey of Canada.
- Saha, A., Basu, A.R., Jacobsen, S.B., Poreda, R.J., Yin, Q.-Z., Yogodzinski, G.M., 2005. Slab devolatilization and Os and Pb mobility in the mantle wedge of the Kamchatka arc. *Earth Planet. Sci. Lett.* 236, 182–194. doi:10.1016/j.epsl.2005.05.018
- Sakakibara, N., Takahashi, Y., Okumura, K., Hattori, K.H., Yaita, T., Suzuki, K., Shimizu, H., 2005. Speciation of osmium in an iron meteorite and a platinum ore specimen based on X-ray absorption fine-structure spectroscopy. *Geochem. J.* 39, 383–389. doi:10.2343/geochemj.39.383
- Schetselaar, E.M., Ryan, J.J., 2009. Remote predictive mapping of the Boothia mainland area, Nunavut, Canada: an iterative approach using Landsat ETM, aeromagnetic, and geological field data. *Can. J. Remote Sens.* 35, S72–S94. doi:10.5589/m09-032
- Schiano, P., Birck, J.-L., Allègre, C.J., 1997. Osmium-strontium-neodymium-lead isotopic covariations in mid-ocean ridge basalt glasses and the heterogeneity of the upper mantle. *Earth Planet. Sci. Lett.* 150, 363–379. doi:10.1016/S0012-821X(97)00098-8
- Schmidberger, S.S., Francis, D., 2001. Constraints on the Trace Element Composition of the Archean Mantle Root beneath Somerset Island, Arctic Canada. *J. Petrol.* 42, 1095–1117. doi:10.1093/petrology/42.6.1095
- Schmidberger, S.S., Francis, D., 1999. Nature of the mantle roots beneath the North American craton: mantle xenolith evidence from Somerset Island kimberlites. *Lithos* 48, 195–216. doi:10.1016/S0024-4937(99)00029-8
- Schmidberger, S.S., Simonetti, A., Francis, D., 2003. Small-scale Sr isotope investigation of clinopyroxenes from peridotite xenoliths by laser ablation MC-ICP-MS—implications for mantle metasomatism. *Chem. Geol.* 199, 317–329. doi:10.1016/S0009-2541(03)00125-6
- Schmidberger, S.S., Simonetti, A., Francis, D., 2001. Sr-Nd-Pb isotope systematics of mantle xenoliths from Somerset Island kimberlites: Evidence for lithosphere

- stratification beneath Arctic Canada. *Geochim. Cosmochim. Acta* 65, 4243–4255. doi:10.1016/S0016-7037(01)00687-1
- Schmidberger, S.S., Simonetti, A., Francis, D., Gariépy, C., 2002. Probing Archean lithosphere using the Lu-Hf isotope systematics of peridotite xenoliths from Somerset Island kimberlites, Canada. *Earth Planet. Sci. Lett.* 197, 245–259. doi:10.1016/S0012-821X(02)00491-0
- Schubert, G., Turcotte, D.L., Olson, P., 2001. *Mantle Convection in the Earth and Planets 2 Volume Set*. Cambridge University Press.
- Sharygin, I.S., Golovin, A.V., Pokhilenko, N.P., 2012. Djerfisherite in xenoliths of sheared peridotite in the Udachnaya-East pipe (Yakutia): origin and relationship with kimberlitic magmatism. *Russ. Geol. Geophys.* 53, 247–261. doi:10.1016/j.rgg.2012.02.003
- Sharygin, V.V., Golovin, A.V., Pokhilenko, N.P., Kamenetsky, V.S., 2007. Djerfisherite in the Udachnaya-East pipe kimberlites (Sakha-Yakutia, Russia): paragenesis, composition and origin. *Eur. J. Mineral.* 19, 51–63. doi:10.1127/0935-1221/2007/0019-0051
- Shiga, Y., 1987. Behavior of iron, nickel, cobalt and sulfur during serpentinization, with reference to the Hayachine ultramafic rocks of the Kamaishi mining district, northeastern Japan. *Can. Mineral.* 25, 611–624.
- Shindo, K., Komuro, K., Hayashi, K., 2009. Sulfide minerals in mantle xenoliths from the Kurose reef, Fukuoka Prefecture, Japan. *J. Mineral. Petrol. Sci.* 104, 182–187. doi:10.2465/jmps.081022c
- Shirey, S.B., Walker, R.J., 1998. The Re-Os isotope system in cosmochemistry and high-temperature geochemistry. *Annu. Rev. Earth Planet. Sci.* 26, 423–500. doi:10.1146/annurev.earth.26.1.423
- Shirey, S.B., Walker, R.J., 1995. Carius Tube Digestion for Low-Blank Rhenium-Osmium Analysis. *Anal. Chem.* 67, 2136–2141. doi:10.1021/ac00109a036
- Simon, N.S.C., Carlson, R.W., Pearson, D.G., Davies, G.R., 2007. The Origin and Evolution of the Kaapvaal Cratonic Lithospheric Mantle. *J. Petrol.* 48, 589–625. doi:10.1093/petrology/egl074
- Simon, N.S.C., Irvine, G.J., Davies, G.R., Pearson, D.G., Carlson, R.W., 2003. The origin of garnet and clinopyroxene in “depleted” Kaapvaal peridotites. *Lithos, A Tale of Two Cratons: The Slave-Kaapvaal Workshop* 71, 289–322. doi:10.1016/S0024-4937(03)00118-X
- Skulski, T., Sandeman, H.A., MacHattie, T.G., Sanborn-Barrie, M., Rayner, N., Byrne, D., 2003. Tectonic setting of 2.73-2.7 Ga Prince Albert Group, Churchill Province, Nunavut. Presented at the GAC-MAC Joint Annual meeting, Vancouver.

- Smith, C.B., Allsopp, H.L., Garvie, O.G., Kramers, J.D., Jackson, P.F.S., Clement, C.R., 1989. Note on the U-Pb perovskite method for dating kimberlites: Examples from the Wesselton and De Beers mines, South Africa, and Somerset Island, Canada. *Chem. Geol. Isot. Geosci. Sect.* 79, 137–145. doi:10.1016/0168-9622(89)90016-X
- Smith, P.J., 1986. *The Earth*. Macmillan, New York.
- Smit, K.V., Pearson, D.G., Stachel, T., Seller, M., 2014. Peridotites from Attawapiskat, Canada: Mesoproterozoic Reworking of Palaeoarchaeon Lithospheric Mantle beneath the Northern Superior Superterrane. *J. Petrol.* 55, 1829–1863. doi:10.1093/petrology/egu043
- Smoliar, M.I., Walker, R.J., Morgan, J.W., 1996. Re-Os Ages of Group IIA, IIIA, IVA, and IVB Iron Meteorites. *Science* 271, 1099–1102. doi:10.1126/science.271.5252.1099
- Sparks, R.S.J., 2013. Kimberlite Volcanism. *Annu. Rev. Earth Planet. Sci.* 41, 497–528. doi:10.1146/annurev-earth-042711-105252
- Stachel, T., Harris, J.W., Tappert, R., Brey, G.P., 2003. Peridotitic diamonds from the Slave and the Kaapvaal cratons--similarities and differences based on a preliminary data set. *Lithos* 71, 489–503. doi:10.1016/S0024-4937(03)00127-0
- Stewart, W.D., 1987. Late Proterozoic to early Tertiary stratigraphy of Somerset Island and northern Boothia Peninsula, District of Franklin, N.W.T. Geological Survey of Canada.
- Sun, W., Bennett, V.C., Eggins, S.M., Kamenetsky, V.S., Arculus, R.J., 2003. Enhanced mantle-to-crust rhenium transfer in undegassed arc magmas. *Nature* 422, 294–297. doi:10.1038/nature01482
- Suzuki, K., Senda, R., Shimizu, K., 2011. Osmium behavior in a subduction system elucidated from chromian spinel in Bonin Island beach sands. *Geology* 39, 999–1002. doi:10.1130/G32044.1
- Tappe, S., Smart, K.A., Pearson, D.G., Steenfelt, A., Simonetti, A., 2011. Craton formation in Late Archean subduction zones revealed by first Greenland eclogites. *Geology* 39, 1103–1106. doi:10.1130/G32348.1
- Tatsumi, Y., Oguri, K., Shimoda, G., 1999. The behaviour of platinum-group elements during magmatic differentiation in Hawaiian tholeiites. *Geochem. J.* 33, 237–247. doi:10.2343/geochemj.33.237
- Taylor, W.R., 1998. An experimental test of some geothermometer and geobarometer formulations for upper mantle peridotites with application to the thermobarometry of fertile lherzolite and garnet websterite. *Neues Jahrb. Für Mineral. Abh.* 381–408.

- Tella, S., LeCheminant, A.N., Sanborn-Barrie, M., Venance, K.E., 1997. Geology, parts of MacQuoid Lake, District of Keewatin, Northwest Territories. Geol. Surv. Can. Open File Map 3404.
- Todolí, J.-L., Mermet, J.-M., 1999. Acid interferences in atomic spectrometry: analyte signal effects and subsequent reduction. *Spectrochim. Acta Part B At. Spectrosc.* 54, 895–929. doi:10.1016/S0584-8547(99)00041-5
- van Acken, D., Becker, H., Walker, R.J., 2008. Refertilization of Jurassic oceanic peridotites from the Tethys Ocean — Implications for the Re–Os systematics of the upper mantle. *Earth Planet. Sci. Lett.* 268, 171–181. doi:10.1016/j.epsl.2008.01.002
- Wainwright, A.N., Luguét, A., Fonseca, R.O.C., Pearson, D.G., 2015. Investigating metasomatic effects on the  $^{187}\text{Os}$  isotopic signature: A case study on micrometric base metal sulphides in metasomatised peridotite from the Letlhakane kimberlite (Botswana). *Lithos* 232, 35–48. doi:10.1016/j.lithos.2015.06.017
- Walker, R.J., Carlson, R.W., Shirey, S.B., F.R. B., 1989. Os, Sr, Nd, and Pb isotope systematics of southern African peridotite xenoliths: Implications for the chemical evolution of subcontinental mantle. *Geochim. Cosmochim. Acta* 53, 1583–1595. doi:10.1016/0016-7037(89)90240-8
- Walker, R.J., Horan, M.F., Morgan, J.W., Becker, H., Grossman, J.N., Rubin, A.E., 2002. Comparative  $^{187}\text{Re}$ - $^{187}\text{Os}$  systematics of chondrites: Implications regarding early solar system processes. *Geochim. Cosmochim. Acta* 66, 4187–4201. doi:10.1016/S0016-7037(02)01003-7
- Wallace, P., Carmichael, I.S.E., 1992. Sulfur in basaltic magmas. *Geochim. Cosmochim. Acta* 56, 1863–1874. doi:10.1016/0016-7037(92)90316-B
- Warren, J.M., Shirey, S.B., 2012. Lead and osmium isotopic constraints on the oceanic mantle from single abyssal peridotite sulfides. *Earth Planet. Sci. Lett.* 359–360, 279–293. doi:10.1016/j.epsl.2012.09.055
- Westerlund, K.J., Shirey, S.B., Richardson, S.H., Carlson, R.W., Gurney, J.J., Harris, J.W., 2006. A subduction wedge origin for Paleoproterozoic peridotitic diamonds and harzburgites from the Panda kimberlite, Slave craton: evidence from Re–Os isotope systematics. *Contrib. Mineral. Petrol.* 152, 275–294. doi:10.1007/s00410-006-0101-8
- Wiggers de Vries, D.F., Pearson, D.G., Bulanova, G.P., Smelov, A.P., Pavlushin, A.D., Davies, G.R., 2013. Re–Os dating of sulphide inclusions zonally distributed in single Yakutian diamonds: Evidence for multiple episodes of Proterozoic formation and protracted timescales of diamond growth. *Geochim. Cosmochim. Acta* 120, 363–394. doi:10.1016/j.gca.2013.06.035

- Willbold, M., Elliott, T., Moorbath, S., 2011. The tungsten isotopic composition of the Earth's mantle before the terminal bombardment. *Nature* 477, 195–198. doi:10.1038/nature10399
- Winter, J.D., 2014. *Principles of igneous and metamorphic petrology*. Pearson.
- Wittig, N., Pearson, D.G., Webb, M., Ottley, C.J., Irvine, G.J., Kopylova, M., Jensen, S.M., Nowell, G.M., 2008. Origin of cratonic lithospheric mantle roots: A geochemical study of peridotites from the North Atlantic Craton, West Greenland. *Earth Planet. Sci. Lett.* 274, 24–33. doi:10.1016/j.epsl.2008.06.034
- Wittig, N., Webb, M., Pearson, D.G., Dale, C.W., Ottley, C.J., Hutchison, M., Jensen, S.M., Luguët, A., 2010. Formation of the North Atlantic Craton: Timing and mechanisms constrained from Re-Os isotope and PGE data of peridotite xenoliths from S.W. Greenland. *Chem. Geol.* 276, 166–187. doi:10.1016/j.chemgeo.2010.06.002
- Wohlgemuth-Ueberwasser, C.C., Ballhaus, C., Berndt, J., Paliulionyte, V.S. née, Meisel, T., 2007. Synthesis of PGE sulfide standards for laser ablation inductively coupled plasma mass spectrometry (LA-ICP-MS). *Contrib. Mineral. Petrol.* 154, 607–617. doi:10.1007/s00410-007-0212-x
- Woodland, S.J., Pearson, D.G., Thirlwall, M.F., 2002. A Platinum Group Element and Re–Os Isotope Investigation of Siderophile Element Recycling in Subduction Zones: Comparison of Grenada, Lesser Antilles Arc, and the Izu–Bonin Arc. *J. Petrol.* 43, 171–198. doi:10.1093/petrology/43.1.171
- Wu, F.-Y., Yang, Y.-H., Mitchell, R.H., Li, Q.-L., Yang, J.-H., Zhang, Y.-B., 2010. In situ U–Pb age determination and Nd isotopic analysis of perovskites from kimberlites in southern Africa and Somerset Island, Canada. *Lithos* 115, 205–222. doi:10.1016/j.lithos.2009.12.010
- Xu, X., Griffin, W.L., O'Reilly, S.Y., Pearson, N.J., Geng, H., Zheng, J., 2008. Re–Os isotopes of sulfides in mantle xenoliths from eastern China: Progressive modification of lithospheric mantle. *Lithos, Continental Volcanism and the Chemistry of the Earth's Interior* International Conference on Continental Volcanism 102, 43–64. doi:10.1016/j.lithos.2007.06.010
- Yamashita, Y., Takahashi, Y., Haba, H., Enomoto, S., Shimizu, H., 2007. Comparison of reductive accumulation of Re and Os in seawater–sediment systems. *Geochim. Cosmochim. Acta* 71, 3458–3475. doi:10.1016/j.gca.2007.05.003
- Yang, A.Y., Zhou, M.-F., Zhao, T.-P., Deng, X.-G., Qi, L., Xu, J.-F., 2014. Chalcophile elemental compositions of MORBs from the ultraslow-spreading Southwest Indian Ridge and controls of lithospheric structure on S-saturated differentiation. *Chem. Geol.* 382, 1–13. doi:10.1016/j.chemgeo.2014.05.019

- Young, M., McNicoll, V., Sandeman, H.A., Creaser, R.A., James, D.T., 2007. Meso- to NeoArchean crustal growth and recycling on northern Baffin Island and correlation of Rae Province rocks across mainland Nunavut and Greenland. Presented at the Geological Association of Canada Annual Meeting., p. 89.
- Zaleski, E., Davis, W.J., Pehrsson, S.J., Duke, N.A., Heureux, R., Greiner, E., 2000. Archean continental rifting recorded by orthoquartzite and bimodal kimatiitic-felsic magmatism in the Woodburn Lake group, Western Churchill Province, Nunavut. Presented at the Geocanada 2000, Calgary, Alberta.
- Zaleski, E., Davis, W.J., Sandeman, H.A., 2001. Continental extension, mantle magmas and basement/cover relationships., in: Proceedings of the Fourth International Archean Symposium 2001. Presented at the Fourth International Archean Symposium, AGSO-Geoscience Australia, pp. 374–376.



## ACKNOWLEDGEMENTS

I wish to thank my supervisor Ambre Luguet for sharing her knowledge and for finding financial support during the last four years. I am grateful for the time she spent providing critiques and advices.

I would like to thank Graham Pearson and Bruce Kjarsgaard for providing samples and for the helpful and motivating discussions.

I would especially like to thank Raúl Fonseca for the LA-ICP-MS analyses, the deadlines, the motivations, the discussions, the detailed comments, the sample preparations, the moral support, the ideas, the microprobe support, the projects, the literature, the availability, the one atmosphere experiments, the piston-cylinder experiments, and the Friday Easter. I am sure the list is not complete and I am deeply in debt for everything you did for me, especially during the darkest moments of my PhD. Muito, muito obrigado.

I wish to thank various people for their contribution to this project; Iris Speelmans for the help with the piston cylinder, Chris Dale and Geoff Nowell for the support in Durham, Toni Schulz for the support in Vienna, Jude Coggon and Ashlea Wainright for lab support, Stephan König and Moritz Lissner for discussions and lab support, Thorsten Nagel for the support with the microprobe.

Suggestions and discussion with Chris Ballhaus, Sandro Conticelli and Simone Tommasini are also appreciated.

Claudia, thanks. Sharing the office with my sophisticated Twin Taurus was an alchemic experience, like a Ginger Ale! Dr. Funki, your encouragement and help were simply fundamental for me to reach this point. The Italian will never forget. I will ask Iddu for a life time supply of Vin Santo for you.

Thanks to Alex and to his subducting minipigs, who led me into the mysteries of geochemistry and mass spectrometry. Many, many thanks for the time spent with the ICP-MS.

Thanks to David for the help in developing the analytical part of this work and for the comments. I am grateful for the lessons about some of the scientific voodooos regarding the HSE and the butterfly molecule!

## Acknowledgements

---

A special thanks to Riccardo Avanzinelli to have introduced me into the fantastic world of geochemistry and for the continuous fruitful discussions. Thanks for showing me the positive trend between a brick of Tavernello and a bottle of Sassicaia!

Thanks Max for moving, the, commas, at, the right spot, ',. Thanks also for the improvised “traditional” cooking sessions.

The day cannot start without FTooooM. Thanks for the nice company and the stimulating discussions during our night shifts!

Thanks also to all the people of the Schloss for making it a nice place (Christoph, Felipe, Maria, Stefan, Kathrin, Bo, Aurelia, Marcus, Lisa, Vera, Peter, Elis, Henrik, Johanna, Matze, Jacek, etc.).

Marti (bioturbata), Edo, Tiziano thanks for the friendly and spontaneous help as well as for the unforgivable scientific deliria.

Thanks to my family for the “remote” support and the encouragement to find my way.